

Micro-Raman Investigation of Mechanical Stress in Si Device Structures and Phonons in SiGe

Von der Fakultät für Mathematik, Naturwissenschaften und Informatik
der Brandenburgischen Technischen Universität Cottbus

zur Erlangung des akademischen Grades

Doktor der Naturwissenschaften
(Dr. rer. nat.)

genehmigte Dissertation

vorgelegt von

Diplom-Physiker

Kai F. Dombrowski

geboren am 25.09.1970 in Ratingen

Gutachter: Prof. Dr. Abbas Ourmazd

Gutachter: Prof. Dr. Joachim Wagner

Gutachter: Prof. Dr. Jürgen Reif

Tag der mündlichen Prüfung: 01.12.2000

Contents

Summary	1
----------------------	---

Part A: Mechanical Stress in Si Device Structures

1 Introduction	5
2 Raman Spectroscopy and Silicon	9
2.1 A Short History of the Raman Effect.....	9
2.2 Fundamentals of Raman Scattering.....	10
2.3 Setup of Micro-Raman Spectroscopy.....	12
2.4 Electronic Band Structure and Phonon Dispersion of Silicon	14
2.5 Spatial Resolution	16
2.6 Penetration Depth of Light into Silicon	18
2.7 How to Measure Mechanical Stress.....	20
2.8 Experimental Challenges with Stress Measurements.....	24
2.8.1 Sample Heating	24
2.8.2 Raman Scattering from Structural Sidewalls	25
2.8.3 Influence of Defocusing.....	25
2.8.4 The Influence of Room Temperature	29
3 Theory: Optical Phonons and Stress	31
3.1 Phonons and Strain.....	31
3.2 Phonons and Stress.....	34
3.2.1 Uniaxial Stress	34
3.2.2 Biaxial Stress.....	37
3.3 Film Stress Models.....	39
3.3.1 Analytic Film Stress Models.....	39
3.3.2 Finite Element Calculations	42

4 Mechanical Stress Measurements	43
4.1 Shallow Trench Isolation	44
4.1.1 The TEOS Process	45
4.1.2 The HDP Process	47
4.2 Mechanical Stress caused by STI.....	48
4.2.1 Stress from Nitride and Sidewall Oxide (TEOS & HDP Process).....	49
4.2.2 Stress from Trench Oxide (<i>TEOS Process</i>)	55
4.2.3 Stress from Trench Oxide (<i>HDP Process</i>).....	60
4.2.4 Stress from Pre-Gate Oxidation (<i>HDP Process</i>).....	62
4.2.5 Evolution of Stress (<i>HDP Process</i>).....	68
4.3 Summary	70
Part B: Phonons in SiGe	
5 Introduction: Why SiGe?	75
6 SiGe Experimental	77
6.1 Basic Properties.....	77
6.2 Crystal Growth	79
6.3 Determination of Composition.....	81
7 Phonons in SiGe	85
7.1 Introduction	86
7.2 Phonon Absorption in Silicon and Germanium	88
7.3 The Si Local Vibrational Mode.....	91
7.4 SiGe-Specific Vibrational Modes	92
7.4.1 Infrared and Raman Active Modes	93
7.4.2 Anharmonic Keating Model.....	95
7.4.3 Si-Si vibrations at 460 cm^{-1}	97
7.5 Disorder and the Ge phonon at 300 cm^{-1}	100
7.6 Summary	102
Outlook	105
Abbreviations	107
References	109

Summary

This thesis consists of two parts. It shows an investigation of mechanical stress in silicon device structures (part A) and a detailed analysis of the optical phonon spectrum of bulk SiGe crystals (part B). Both investigations were performed using the experimental technique micro-Raman spectroscopy.

Part A shows the measurement of locally resolved mechanical stress in silicon device structures processed with a mainstream technology, the shallow trench isolation (STI) process. The measurements were performed using micro-Raman spectroscopy. It was one goal of this thesis to demonstrate that the use of ultra violet (UV, 364 nm) laser light significantly enhances stress measurements with micro-Raman spectroscopy as compared to previously used blue (458 nm) laser light. This enhancement is mainly based on the fact that UV light penetrates only 12 nm into silicon as compared to over 300 nm for the case of conventionally used blue light. Through this reduction of penetration depth only the near-surface stress is probed and areas of high stress are now detected by UV, which have previously been averaged away by the deep penetration of blue light. The shorter wavelength of UV light compared to blue light leads to a 20% smaller laser focus on the sample, further reducing the probed sample volume and thus averaging.

Part A shows the mechanical stress induced in the silicon substrate by the various process steps of shallow trench isolation (STI), an important isolation technique for deep submicron CMOS technology. Through the measurement of stress after each relevant process step the evolution of stress through a complete STI process is shown for the first time. The amount of stress caused by each process step could thus be identified. Since UV light is very sensitive to the high surface stress at structural edges, the influence of different process parameters on the amount of stress could also be observed. Different sidewall oxide thicknesses, different trench fill oxides, the trench fill densification in wet and dry ambient, and the formation of the pre-gate (PG) oxide in wet and dry ambient have been investigated. It was found that a wet ambient always drastically increases the stress in the neighboring silicon active areas. The high stress from the bird's beak, which forms especially during wet densification of the trench fill material, has been measured here for the first time. In another STI process the influence of wet pre-gate oxidation on the amount of stress in neighboring silicon active areas has been investigated. It was found that wet PG oxidation increases the stress by 60% as compared to dry PG oxidation, which led to the formation of defects and an increase in diode leakage across narrow trenches by four orders of magnitude.

All of the results mentioned above indicate that UV micro-Raman spectroscopy can be a useful tool for the optimization of defect-free technologies. It is not only

possible to pinpoint areas of high stress, but also to identify the process step or combination of process steps that caused this high stress. This knowledge can then be used to avoid the buildup of large mechanical stress and thus reduce the potential for defect formation in future deep submicron technologies.

Besides the measurement of mechanical stress in silicon device structures, this thesis also presents a detailed analysis of the phonon spectrum of SiGe bulk crystals (part B). Several publications over the past years have dealt with this topic. Still, there were many open questions and sometimes contradictory interpretations of vibrational modes. Due to the measurement in samples of high structural quality and homogeneity and through the comparison of results from Raman measurements, infrared absorption¹, and theoretical calculations², new vibrational modes were observed and contradictory interpretations could be clarified.

One publication showed a behavior of the Ge phonon in samples with very small Si content, which could not be reproduced in this thesis. In that publication the Ge phonon was observed to shift to higher frequencies for Si contents smaller than 2% and for higher Si concentrations it was observed to shift to lower energies. In this thesis the Ge phonon was observed to shift to lower energies for all Si concentrations. This observation was reproduced by theoretical calculations using harmonic and anharmonic Keating models.

The observation of the local vibrational modes of all three silicon isotopes around 390 cm^{-1} in SiGe is the first direct experimental proof, that the assignment of this mode to the silicon local vibrational mode is correct. Several publications presented contradicting interpretations for vibrational modes in Ge-rich SiGe. One example is the mode at 400 cm^{-1} . The comparison of absorption and Raman measurements showed that this mode is exclusively Raman active. The assignment of this mode to the localized vibration of silicon could thus be falsified. This mode is actually caused by Si nearest neighbor pair vibrations, as was proven by the observation of all four possible vibrational modes: two exclusively Raman active and two solely infrared active modes. The agreement with theoretical results from the anharmonic Keating model further validates this assignment.

Starting from pure germanium the development of the silicon localized vibrational mode, Si pair vibrations and three neighboring Si atoms up to larger silicon clusters and eventually Si-rich crystals could be observed. Previously published theoretical investigations could thus be experimentally verified.

¹ performed by Dr. M. Franz

² performed by Dr. H. Rucker

Part A: Mechanical Stress in Si Device Structures

1 Introduction

Silicon is the most important semiconductor material. The invention of the transistor, the integrated wire, and isolation of active areas made the production of integrated circuits (IC's) possible. Silicon microelectronics has since penetrated our everyday lives. The continuing advances in device speed and performance and the constantly decreasing cost per bit on a wafer have one main driving force: miniaturization. In every new technology generation significantly smaller device structures are placed on the same chip area. An increase in functionality per chip area is thus achieved. Moore's law states, that the amount of data storage a microchip can hold doubles every year or at least every 18 months [1]. In other words, the number of bits per square centimeter doubles at least every 18 months. This increase leads to an exponential rise in computational power. The continuing reduction of feature size, on the other hand, keeps posing technological challenges that have to be overcome before the next generation circuit can be produced.

One result of the continuing miniaturization is the increase of mechanical stress in the device structures. The differing thermal expansion coefficients of the various oxide, nitride and metal layers induce large mechanical stress in the underlying silicon substrate. The stress is usually concentrated along structural edges and at corners. As the device dimensions decrease, edges and corners come closer together and the stress begins to overlap and increase. Above a certain threshold, stress can trigger defects, cracking or the formation of voids and will thus render the device useless. Poor manufacturing yield can in turn decide the market success or failure and the profitability of an otherwise superior device.

Besides the detrimental influence on the fabrication process, mechanical stress also influences the electrical properties of a device even in the absence of any defects. Mechanical stress can degrade hot carrier lifetimes and gate oxide quality, causing traps and a decrease in device speed; a positive side-effect being, that stressed transistor channels can increase carrier mobility.

As devices become smaller, mechanical stress becomes more and more important. It is therefore desirable, to be able to measure mechanical stress with high spatial resolution during device formation, to pinpoint areas of critical stress levels. The knowledge of which process step induces how much stress can then lead to changes in process parameters with the effect of avoiding high stress and thus lowering the probability for defect formation.

Several methods deliver information on mechanical stress in semiconductor devices. The most important are X-ray diffraction, transmission electron microscopy (TEM), and micro-Raman spectroscopy. All of these methods have advantages and

disadvantages. The criteria which decide the usefulness of a technique for stress measurements in silicon microelectronic technologies are spatial resolution, stress sensitivity, and time. Evaluating all techniques according to these criteria leaves micro-Raman spectroscopy to be the most suitable.

X-ray diffraction is very sensitive to small changes in the lattice constant, a_0 , with a strain sensitivity of $\Delta a_0/a_0 \approx 10^{-7}$. The size of the probing spot is in the range of 1 mm^2 . Since device dimensions are on the order of μm , the measurement of locally resolved stress on a device scale is impossible.

The TEM methods, such as stress contrast in cross-sectional TEM (XTEM) and convergent beam electron diffraction (CBED), reach spatial resolutions of a few nanometers. The strain sensitivity of 10^{-4} is lower than that of X-ray diffraction, but about the same as for micro-Raman spectroscopy. The main disadvantages here are the destructive sample preparation and the extensive modeling required to extract the information on stress from the measurements. The time it takes to obtain stress information using TEM is often in the range of weeks or even months. This is prohibitive in an industry, where such information is often desired within hours or at the most within a few days.

Micro-Raman spectroscopy reaches neither the stress sensitivity of X-ray diffraction nor the spatial resolution of TEM, but is yet the most suitable method to deliver stress information on a microscopic scale. The strain sensitivity is the same as for TEM with 10^{-4} and the spatial resolution is around $0.6 - 1.0 \mu\text{m}$. The time it takes to gain information on mechanical stress in a device structure is of the order of hours. This makes the method good enough to be used as a monitoring tool during processing.

At the start of this thesis the main drawback of micro-Raman spectroscopy for the assessment of mechanical stress was the relatively large sample volume probed during the measurement. This is a drawback, because the stress information is averaged over the probed sample volume. This volume is determined laterally by the laser spot size and vertically by the penetration depth of the laser light into the material. Since stress decreases quickly into the substrate and changes by orders of magnitude within a few nanometers away from the edge or surface where the stress is created, an assessment of the true near-surface stress is desirable. It will be shown in this thesis, that near-surface stress can be assessed very well using micro-Raman spectroscopy with ultra violet (UV) excitation. UV light (364 nm) penetrates only 12 nm deep into silicon as compared to over 300 nm for conventionally used blue light (458 nm). This significant reduction in penetration depth allows one to monitor areas of high near-surface stress averaged away by the large penetration of blue (457.9 nm) or green (514.5 nm) light. It will also be demonstrated, that the laser spot size of around $1 \mu\text{m}$ is no barrier to measure stress changes in submicron device structures.

In chapter 2, a general introduction to micro-Raman spectroscopy and a discussion of the experimental details, such as spatial resolution and penetration depth of light into silicon, will be given. Chapter 3 presents the theoretical background of the influence of stress and strain on the optical phonon modes in silicon.

Chapter 4 presents the experimental results of stress measurements in device structures processed with an important future isolation technique, the shallow trench isolation (STI). The influence of different process parameters (nitride and sidewall oxide thickness, different trench fill methods, densification in wet and dry ambient, growth of wet and dry pre-gate oxides, and well implantation) on the amount of mechanical stress in the underlying silicon substrate will be discussed.

2 Raman Spectroscopy and Silicon

This chapter starts with a short history (section 2.1) and the fundamentals of Raman spectroscopy (section 2.2). After the description of the experimental setup of micro-Raman spectroscopy (section 2.3) two significant parameters will be defined: the penetration depth (section 2.6) and the laser spot size (section 2.5). These two parameters are responsible for the significant improvements achieved when measuring mechanical stress with ultra violet (UV) light instead of visible light. The phonon dispersion and electronic band structure of silicon will also be presented (section 2.4). Afterwards, the measurement of mechanical stress in silicon device structures will be explained (section 2.7). The chapter closes with a discussion of some experimental challenges of stress measurements, such as the influence of defocusing or geometric considerations concerning the experimental setup (section 2.8).

2.1 A Short History of the Raman Effect

The Raman effect was named after Prof. C.V. Raman, who published the observation of "a new type of secondary radiation" for the first time in 1928 [2]. Similar observations were found independently by Landsberg and Mandelstam [3]. At first this newly discovered effect was used extensively to study the excitation and vibronic properties of molecules. With the invention of the laser, the investigation of semiconductor materials became possible. Russell [4] and later Parker et al. [5] were the first to publish first- and second-order phonon spectra of silicon and germanium. From that time on, there has been significant progress in the understanding of the mechanism involved in Raman scattering and the techniques used to make the experimental observations [6, 7]. Around 1989 the first stress measurements using micro-Raman spectroscopy were performed [8] on local oxidation of silicon (LOCOS) samples. Since then the influence of different isolation techniques, of nitrides, silicides, and even some metals on mechanical stress in silicon have been investigated. Overviews are given in [9], [10] and references therein. None of these stress measurements were performed with UV light. This is done for the first time in this thesis.

2.2 Fundamentals of Raman Scattering

Raman spectroscopy measures the inelastic scattering of light in a sample by elementary excitations of the sample. In the scattering process, energy is transferred between the incident photon $\hbar\omega_i$ and the sample, resulting in a scattered photon of energy $\hbar\omega_s$. The amount of energy transferred corresponds to the energy of the elementary excitation $\hbar\Omega_j$. Energy conservation yields

$$\hbar\omega_s = \hbar\omega_i \pm \hbar\Omega_j. \quad (2.1)$$

Here, the minus sign stands for processes in which an elementary excitation is generated (Stokes process), and the plus sign for processes in which an elementary excitation is annihilated (anti-Stokes process). The efficiency of the anti-Stokes process depends on the population of the elementary excitation state, which is proportional to the Boltzmann distribution. Except for the case of resonant Raman scattering, the intensity ratio between Stokes and anti-Stokes processes can be used to determine the sample temperature.

In analogy to energy conservation, quasi-momentum conservation yields the relation between incident photon wavevector \mathbf{k}_i , scattered photon wavevector \mathbf{k}_s and the wavevector of the elementary excitation \mathbf{q}_j :

$$\mathbf{k}_s = \mathbf{k}_i \pm \mathbf{q}_j \quad (2.2)$$

For silicon, the wavelength of the incident laser light is long compared to the lattice constant of the material, and therefore $\mathbf{q}_j \approx 0$. Thus, only the optical phonons near the Γ point at the center of the Brillouin zone contribute to the scattering. Throughout this thesis, only measurements of Raman scattering by optical phonons in Si, Ge and SiGe will be presented. From here on, the theory will therefore be presented with regard to phonons, although it is generally true for other elementary excitations as well.

In the Raman scattering process, the interaction between incident photon and phonon is indirect. It is mediated by electronic interband transitions, which define the dielectric susceptibility χ in the visible spectral range. Raman scattering occurs when these interband transitions are influenced by the lattice vibrations. The normal coordinate of a phonon can be expressed classically as

$$Q_j = A_j \exp[\pm i (\mathbf{q}_j \cdot \mathbf{r} - \Omega_j \cdot t)]. \quad (2.3)$$

The influence of this vibration on the susceptibility tensor can be described by expanding χ into a Taylor series with respect to the normal coordinate of the vibration Q_j :

$$\chi = \chi^{(0)} + \sum_j \chi^{(1)} Q_j + \dots = \chi_0 + \sum_j \left(\frac{\partial \chi}{\partial Q_j} \right)_0 Q_j + \dots \quad (2.4)$$

The summation runs over the $3N-3$ vibrational modes, with N the number of atoms in the unit cell. For the di-atomic base of silicon, the summation runs over the three optical phonons.

When monochromatic light with frequency ω_i is incident on a sample in the direction \mathbf{k}_i , the associated electric field \mathbf{E} induces an electric moment \mathbf{P} according to

$$\mathbf{P} = \epsilon_0 \chi \mathbf{E} = \epsilon_0 \chi \mathbf{E}_0 \exp[i(\mathbf{k}_i \cdot \mathbf{r} - \omega_i t)]. \quad (2.5)$$

Combining equations (2.3) through (2.5) results in

$$\mathbf{P} = \epsilon_0 \chi_0 \mathbf{E} + \sum_j \epsilon_0 A_j \mathbf{E}_0 \left(\frac{\partial \chi}{\partial Q_j} \right)_0 \exp[i(\mathbf{k}_i \pm \mathbf{q}_j) \cdot \mathbf{r} - i(\omega_i \pm \Omega_j) t] \quad (2.6)$$

The first term gives rise to Rayleigh scattering. The second term describes the anti-Stokes and Stokes scattering with frequencies $\omega_i \pm \Omega_j$. This second term will only be observed when $(\partial \chi / \partial Q_j)_0 = \chi^{(1)}$ differs from zero, giving rise to the selection rules discussed below. Terms of higher order in the Taylor expansion in (2.4) describe multi-phonon processes, which will not be pursued further.

The elements of $\chi^{(1)}$ are often referred to as the components of the Raman tensor. They determine whether a normal vibration Q_j is Raman active or not. The exact form of the Raman tensor depends on crystal symmetry. Loudon derived these tensors for all crystal classes [11]. For silicon, in the ortho-normal coordinate system $x = [100]$, $y = [010]$ and $z = [001]$, they have the form:

$$\mathbf{R}_x = \begin{pmatrix} 0 & 0 & 0 \\ 0 & 0 & d \\ 0 & d & 0 \end{pmatrix}, \quad \mathbf{R}_y = \begin{pmatrix} 0 & 0 & d \\ 0 & 0 & 0 \\ d & 0 & 0 \end{pmatrix}, \quad \mathbf{R}_z = \begin{pmatrix} 0 & d & 0 \\ d & 0 & 0 \\ 0 & 0 & 0 \end{pmatrix} \quad (2.7)$$

The total scattering efficiency I is then given by

$$I = C \cdot \sum_j |\mathbf{e}_i \cdot \mathbf{R}_j \cdot \mathbf{e}_s|^2 \quad (2.8)$$

with C a constant, and \mathbf{e}_i and \mathbf{e}_s the polarization vectors of the incident and scattered light, respectively. For back scattering from a (001) surface, \mathbf{R}_x and \mathbf{R}_y correspond to the transverse optical (TO) phonons polarized along x and y , respectively, and \mathbf{R}_z to the longitudinal optical (LO) phonon polarized along z .

For back scattering from a (001) surface, equations (2.7) and (2.8) indicate, that only two polarization configurations for the incident and scattered light permit the Raman scattering to be observed:

- i) For \mathbf{e}_i and \mathbf{e}_s perpendicular: $z(x,y)-z$ with $x \parallel (100)$
- ii) for \mathbf{e}_i and \mathbf{e}_s parallel: $z(x,x)-z$ with $x \parallel (110)$.

In both cases, only the LO phonon can be observed. To observe the TO phonons another scattering geometry, such as 90° scattering, or backscattering from a (110) surface, would be needed.

2.3 Setup of Micro-Raman Spectroscopy

Micro-Raman spectroscopy combines Raman spectroscopy with the spatial resolution of a microscope. The incident laser light is focussed through a microscope objective onto the sample. The Raman scattered light is collected through the same

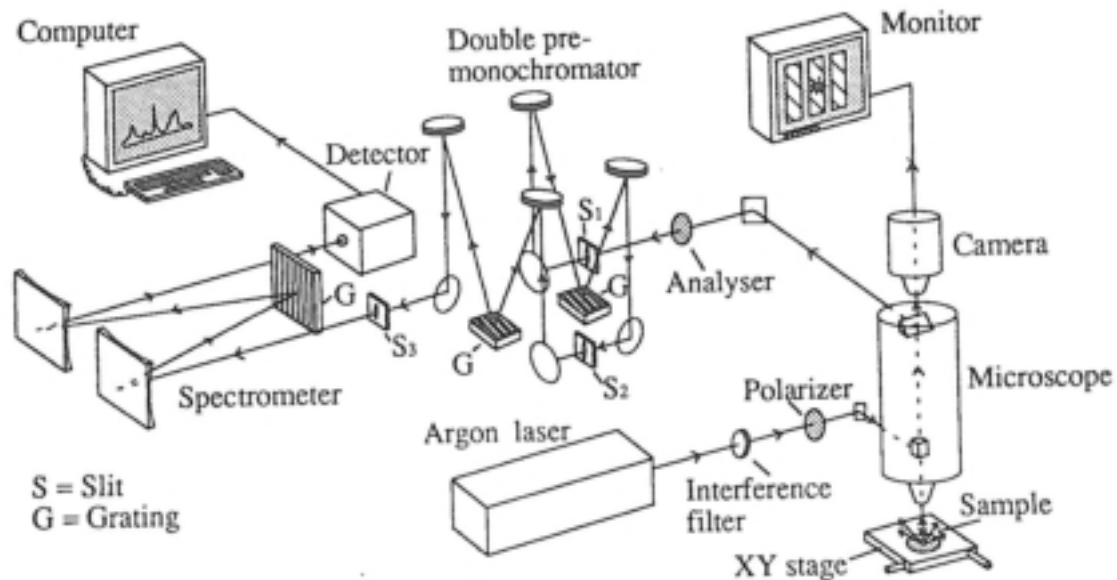


Fig. 2.1: Schematic setup of a Dilor XY micro-Raman spectrometer¹. The system consists of an Ar^+ -ion laser as light source, a microscope, the spectrometer consisting of a double grating pre-monochromator and a single grating spectrograph, a CCD detector, and a computer to read out the spectra. The samples are placed under the microscope on a motorized xy-stage.

¹ Figure reproduced by courtesy of Dr. I. De Wolf, IMEC, Belgium

objective in the back scattering configuration. The Raman signal is thus collected from a spatially well defined region with the lateral resolution determined only by the aperture of the microscope objective and the laser wavelength. The 457.9 and 363.7 nm lines of an Ar⁺-ion laser from the Coherent Innova 400 series served as light source.

The micro-Raman spectrometers used for this work are commercial systems from Dilor (XY-500 and XY-800). The spectrometers consist of a double grating pre-monochromator and a single grating spectrograph. The pre-monochromator is build in a typical Czerny-Turner mounting. It can be used in subtractive mode, to select the spectral range and suppress stray light. It can also be switched to additive mode for high spectral resolution. Since the Raman scattered light is very weak compared to the incident laser power - only about one out of 10⁶ photons is elastically scattered - a very sensitive detector is necessary to record the scattered light, while the laser line has to be kept from reaching the detector. The recording is done by a CCD (charge coupled device) camera cooled with liquid nitrogen to about 110 K to minimize thermal noise. The spectra are read out by a computer.

Spectrometer	Dilor XY-500 (vis)	Dilor XY-800 (UV)
Gratings	1800 line/mm	2400 line/mm
Blaze	500 nm	250 nm
Focal length	500 mm	800 mm
Objective	Olympus 100x	Zeiss 100x Ultrafluar
N.A.	0.95	0.9

Tab. 2.1: *Properties of the Raman spectrometers and microscope objectives.*

The entrance optics to the spectrometer is confocal. This enables one to select the volume from which the scattered light is to be detected and also helps reduce stray. For stress measurements the depth selection of the confocal arrangement plays no role, because the depth selection of order μm is larger than the penetration depth of the laser light into silicon.

The spectral resolution is defined by the focal length of the spectrometer and the dispersion of the gratings. The laser spot, which is focussed onto the entrance slit, is usually smaller than the slit width, which is chosen to allow enough light to enter the spectrometer. The size of the entrance slit S1 (see Fig. 2.1) is typically chosen to be 2 μm wide.

For the measurement of mechanical stress in silicon device structures a Dilor XY with a focal length of 800 mm and 2400 line/mm gratings blazed at 250 nm was used. This spectrometer was specifically designed for use in the UV spectral range. All optical elements are UV compatible and the CCD is back-side thinned with a special UV coating to increase the sensitivity. For the investigation of phonons in SiGe (Chapter 7), a Dilor XY spectrometer with a focal length of 500 mm was used. This spectrometer has gratings with 1800 lines/mm blazed at 500 nm. Some properties of both spectrometers are summarized in Tab. 2.1.

The investigation of phonons in SiGe was often performed at low temperatures ($T \approx 80$ K). To reach those temperatures the samples were placed in a CryoVac flow-through cryostat cooled with liquid nitrogen.

2.4 Electronic Band Structure and Phonon Dispersion of Silicon

Silicon has the same crystal structure as diamond. The atoms build the crystal through covalent bonds. The electronic bandgap of 1.1 eV is indirect. The conduction band minimum lies at 85% of the distance between the Γ point and the X point in the Δ direction (Fig. 2.2). In Raman scattering the interaction between the incident laser light and the silicon phonons is mediated via the electronic system, as described in section 2.2. For the absorption of the laser light it is thus not the indirect, but the direct bandgap which is important for this interaction. The smallest direct gap of ~ 3.4 eV is between the valence band Γ'_{25} and the conduction band Γ_{15} (Fig. 2.2, left).

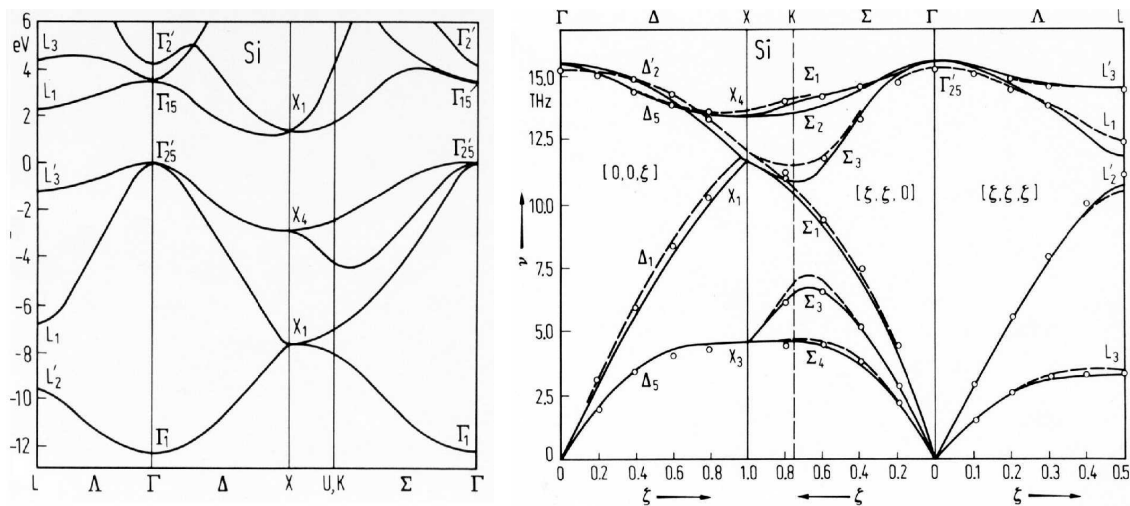


Fig. 2.2: *Electronic band structure (left) and phonon dispersion (right) of silicon.*

Due to the cubic symmetry of silicon, the optical phonon branches shown in the phonon dispersion in Fig. 2.2 are degenerate at the Γ point. The energy of the optical phonons at the Γ point corresponds to about 521 cm^{-1} . The wave number (cm^{-1}) is a spectroscopic unit used typically for phonon energies. Some conversion factors are:

$$8.0655 \text{ cm}^{-1} \triangleq 1 \text{ meV} \triangleq 0.2418 \text{ THz.} \quad (2.9)$$

The Raman spectrum of silicon is shown in Fig. 2.3. A Raman spectrum obtained with UV (363.7 nm) and blue light (457.9 nm) is shown. The broad central line at $\omega = 521 \text{ cm}^{-1}$ in each spectrum is the triply degenerate optical phonon mode of silicon. The other sharp lines are plasma lines from the laser. They result from atomic transitions of the Ar^+ ions in the laser gas plasma and are reflected off the sample surface. Their energetic position in the spectrum is independent of the investigated sample material. The plasma lines are thus ideal to be used as an absolute energetic reference.

The triple degeneracy of the silicon phonon can be lifted by mechanical stress. A detailed discussion of this influence is given in chapter 3.

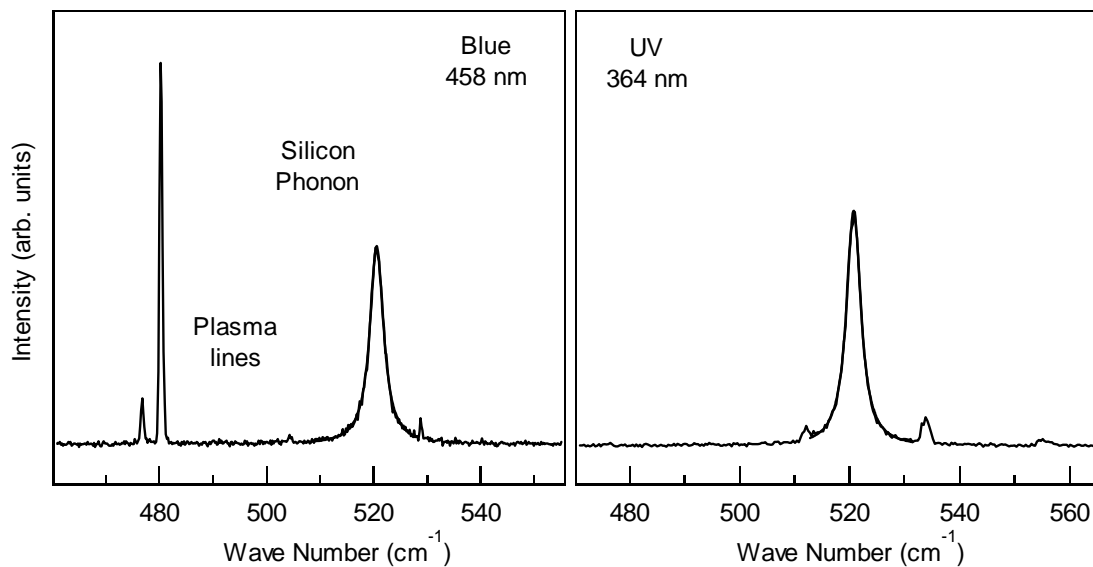


Fig. 2.3 Raman spectrum of silicon obtained with blue (left) and UV light (right). The broad central line is the triply degenerate optical phonon at $\omega = 521 \text{ cm}^{-1}$. The other lines in the spectrum are plasma lines from the Ar^+ -ion laser. Their energetic position in the spectrum is fixed, because they result from atomic transitions of the ions in the laser tube. This plasma light is reflected off the sample surface and can be used as an absolute energetic reference.

2.5 Spatial Resolution

The Raman scattered light is collected by the microscope objective. The collected signal contains all information from the probed volume. This volume is determined laterally by the size of the laser spot on the sample and vertically by the penetration depth of the laser light into the sample material. The penetration depth will be defined in the next section 2.6.

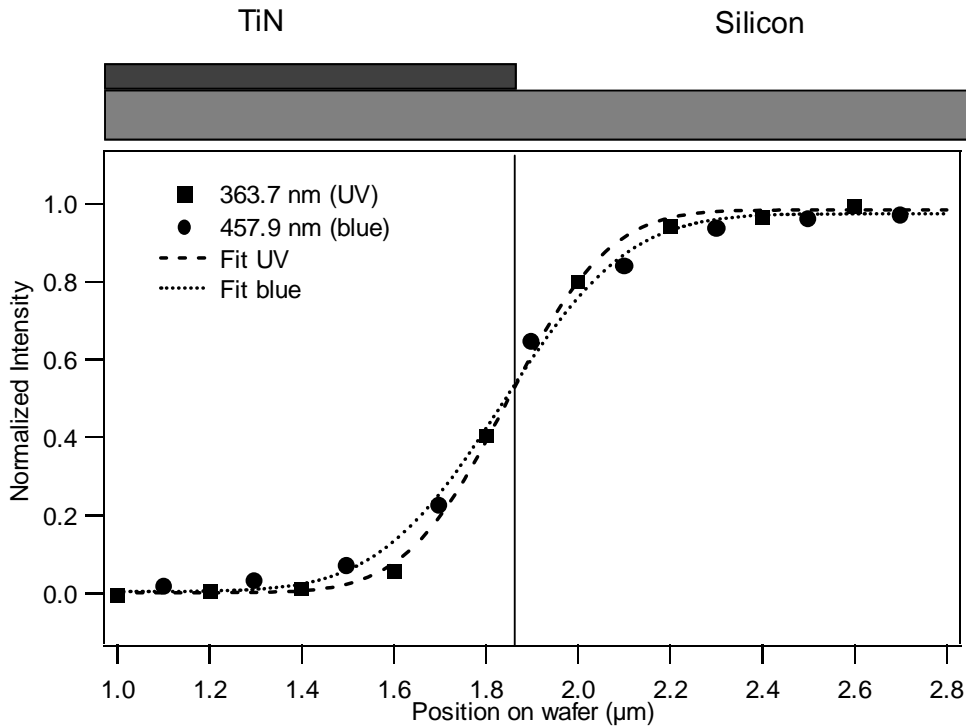


Fig. 2.4: *Intensity distributions while scanning across an opaque TiN metal edge. The points are the normalized measured intensities. The lines are the numerical fits of the convolution of a Gaussian distribution with a step function to the experimental data.*

The intensity distribution in the laser focus is assumed to be Gaussian. This is a reasonable assumption, since the objective aperture is uniformly illuminated by the laser beam. Throughout this thesis all laser spot sizes given are referring to the full width at $1/e^2$ of the Gaussian intensity distribution.

The laser spot sizes were determined experimentally, by scanning the laser spot over a sharp metal edge (20 nm TiN), which is opaque to the laser light. The intensity distribution of the measured Raman light is then given by the convolution of a Gaussian distribution with a step function. Fig. 2.4 shows the comparison of two such intensity distributions obtained with the 457.9 and 363.7 nm laser lines and the UV objective (N.A. = 0.9). The laser spot sizes obtained from the fit to the experimental data shown

wavelength	laser spot size at $1/e^2$
457.9 nm	0.8-0.9 μm
363.7 nm	0.6-0.7 μm

Tab. 2.2: *Laser spot sizes obtained for different laser lines.*

in Fig. 2.4 are: 0.69 μm for UV and 0.86 μm for the blue laser line. Usually the values lie in the ranges shown in Tab. 2.2.

Several attempts have been made by different authors to improve the spatial resolution significantly below 1 μm . One attempt uses the combination of Raman spectroscopy with scanning near-field microscopy (RSNOM) [12]. The authors of [12] reached a spatial resolution of ≈ 150 nm using 633 nm light. The problem with near-field microscopy is, that it fails as soon as a film, such as nitride or oxide, is on top of the silicon, because the near-field condition can no longer be met. The signal intensities are also usually very small and the measured phonons quite broad, making the detection of small phonon shifts difficult. This method is therefore not suitable for stress measurements in silicon device structures.

Another method uses the conventional micro-Raman setup and tries to raise the numerical aperture of the microscope above 1. This can either be achieved by using an oil immersion lens (N.A. ≈ 1.4) [13] or a solid immersion lens (SIL) with an index of refraction greater than one [14]. De Wolf [13] demonstrated the improved spatial resolution using an oil immersion lens, achieving laser spots of 0.5 μm with 457.9 nm laser light. The use of oil immersion lenses with UV light is difficult, because the oils usually show strong fluorescence when excited with UV light. The use of solid immersion lenses with an index of refraction of $n \approx 1.9$ at 488 nm have led to an effective N.A. of nearly 1.5 [14]. The lenses are typically small glass hemispheres placed on top of the sample under the microscope objective. If the sample surface is not very flat, as is seldom the case after the deposition of thick nitride or oxide layers, the "magnifying effect" of the SIL is usually diminished, if not lost. Nonetheless, solid immersion lenses could lead to laser spot sizes of about 150 nm [14] making them an interesting candidate to really enhance the lateral resolution of micro-Raman spectroscopy in the future.

2.6 Penetration Depth of Light into Silicon

As described in section 2.2, the interaction between the laser light and the optical phonons is mediated via the electronic system. The interaction will thus be strong, when the energy of the incident laser light coincides with a maximum in the electronic density of states. This enhancement of the Raman scattering efficiency is called "resonant Raman scattering".

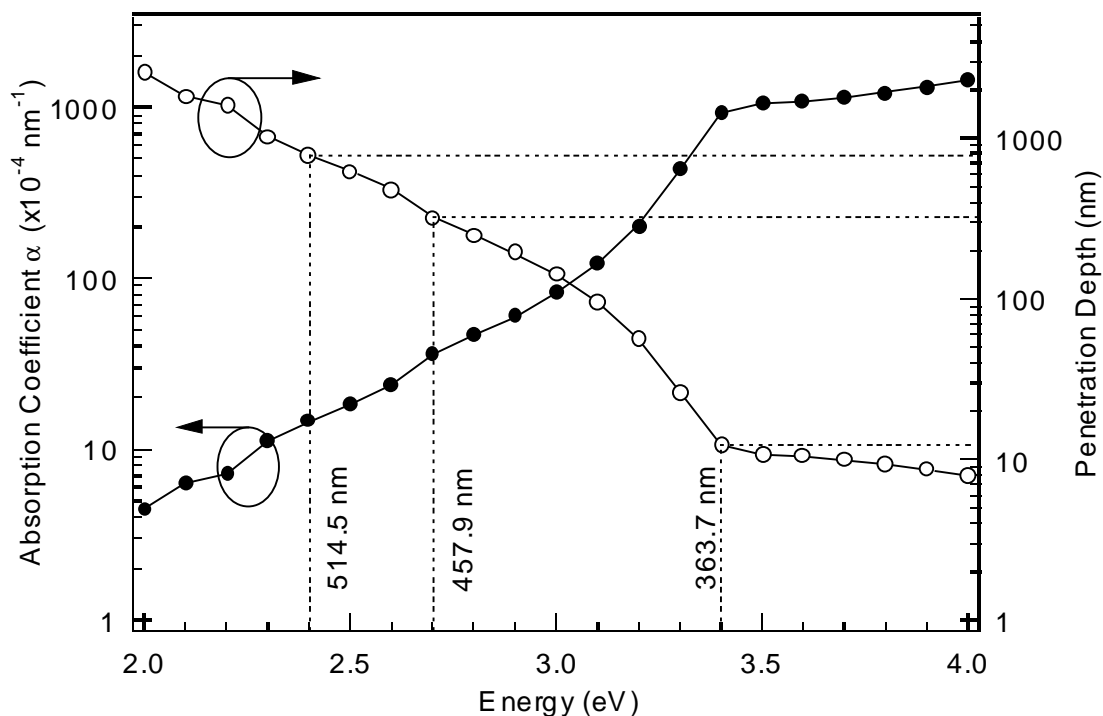


Fig. 2.5: Absorption coefficient of silicon (left axis) and resulting laser penetration depth (right axis). The three most commonly used laser excitation wavelength and the corresponding penetration depths are indicated. The absorption data is taken from [16] and the penetration depths are calculated as discussed in the text (Eq. (2.13)).

In silicon the size of the direct gap at the Γ point is ~ 3.4 eV. As the energy of the incident light approaches the energy of the direct gap, the absorption coefficient increases. The laser light, therefore, has a smaller penetration depth into silicon, the higher the absorption coefficient (Fig. 2.5). Throughout this thesis, the following definition for the penetration depth will be used [9]:

The total scattered light intensity I_s , integrated from the sample surface to a depth d , is given by:

$$I_s = I_0 D \int_0^d e^{-2\alpha x} dx = \frac{I_0 D}{2\alpha} (1 - e^{-2\alpha d}) \quad (2.10)$$

I_0 is the incident laser intensity, D the Raman scattering cross section and α the absorption coefficient of silicon for the given laser wavelength. The total scattered intensity from depth d to infinity I_d is given by:

$$I_d = I_0 D \int_d^{\infty} e^{-2\alpha x} dx = \frac{I_0 D}{2\alpha} e^{-2\alpha d} \quad (2.11)$$

The penetration depth d_p is now defined as that depth from which 90% of the total scattered intensity originates, thus satisfying the relation

$$I_s = 0.9 (I_s + I_d). \quad (2.12)$$

Solving equation (2.12) for d using equations (2.10) and (2.11) yields for the penetration depth d_p :

$$d_p = \frac{-\ln 0.1}{2\alpha} \quad (2.13)$$

The resulting penetration depth for silicon is shown in Fig. 2.5. As the laser energy approaches the direct transition $\Gamma'_{25} - \Gamma_{15}$ the penetration depth reaches a minimum of 10 to 12 nm. Tab. 2.3 summarizes the penetration depths for the three most commonly used Ar^+ -ion laser lines. It becomes clear from this table and Fig. 2.5, that the use of UV becomes inevitable if one wants to obtain near-surface information in silicon.

Laser line [nm]	Penetration depth d_p [nm]
514.5	760
457.9	320
363.7	12

Tab. 2.3: Penetration depth into silicon of the three most commonly used Ar^+ -ion laser lines.

2.7 How to Measure Mechanical Stress

For stress measurements, the sample is placed under the microscope on a computer controlled xyz-stage (Fig. 2.1). The x and y tables can be moved in steps of 50 nm and the z table in steps of 100 nm. To measure the stress in a device structure a Raman spectrum (Fig. 2.3) is taken at a certain distance away from the structure, preferably on unstrained silicon (position zero, Fig. 2.6). The exact position of the Si phonon is obtained by fitting a Lorentz function into the measured phonon peak. The sample is then moved one step (in this thesis always 0.1 μm) and another Raman spectrum is taken at the new position. The newly obtained Si peak is again fit by a Lorentz line and the peak position plotted vs. position on the wafer. Repeating this procedure until the whole device structure is scanned delivers the shift of the Si phonon peak position as a function of position on the wafer. An example for this procedure is shown in Fig. 2.6 (left graph). The shift of the Si phonon indicates mechanical stress as will be discussed in detail in chapter 3.

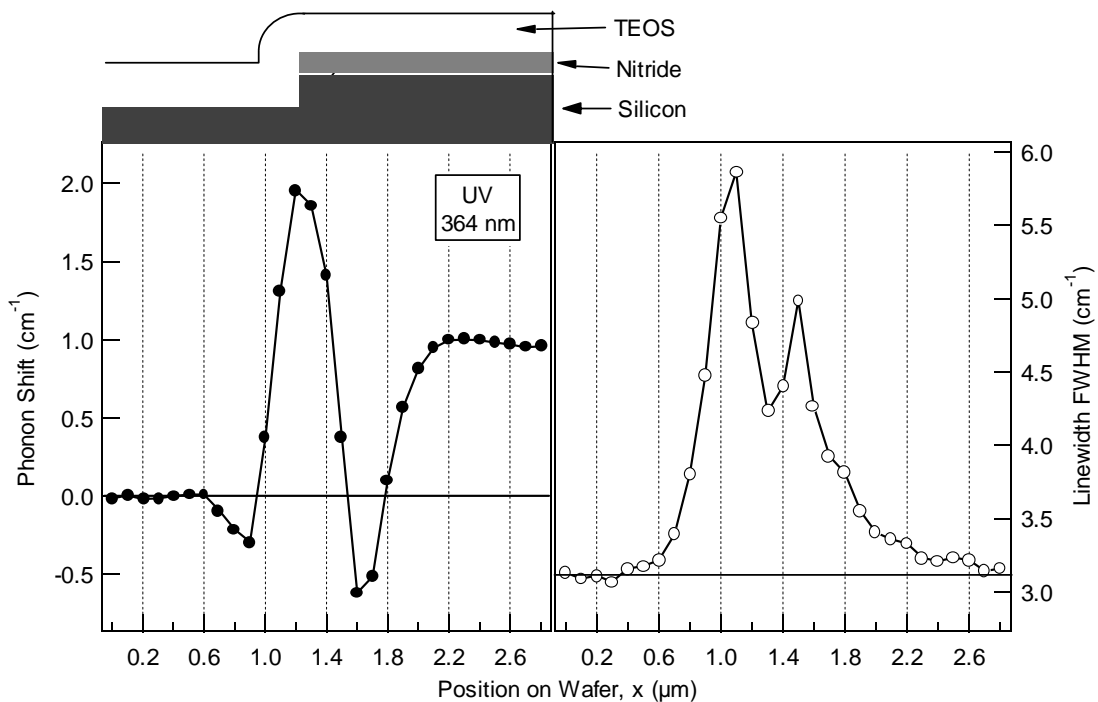


Fig. 2.6: *Left graph: Shift of the silicon phonon peak position as the laser spot (UV light, 364 nm) is scanned across a silicon device structure shown schematically at the top. The shift of the silicon phonon peak position from the value of unstrained silicon (zero shift, horizontal line at 0 cm⁻¹) indicates mechanical stress (details in chapter 3). The phonon peak positions were obtained by fitting a Lorentz function into the measured Raman peaks (Fig. 2.7). The full widths at half maximum (FWHM) of these fitted curves are shown in the right graph. The change in linewidth from the value of unstrained silicon, indicated by the horizontal line at 3.2 cm⁻¹, indicates an inhomogeneous stress distribution under the laser spot.*

Fitting only one Lorentz function into the measured phonon peak for all positions on the wafer as shown in Fig. 2.6 is a simplification. In reality, the phonon peak in the Raman spectra has a Lorentzian lineshape only in the case of unstrained silicon, or in the case of homogeneous uniaxial stress under the laser spot. Any deviation from these two conditions can result in a broadened phonon peak with often asymmetric shapes. This change in phonon peak shape is a result of the following two main influences: (i) splitting of the phonon peak due to mechanical stress and (ii) inhomogeneous stress distribution under the laser spot.

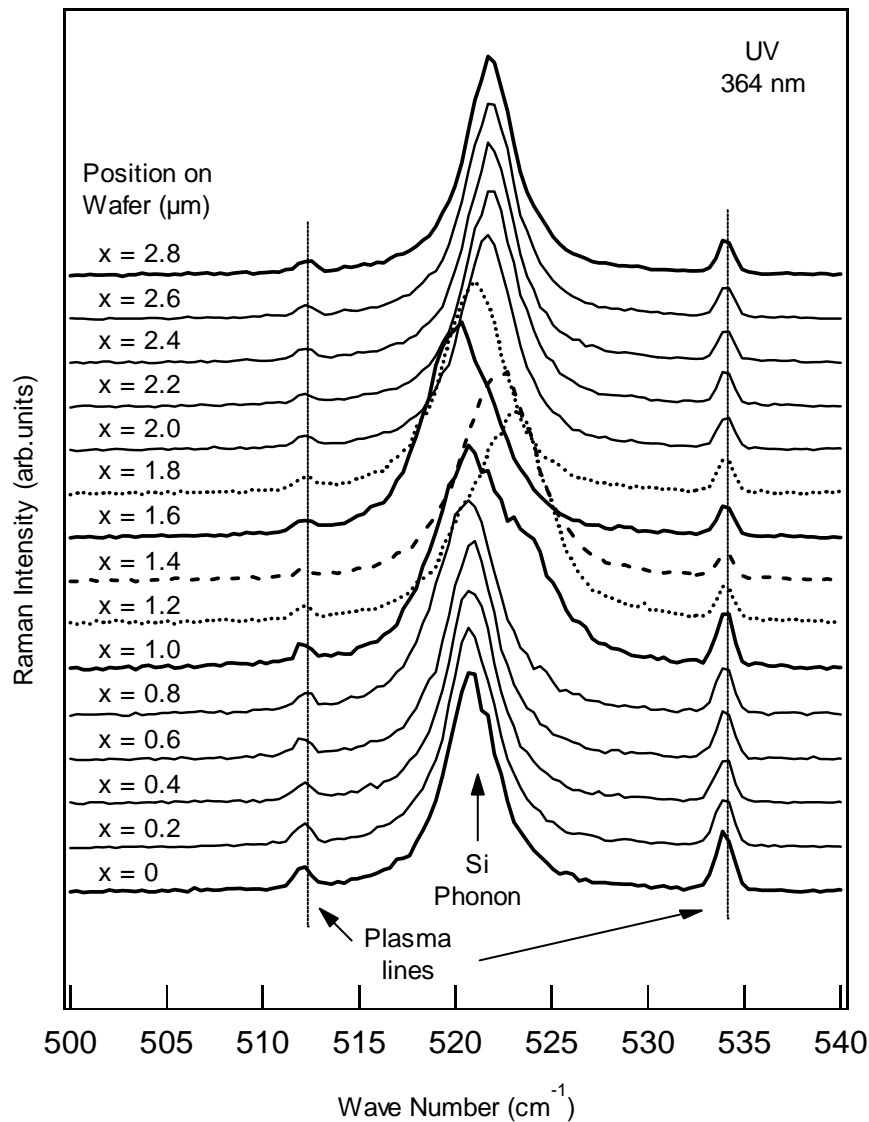


Fig. 2.7: Measured Raman spectra obtained with UV light (364 nm) crossing the sample structure shown in Fig. 2.6. The position on the wafer, where the spectrum was obtained, is indicated on the left side above each trace. The silicon phonon peak position and lineshape change remarkably, while the plasma lines are unaffected. The silicon phonon peak position and linewidth obtained by fitting a single Lorentz line into each silicon phonon peak is shown in Fig. 2.6 (phonon shift: left graph, linewidth: right graph).

Mechanical stress (or strain) can lift the degeneracy of the optical phonon modes, which can lead to a splitting of the phonon peak in the Raman spectra (a detailed discussion about the influence of stress on the optical phonon modes in silicon is given in chapter 3). In addition to the splitting of the phonon modes due to stress, the collected Raman light from under the laser spot contains all stress information from the probed sample volume. If this stress is inhomogeneously distributed, as is always the case along film and structural edges, the silicon phonon peak in the Raman spectrum will be a superposition of many Lorentz lines at different frequencies, each according to the stress in the infinitesimal scattering volume from which they originate. The result can be a broadened and asymmetric lineshape. An example for this is shown in Fig. 2.7.

Fig. 2.7 shows the Raman spectra obtained with UV light (364 nm) while scanning across the sample structure shown at the top of Fig. 2.6. The silicon phonon peak in the center of each trace changes remarkably for different positions on the wafer. These changes are the result of an inhomogeneous stress distribution under the laser spot together with a splitting of the phonon modes under the influence of mechanical stress, as discussed before. The plasma line positions are not affected by the underlying sample structure. This is the expected behavior, since the plasma light is merely reflected off the sample surface.

Despite the changes in lineshape, a single Lorentz line is fit into each phonon peak of Fig. 2.7, and the peak positions and linewidths are plotted vs. position on the wafer (Fig. 2.6). Since it is impossible to determine from the measured Raman spectra alone, whether the broadening is caused by inhomogeneous stress in the probed sample volume

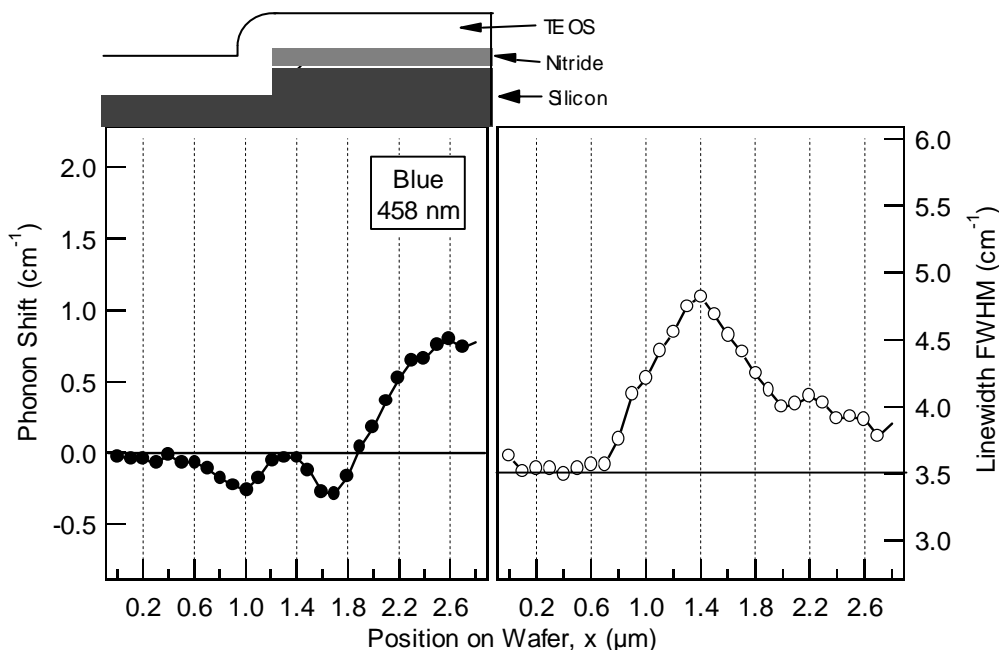


Fig. 2.8: The two graphs are identical to the ones shown in Fig. 2.6, except that here the measurement was performed using blue light (458 nm) instead of UV. The corresponding Raman spectra are shown in Fig. 2.9.

or due to splitting of the phonon modes, fitting a single Lorentz peak into the Raman spectra delivers roughly the averaged stress value in the probed sample volume. This averaging is indicated by the change in linewidth (Fig. 2.6).

The measurement of mechanical stress with blue light (458 nm, spot size: 0.9 μm , penetration depth: 320 nm) generally results in even more averaging compared to the same measurement with UV light (364 nm, spot size: 0.7 μm , penetration depth: 12 nm), simply because the probed sample volume is 25 to 30 times larger. The changes in silicon phonon linewidth and asymmetry (Fig. 2.9) are generally much smaller, though, because the contribution of each sample volume element to the total signal is smaller than in the case of UV.

Fig. 2.8 shows the same stress measurement as in Fig. 2.6, but using blue instead of UV light. The silicon phonon shifts less (left graph, Fig. 2.8) and the linewidths of the fitted Lorentz peaks are also smaller (right graph, Fig. 2.8). The lineshape of the

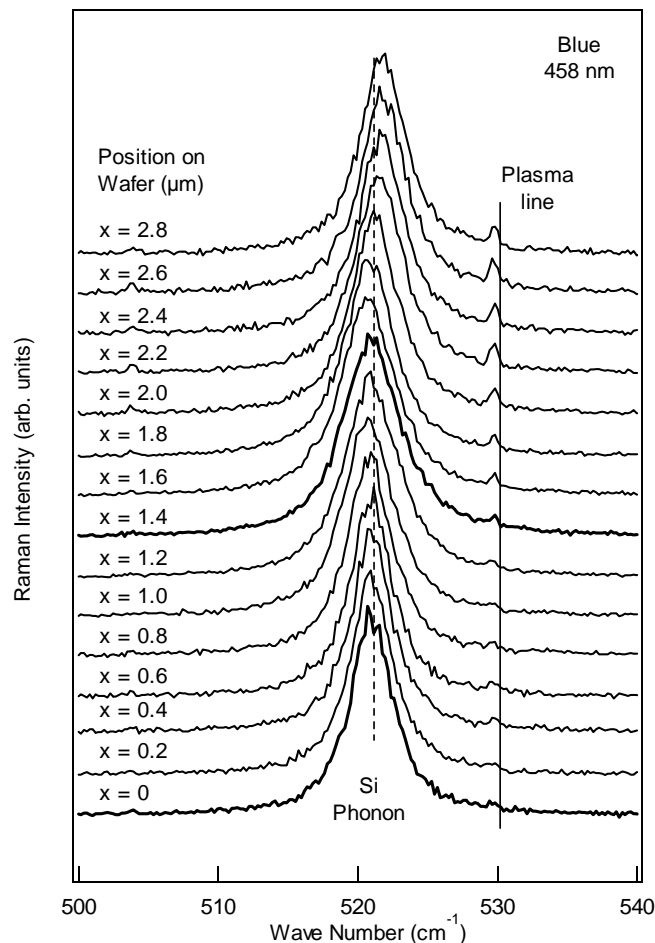


Fig. 2.9: Measured Raman spectra obtained with blue light (458 nm) crossing the sample structure shown in Fig. 2.6 and Fig. 2.8. The silicon phonon peak position and lineshape changes much less than in Fig. 2.7. The silicon phonon peak position and linewidth obtained by fitting a single Lorentz line into each silicon phonon peak is shown in Fig. 2.8.

measured silicon phonon peaks shown in Fig. 2.9, remain almost perfectly Lorentzian, although broadened, at all positions. The large asymmetries observed in the Raman spectra of Fig. 2.7 are not seen here (Fig. 2.9).

A detailed analysis of the phonon peaks can only be achieved in combination with stress-modeling, such as finite element (FE) calculations or analytical stress models. After all stress values in a given sample structure have been calculated, the Raman spectrum can be simulated by adding up all Lorentz lines corresponding to the stress from each infinitesimal scattering volume under the laser spot (taking into account the intensity distribution of the laser spot). A comparison between the measured and calculated phonon shape should then help to extract more information from the measured phonon peaks. A comparison like that has not been performed, yet, and is also not shown in this thesis. Only the measurements with UV light show definite signs of a splitting of the measured Si phonon peak, or at least that the measured phonon consists of definitely more than one Lorentz line (Fig. 2.7). This should make it possible to perform the comparison of lineshapes mentioned above in the future.

2.8 Experimental Challenges with Stress Measurements

This section will present and discuss several challenges one faces when trying to measure mechanical stress in device structures with micro-Raman spectroscopy [15]. These challenges are not specific to the use of UV light, but some become more important or are more difficult to deal with than in the case of blue light. These challenges include:

- (i) Sample heating
- (ii) Raman scattering from structural sidewalls
- (iii) The influence of focusing/defocusing on the phonon shift
- (iv) The influence of room temperature

Each challenge will be discussed in the following sub-sections.

2.8.1 Sample Heating

The laser light is focussed through the microscope objective to a spot of around 1 μm in diameter. No matter how low the laser output power is chosen, the sample is always heated by the laser spot. Due to thermal expansion the silicon phonon shifts to lower energies with increasing temperature ($\approx 0.025 \text{ cm}^{-1}/\text{K}$). This downshift would look like tensile stress (chapter 3). Measuring the silicon phonon position as a function of laser output power showed the following values to be sufficiently small, so that shifts due to sample heating were smaller than 0.05 cm^{-1} , the typical measurement noise:

Blue light (458 nm): ≈ 10 mW

UV light (364 nm): ≈ 300 μ W

The output power for UV light is smaller by a factor of 30, the same factor that the probed sample volume is reduced through the smaller penetration depth of UV light.

2.8.2 Raman Scattering from Structural Sidewalls

The device structures investigated in this thesis consist mainly of silicon stripes separated by shallow trenches (for details see chapter 4). The trenches are always aligned along $\langle 110 \rangle$ directions, so that the trench sidewalls are always (110) faces. Looking at the selection rules given in Eq. (2.8), with the polarization of the incident and scattered light along [110], shows that backscattering from a (110) plane also measures the LO phonon, just as backscattering from the (001) plane does.

In the experimental setup used in this thesis (Fig. 2.1), the scattering geometry is such that the laser light reaches the sample in a (001) direction. The laser light is focussed through a microscope objective with a numerical aperture of 0.9. Looking at the path of the light leaving the objective lens in pure geometrical optics, some light shines on the sample at an angle of almost 65° to the optical axis. When the laser spot is focussed right on the edge of a silicon trench, some light would therefore also enter the (110) sidewall and the Raman scattered light from that sidewall would be collected by the objective the same way.

It is impossible to tell from the selection rules alone how big the contribution from Raman scattering at sidewalls to the total Raman signal is. The intensity distribution of the laser light leaving the microscope objective doesn't follow geometric optical paths, of course, but is rather determined by diffraction theory. It can only be assumed, that the contribution of the sidewalls to the overall Raman signal is small, although no proof exists so far, whether this assumption is right or wrong. In future investigations, when the measured phonon lineshapes are compared with calculated lineshapes from FE simulations, it may be possible to shed some light on this question.

2.8.3 Influence of Defocusing

As already mentioned in the previous section, the samples investigated in this thesis consist mainly of long silicon stripes separated by trenches etched into the silicon substrate. These trenches are about 400 nm deep. The investigated sample structures thus have height differences, which are about the same size as the wavelength of the laser light. The intensity distribution of the laser spot is governed by diffraction optics. The characteristic quantities of a diffraction limited objective lens are [17]:

The spatial resolution

$$r_{\min} = 0.61 \cdot \frac{\lambda}{n \cdot \sin \gamma}, \quad (2.14)$$

and the depth of focus where the intensity has dropped to 80% of the in-focus value

$$z_{\text{dof}} = \pm \frac{\lambda}{2 \cdot \tan^2 \gamma}. \quad (2.15)$$

Here, γ is the aperture angle, λ the laser wavelength, and n the index of refraction of the material between objective and sample. In the present case, $n = 1$ (air). The calculated values for blue and UV light are shown in Tab. 2.4.

While scanning across a 400 nm deep trench, the laser spot reaching the silicon surface at the top or bottom of a stripe or trench will be more or less in focus. To investigate whether this influences the position of the Raman signal, a flat silicon wafer was moved up and down under the microscope and the silicon phonon position recorded as a function of distance out of focus [15]. At the same time the intensity of the silicon phonon and a neighboring plasma line were also recorded. Both results are shown in Fig. 2.12.

To understand these results, the origin of the detected Raman signal has to be considered. If the incoming laser beam is perfectly aligned to the optical axis of the microscope (see Fig. 2.10), the objective generates an intensity distribution I_{im} around the geometric-optical focus like the intensity distribution in the focus of a diffraction-limited lens [17]. Equal energy surfaces have an ellipsoid shape around the geometric optical focus, with their main axis along the optical axis. This is shown schematically in Fig. 2.11.

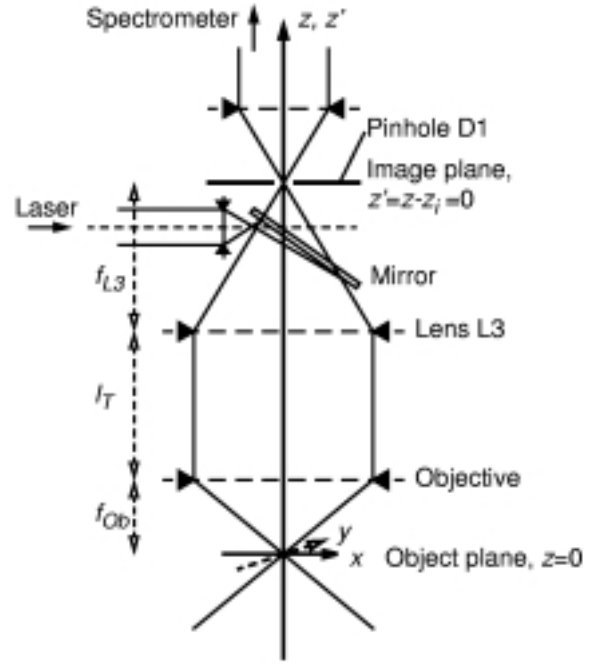


Fig. 2.10: Simplified optical scheme of the micro-Raman spectrometer shown in Fig. 2.1. The semi-transparent mirror (beam splitter) reflects the incoming laser light into the optical system consisting of lens L3 and the microscope objective, where it is focussed in the object plane in the focal point $x=y=z=0$. The Raman scattered light is focussed in the image plane at $x'=y'=z'=0$ (the pinhole D1), from where it is focussed onto the entrance slit of the spectrometer.

Wavelength λ (nm)	r_{\min} (μm)	z_{dof} (μm)
457.9 (Blue)	0.31	0.057
363.7 (UV)	0.25	0.043

Tab. 2.4: Spatial resolution, r_{\min} , and depth of focus, z_{dof} , of an objective with a numerical aperture of 0.9 for blue and UV light.

the intensity distribution in the focus of a diffraction-limited lens [17]. Equal energy surfaces have an ellipsoid shape around the geometric optical focus, with their main axis along the optical axis. This is shown schematically in Fig. 2.11.

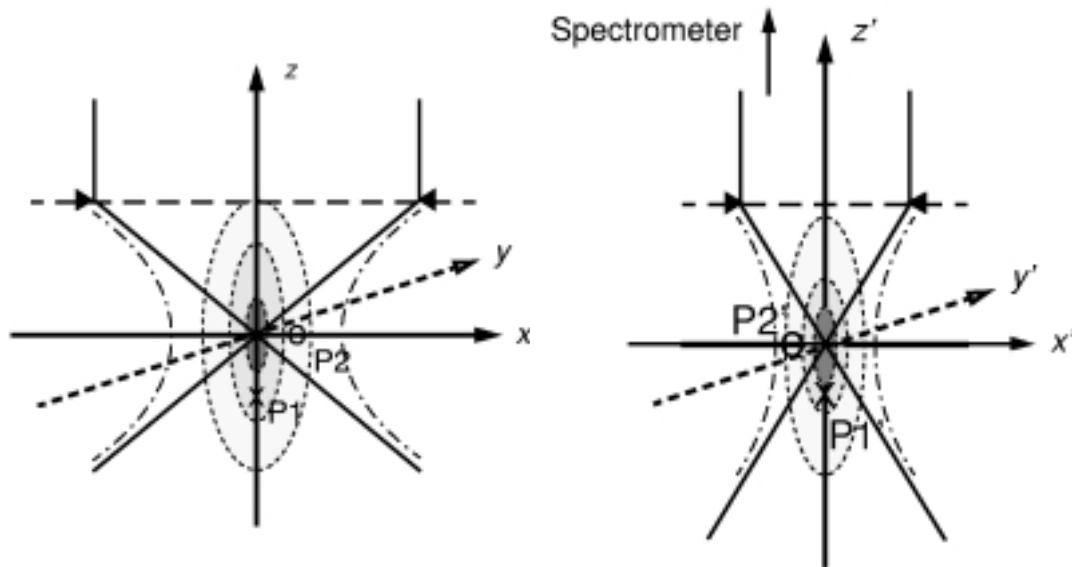


Fig. 2.11: *Left: Intensity distribution of the laser light in the object plane. The dashed ellipsoids mark equi-intensity planes. The dash-dotted hyperbola marks the width of the focus where the intensity has dropped to 50%. The points $P1$ and $P2$ are projected into the points $P1'$ and $P2'$ near the image plane. Right: Intensity distribution in the image plane. The image focus is at $x'=y'=z'=0$. $P1'$ and $P2'$ are the images of $P1$ and $P2$.*

An infinitesimal scattering volume within the focal point generates an intensity distribution I_{im} near the image plane, which is proportional to that of a diffraction limited lens (Fig. 2.11, right). A flat and homogeneous silicon sample in the focal plane produces an intensity distribution proportional to the convolution of the intensity scattered by the sample with the intensity I_{im} [18]. Any small shift of the scattering volume in x or z direction shifts the center of the intensity distribution in the image plane in $-x'$ or $-z'$ direction, following the rules of geometrical optics.

The pinhole D1 (Fig. 2.10) in the image plane cuts out the central part of the intensity distribution. The CCD detector integrates over this intensity behind the pinhole. As known from the principle of the confocal microscope the portion of the whole intensity reaching the receiver and the sensitivity to defocusing is determined by the pinhole diameter. To get a low sensitivity to defocusing a fairly large pinhole diameter was chosen. The pinhole also reduces stray light and background light generated by the glass of the objective lenses and the L3 lens (Fig. 2.10).

Shifting the sample along the z -axis (Fig. 2.10) will thus reduce the signal intensity as a whole, but should not influence the spectral positions. This behavior is shown in Fig. 2.12. The measured silicon phonon peak position deviates slightly as a function of defocus, z , but by less than $\pm 0.05 \text{ cm}^{-1}$ in the range of $-1 \mu\text{m} < z < 1 \mu\text{m}$. The intensities show almost the expected behavior. The highest intensity occurs as the sample is in the object plane $z = 0$. The depth of focus, taken at the point where the intensity has dropped to 80%, is twice as large as the calculated one (Tab. 2.4). The

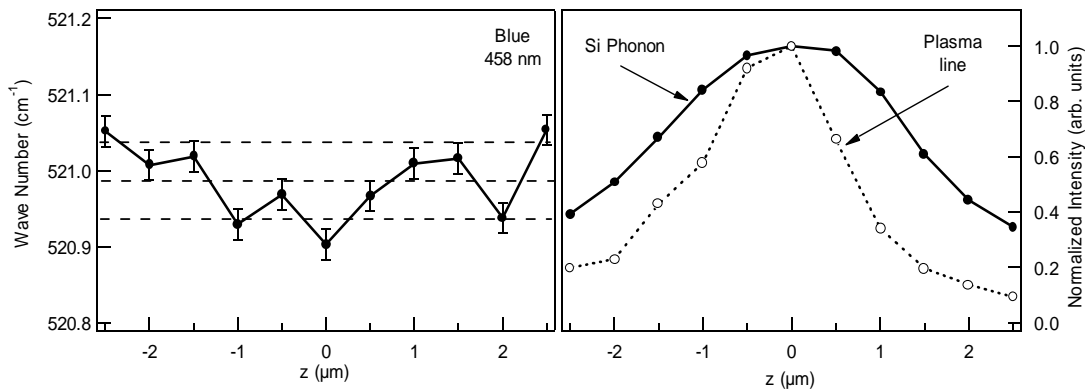


Fig. 2.12: *Left:* Silicon phonon peak position obtained with blue light (458 nm) as a function of z , the distance of the wafer from the focal plane. The phonon position deviates less than $\pm 0.05 \text{ cm}^{-1}$ from its mean value. *Right:* Intensities of the silicon phonon (left) and a neighboring plasma line obtained in a flat silicon wafer as a function of z .

reason for this discrepancy is unknown. The depth of focus for the plasma line is about one-half of that of the Raman line. This difference is understandable, because the reflected plasma light starts from a virtual focus twice as far from $z=0$ as the sample surface. Defocusing decreases the plasma line intensity thus more strongly than the Raman intensity. The behavior of the silicon phonon shift and the intensities of Raman and plasma light shown in Fig. 2.12 is the same as with UV light.

As long as the wafer surface is flat, almost no shift of the silicon phonon peak as a function of defocus can be observed. If the sample surface is no longer flat, but consists of trench structures, the picture changes. In this thesis, a strong dependence of the scanning direction with respect to the orientation of the entrance slit was found. As the laser spot is scanned across a silicon step on the wafer, the intensity distribution in the image plane (Fig. 2.11) moves slightly as the laser spot is located right on the step. This movement of the focus on the entrance slit was observed using a camera situated behind the entrance slit. The movement can be explained with the help of Fig. 2.11.

A sample shift in the x -direction shifts the intensity distribution in the image plane in the $-x'$ direction. If the intensity in the focus is not homogeneous (as in the case when the laser spot is right on top of a silicon step), then the intensity distribution in the image plane x',y' changes also and shifts the peak position. The intensity distribution in the entrance slit of the spectrometer is a picture of the intensity in the image plane $z'=0$ and the same intensity distribution occurs also on the CCD detector for each wavelength. If the movement on the entrance slit is perpendicular to the length of the slit, this movement will be transformed on the CCD as a shift in frequency. If the shift is along the length of the entrance slit, the intensity will also shift on the CCD, but not in the spectral direction but perpendicular to it. The lines of the CCD are binned together, so that this movement goes undetected. This behavior is shown in Fig. 2.13.

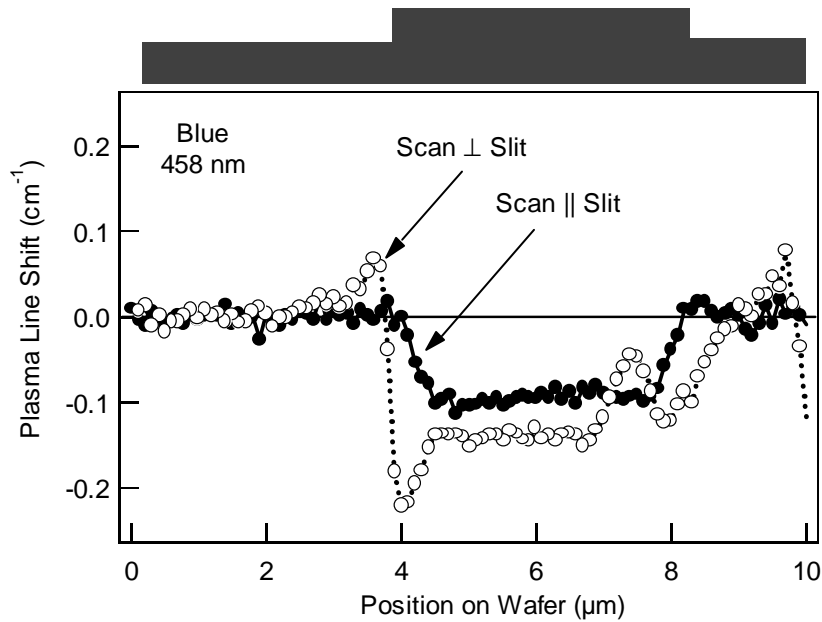


Fig. 2.13: *Shift of the plasma line position in the Raman spectrum as the laser spot (458 nm) is scanned across a silicon stripe shown schematically at the top of the figure. The plasma line shift is asymmetric, if the scanning direction is such that the shift of the intensity distribution on the entrance slit is perpendicular to the length of the slit (scan \perp slit). It is symmetrical, if the movement of the focal point on the entrance slit is along the length of the slit (scan \parallel slit).*

2.8.4 The Influence of Room Temperature

The commercial micro-Raman spectrometers used in this thesis are very susceptible to changes in room temperature. Changes in room temperature are transformed directly into spectral shifts of the peaks in the Raman spectra. These shifts are caused by small movements of the gratings, which are a result of differing thermal expansion of the various materials of the arms to which the gratings are attached.

Performing measurements over long periods of time, especially for several hours, make it possible to monitor the room temperature as a side effect. This is demonstrated in Fig. 2.14, showing two stress measurements with UV light (364 nm), which were performed over a time period of 12 hours each. Each trace consists of 3550 (!) measurement points taken in steps of $0.1 \mu\text{m}$ scanning across silicon device structures. The details of the stress measurements are not of interest here.

The two traces in each graph are the silicon phonon shift (the large movement is due to stress in the underlying silicon device structures) and the shift of a neighboring plasma line (offset by -1 cm^{-1} for better viewing). The top and bottom graph of Fig. 2.14 show the same measurement performed during two consecutive nights. The

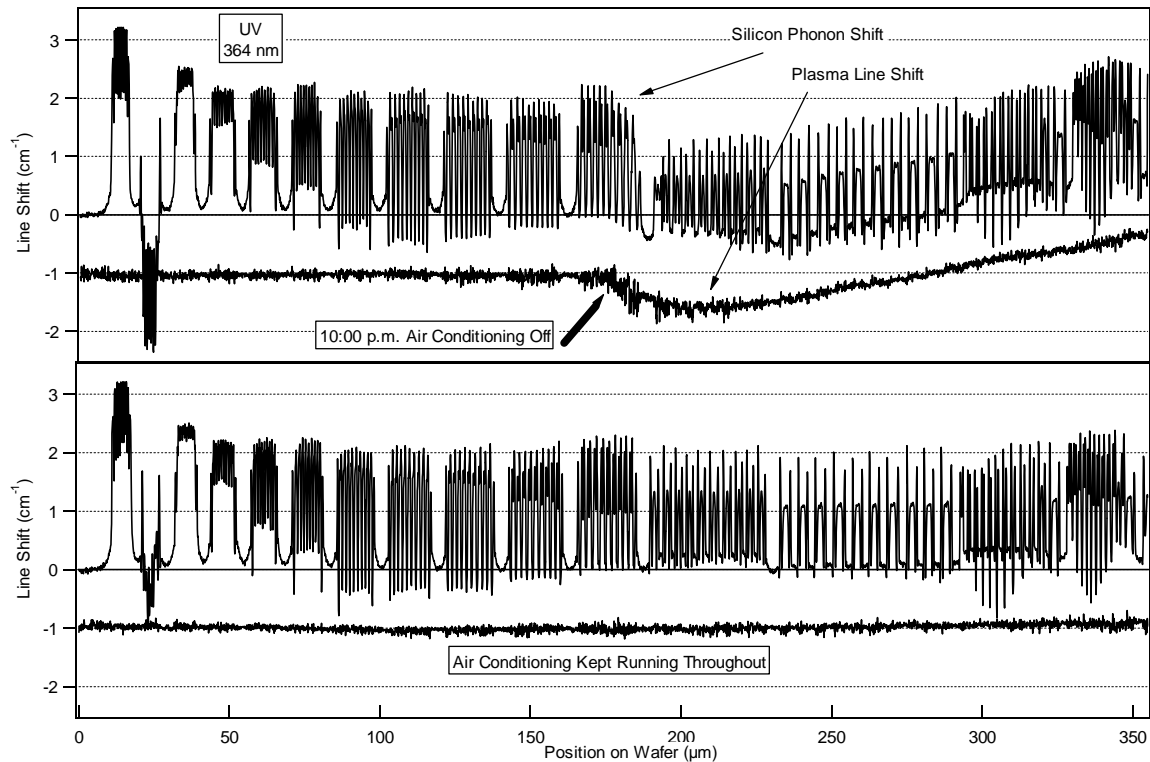


Fig. 2.14: Influence of room temperature on stress measurements with UV light (364 nm) performed over a time period of 12 hours. *Top graph:* The two traces are the silicon phonon shift (the large movement is due to stress in the underlying silicon device structures) and the shift of a neighboring plasma line (offset by -1 cm^{-1} for better viewing). The measurement started at 4 p.m. and ran till 4 a.m. At 10 p.m. the air conditioning in the lab was turned off, resulting in a room temperature change, leading to a shift in the measured lines. *Bottom graph:* The same measurement as in the top graph with the air conditioning running throughout. As the room temperature remains stable no changes in the plasma line position or in the silicon phonon shift can be observed.

measurements started at 4 p.m. and ran till 4 a.m. the next morning. During the measurement shown in the top graph, the air conditioning in the lab was turned off at 10 p.m., which resulted first in a drop and later in a continuous increase of room temperature. These changes are seen directly as a shift in the plasma line and also in the general trend of the silicon phonon shift. The bottom graph shows the same measurement as in the top graph, performed again one night later with the air conditioning running all night. As the room temperature remained stable no changes in the plasma line position or in the silicon phonon shift can be observed.

The measurements shown in Fig. 2.14 demonstrate the necessity to always monitor shifts in the plasma lines during stress measurements. Subtracting the plasma line shift from the silicon phonon shift in the top graph of Fig. 2.14 will result in a constant "baseline" of the silicon phonon shift, compensating the shift due to changes in room temperature.

3 Theory: Optical Phonons and Stress

This chapter presents the theoretical background on the influence of mechanical stress on the optical phonon modes of silicon. Micro-Raman spectroscopy measures the energy of the optical phonon(s) of silicon. This energy is influenced by strain in the material via the phonon deformation potentials (section 3.1). The amount of strain is determined via the elasticity constants from external or internal stress according to Hook's law (section 3.2). The stress induced in the silicon during device processing can be modeled by analytical film stress models or finite element (FE) simulations (section 3.3). The stress in the silicon is caused by thermal mismatch, volume expansion or internal stress of different nitride and oxide layers, deposited or grown on the silicon substrate during device processing.

The main aspects of the theory will be shown, including the general solution for the two most common forms of stress, uniaxial and biaxial stress. The theoretical tools can be used to compare calculated Raman shifts to measurements in device structures, caused by stresses induced through the different process steps of the shallow trench isolation process (chapter 4).

3.1 Phonons and Strain

The effect of strain on the Raman-active optical phonons of crystalline materials has been studied quite extensively since the 1970's. Ganesan et al. [19] and Anastassakis [20] were among the first to address the morphic effect of stress on the optical phonon modes. They found, that in the presence of a symmetric strain, the triple degeneracy of the $k = 0$ optical phonon with frequency ω_0 is lifted, due to anisotropic changes in the lattice constants. Each of the strain-split phonons exhibits its own frequency Ω , which for the strain ϵ in the elastic regime, varies linearly with the components $\epsilon_{\nu\nu}$. Observation of a shift $\Delta\Omega = \Omega - \omega_0$ may therefore be attributed to a tensile or compressive strain present in the scattering volume.

In the absence of strain, the mode frequency ω_j is associated with a diagonal effective force constant K_j^0 , which is in general a second rank tensor, according to the definition

$$K_{j,\alpha\beta}^0 = \omega_j^2 \delta_{\alpha\beta} \quad (3.1)$$

where $\delta_{\alpha\beta}$ is the Kronecker delta. In the presence of a symmetric strain, the force constant K_j^0 and the frequency ω_j can be expanded to terms linear in $\epsilon_{\nu\nu}$:

$$\Omega_j \cong \omega_j + \Delta\Omega_j \quad (3.2)$$

$$\mathbf{K}_{j,\alpha\beta} \cong \mathbf{K}_{j,\alpha\beta}^0 + \Delta\mathbf{K}_{j,\alpha\beta} \quad (3.3)$$

with

$$\Delta\mathbf{K}_{j,\alpha\beta} = \sum_{uv} \left(\frac{\partial \mathbf{K}_{j,\alpha\beta}}{\partial \epsilon_{uv}} \right) \epsilon_{uv} \equiv \sum_{uv} \mathbf{K}_{j,\alpha\beta uv} \epsilon_{uv}. \quad (3.4)$$

For silicon, the fourth rank force tensor $\mathbf{K}_{\alpha\beta uv}$ has only three independent elements in the crystal coordinate system $x = [100]$, $y = [010]$, $z = [001]$:

$$\begin{aligned} \mathbf{K}_{1111} = \mathbf{K}_{2222} = \mathbf{K}_{3333} = \mathbf{K}_{11} &\equiv p, \\ \mathbf{K}_{1122} = \mathbf{K}_{1133} = \mathbf{K}_{2233} = \mathbf{K}_{12} &\equiv q, \\ \mathbf{K}_{1212} = \mathbf{K}_{1313} = \mathbf{K}_{2323} = \mathbf{K}_{44} &\equiv r. \end{aligned} \quad (3.5)$$

All other elements are zero from symmetry considerations. \mathbf{K}_{11} , \mathbf{K}_{12} and \mathbf{K}_{44} are the components in suppressed notation according to [21]. They are also called the phonon deformation potentials (PDP's), because they connect the strain components with the changes induced on the phonon frequency the same way the elastic constants (elastic compliance tensor components) connect the strain components with stresses (Hooke's law).

The new phonon frequencies are then given by diagonalization of the secular equation

$$\left| \Delta\mathbf{K}_{j,\alpha\beta} - \lambda_j \delta_{\alpha\beta} \right| = 0 \quad (3.6)$$

with

$$\lambda_j = \Omega_j^2 - \omega_j^2 = (\Omega_j - \omega_j)(\Omega_j + \omega_j) \cong \Delta\Omega_j \cdot 2\omega_j. \quad (3.7)$$

Here ω_j is the unstrained phonon frequency, Ω_j the strain-split frequency and $\Delta\Omega$ the frequency shift due to strain. $\Delta\Omega_j$ is small compared to ω_j , and therefore

$$\Delta\Omega_j = \frac{\lambda_j}{2\omega_j}, \quad j=1,2,3. \quad (3.8)$$

Combining equations (3.1) to (3.6) results in the well known form of the secular equation:

$$\begin{vmatrix} p\epsilon_{11} + q(\epsilon_{22} + \epsilon_{33}) - \lambda & 2r\epsilon_{12} & 2r\epsilon_{13} \\ 2r\epsilon_{12} & p\epsilon_{22} + q(\epsilon_{11} + \epsilon_{33}) - \lambda & 2r\epsilon_{23} \\ 2r\epsilon_{13} & 2r\epsilon_{23} & p\epsilon_{33} + q(\epsilon_{11} + \epsilon_{22}) - \lambda \end{vmatrix} = 0 \quad (3.9)$$

Solving this equation for the eigenvalues, λ_j , results in relations between the Raman frequency of each of the three modes as a function of strain. The corresponding polarizations are given by the eigenvectors.

The secular equation (3.9) is given in the crystal coordinate system. But, in microelectronic devices, most structures like trenches and film edges are oriented along (110) directions. The stresses induced by these edges will then also be along those directions. It is therefore often much easier to solve the secular equation not in the crystal coordinate system, but in the sample coordinate system defined by

$$x' = \frac{1}{\sqrt{2}}[110], \quad y' = \frac{1}{\sqrt{2}}[\bar{1}10], \quad z' = [001].$$

Anastassakis [22] and De Wolf [23] have proposed several different methods to accomplish this. Switching back and forth between the two coordinate systems often leads to confusion and errors in choosing the correct eigenvectors. The problem will therefore be treated entirely in the sample coordinate system, thus avoiding to switch back and forth between both coordinate systems as De Wolf did in [23].

First, the force tensor is rotated to the sample coordinate system, to get the secular equation in the sample system. This straight forward tensor rotation results in the new force tensor components:

$$\begin{aligned} K'_{1111} &= K'_{2222} = p', & K'_{3333} &= p, \\ K'_{1122} &= q', & K'_{1133} &= K'_{2233} = q, \\ K'_{1212} &= \frac{p-q}{2}, & K'_{1313} &= K'_{2323} = r, \end{aligned} \quad (3.10)$$

with

$$p' = \frac{p+q}{2} + r, \quad q' = \frac{p+q}{2} - r. \quad (3.11)$$

This gives the secular equation in the sample axis system:

$$\begin{vmatrix} p'\epsilon'_{11} + q'\epsilon'_{22} + q\epsilon'_{33} - \lambda & (p-q)\epsilon'_{12} & 2r\epsilon'_{13} \\ (p-q)\epsilon'_{12} & q'\epsilon'_{11} + p'\epsilon'_{22} + q\epsilon'_{33} - \lambda & 2r\epsilon'_{23} \\ 2r\epsilon'_{13} & 2r\epsilon'_{23} & p\epsilon'_{33} + q(\epsilon'_{11} + \epsilon'_{22}) - \lambda \end{vmatrix} = 0. \quad (3.12)$$

The strain tensor ε' must now also be given in the sample axis system.

It is possible to give general solutions to (3.9) or (3.12) but not practical. In many cases, some of the components will be zero, depending on the symmetry of the applied stress. The general solutions to the two most common cases, uniaxial and biaxial stress (Fig. 3.1), which apply to many situations in microelectronic device structuring, will be given in the next sections.

3.2 Phonons and Stress

Fig. 3.1 shows a schematic drawing of the stress caused in the silicon substrate under a film, such as nitride. The figure is meant to be the cross-section through the center of a long line on silicon. In that case, the stress components along the film edges (σ_y) are zero. In the center under the film, the stress caused by the film edges is almost exactly uniaxial (left drawing, Fig. 3.1). Close to the film edge, the stress is biaxial (right drawing, Fig. 3.1), with components σ_x , σ_z and shear component τ_{xz} . Solutions of the secular equation and resulting phonon shifts for both cases are presented in the following sections.

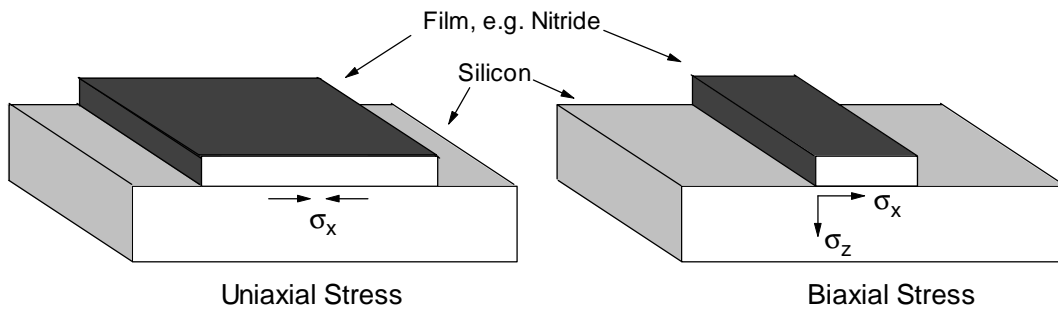


Fig. 3.1: *Cross-sectional view of uniaxial (left) and biaxial (right) stress in the silicon substrate under a stress-causing film, such as nitride.*

3.2.1 Uniaxial Stress

Assuming uniaxial stress, the strain tensor components have to be calculated first according to Hooke's law:

$$\varepsilon = S \sigma \quad (3.13)$$

The elastic compliance tensor S , a fourth rank tensor, has a relatively simple form due to the cubic symmetry of silicon. In suppressed notation [21] in the crystal coordinate system [100], [010], [001] it can be written as:

$$S = \begin{pmatrix} S_{11} & S_{12} & S_{12} & 0 & 0 & 0 \\ S_{12} & S_{11} & S_{12} & 0 & 0 & 0 \\ S_{12} & S_{12} & S_{11} & 0 & 0 & 0 \\ 0 & 0 & 0 & \frac{1}{4}S_{44} & 0 & 0 \\ 0 & 0 & 0 & 0 & \frac{1}{4}S_{44} & 0 \\ 0 & 0 & 0 & 0 & 0 & \frac{1}{4}S_{44} \end{pmatrix} \quad (3.14)$$

After rotation to the sample axis system the compliance tensor has components:

$$S' = \begin{pmatrix} \frac{1}{2}(S_{11} + S_{12}) + \frac{1}{4}S_{44} & \frac{1}{2}(S_{11} + S_{12}) - \frac{1}{4}S_{44} & S_{12} & 0 & 0 & 0 \\ \frac{1}{2}(S_{11} + S_{12}) - \frac{1}{4}S_{44} & \frac{1}{2}(S_{11} + S_{12}) + \frac{1}{4}S_{44} & S_{12} & 0 & 0 & 0 \\ S_{12} & S_{12} & S_{11} & 0 & 0 & 0 \\ 0 & 0 & 0 & \frac{1}{4}S_{44} & 0 & 0 \\ 0 & 0 & 0 & 0 & \frac{1}{4}S_{44} & 0 \\ 0 & 0 & 0 & 0 & 0 & \frac{1}{2}(S_{11} - S_{12}) \end{pmatrix} \quad (3.15)$$

Assuming a uniaxial stress $\sigma_x = \sigma_0$ (100) along the x' direction (in the sample system), leads to the strain tensor components:

$$\varepsilon' = \sigma_0 \begin{pmatrix} \frac{1}{2}(S_{11} + S_{12}) + \frac{1}{4}S_{44} & 0 & 0 \\ 0 & \frac{1}{2}(S_{11} + S_{12}) - \frac{1}{4}S_{44} & 0 \\ 0 & 0 & S_{12} \end{pmatrix} \quad (3.16)$$

Filling this into (3.12) results in a diagonal secular equation, from which the eigenvalues are easily obtained:

$$\begin{aligned} \lambda_1 &= \left[\frac{1}{2}(p + q)S_{11} + \frac{1}{2}(p + 3q)S_{12} + \frac{1}{2}rS_{44} \right] \sigma_0 \\ \lambda_2 &= \left[\frac{1}{2}(p + q)S_{11} + \frac{1}{2}(p + 3q)S_{12} - \frac{1}{2}rS_{44} \right] \sigma_0 \\ \lambda_3 &= [pS_{12} + q(S_{11} + S_{12})] \sigma_0 \end{aligned} \quad (3.17)$$

The corresponding eigenvectors giving the polarizations of the Raman modes under stress are (in the sample system):

$$v'_{1_st} = (100), v'_{2_st} = (010), v'_{3_st} = (001). \quad (3.18)$$

Next the Raman tensors also have to be rotated to the sample system, resulting in

$$\mathbf{R}'_1 = \frac{1}{\sqrt{2}} \begin{pmatrix} 0 & 0 & d \\ 0 & 0 & d \\ d & d & 0 \end{pmatrix}, \quad \mathbf{R}'_2 = \frac{1}{\sqrt{2}} \begin{pmatrix} 0 & 0 & d \\ 0 & 0 & -d \\ d & -d & 0 \end{pmatrix}, \quad \mathbf{R}'_3 = \begin{pmatrix} d & 0 & 0 \\ 0 & -d & 0 \\ 0 & 0 & 0 \end{pmatrix} \quad (3.19)$$

The related polarization vectors are

$$\mathbf{v}'_1 = \frac{1}{\sqrt{2}} [1 \bar{1} 0], \quad \mathbf{v}'_2 = \frac{1}{\sqrt{2}} [1 1 0], \quad \mathbf{v}'_3 = [001]. \quad (3.20)$$

The Raman tensors in the presence of stress are now calculated from

$$\mathbf{R}'_{i_st} = \sum_{k=1}^3 \frac{\partial \mathbf{v}'_k}{\partial \mathbf{v}'_{i_st}} \cdot \mathbf{R}'_k, \quad (3.21)$$

resulting in

$$\mathbf{R}'_{1_st} = \begin{pmatrix} 0 & 0 & d \\ 0 & 0 & 0 \\ d & 0 & 0 \end{pmatrix}, \quad \mathbf{R}'_2 = \begin{pmatrix} 0 & 0 & 0 \\ 0 & 0 & -d \\ 0 & -d & 0 \end{pmatrix}, \quad \mathbf{R}'_3 = \begin{pmatrix} d & 0 & 0 \\ 0 & -d & 0 \\ 0 & 0 & 0 \end{pmatrix} \quad (3.22)$$

For backscattering from the $z' = [001]$ direction, it follows from the Raman selection rule with $\mathbf{e}_i = \mathbf{e}_s = (100)$, that only the third Raman mode can be observed. The relation between the measured Raman shift and the stress is then obtained from (3.8) to be

$$\Delta\Omega_3 = \frac{1}{2\omega_0} [pS_{12} + q(S_{11} + S_{12})] \sigma_0 \quad (3.23)$$

The PDP's (p , q , r) and the elasticity constants (S_{ij}) are material properties. Experimental and theoretical values for the phonon deformation potentials (p , q and r), determined by different authors, are summarized in Tab. 3.1. The experimental values from Chandrasekhar [24] and Anastassakis [25] differ by as much as 25%. So,

source year	Experiment		Theory		
	[24] 1978	[25] 1990	[26] 1985	[27] 1989	[25] 1990
p / ω_0^2	-1.49±0.07	-1.85±0.06	-1.63	-1.67	-2.11
q / ω_0^2	-1.97±0.09	-2.31±0.06	-1.89	-2.13	-2.57
r / ω_0^2	-0.61±0.03	-0.71±0.02	-0.6	-0.97	-0.69

Tab. 3.1: Comparison of experimental and theoretical values for the phonon deformation potentials of Si.

depending on the set of values used in (3.23), the stress determined from the Raman shift varies. Assuming a uniaxial stress σ_0 of -1 GPa, the Raman shift $\Delta\Omega_3$ using the PDP's from [24] is 2.01 cm^{-1} , whereas the PDP's from [25] give a value of 2.29 cm^{-1} . As a general rule of thumb, for uniaxial stress the following relation between Raman shift and stress is often used:

$$\Delta\omega = -2 \times 10^{-9} \sigma_0 \quad (3.24)$$

Here $\Delta\omega$ is given in units of cm^{-1} and σ_0 in Pascal (Pa). A compressive stress of -1 GPa will thus result in a Raman shift of 2 cm^{-1} .

3.2.2 Biaxial Stress

The assumption of uniaxial stress is often a good approximation in the center of lines or at least a certain distance away from the edges. This assumption is most certainly wrong right at the edge, where other stress components play an equal role. The general solution for a stress tensor of the following form will now be given (compare Fig. 3.1):

$$\sigma' = \begin{pmatrix} \sigma_x & 0 & \tau_{xz} \\ 0 & 0 & 0 \\ \tau_{xz} & 0 & \sigma_z \end{pmatrix} \quad (3.25)$$

Eq. (3.25) is given in the sample coordinate system. The resulting strain tensor has components:

$$\varepsilon' = \begin{pmatrix} \left(\frac{S_{11} + S_{12}}{2} + \frac{S_{44}}{4} \right) \sigma_x + S_{12} \sigma_z & 0 & \frac{1}{2} S_{44} \tau_{xz} \\ 0 & \left(\frac{S_{11} + S_{12}}{2} - \frac{S_{44}}{4} \right) \sigma_x + S_{12} \sigma_z & 0 \\ \frac{1}{2} S_{44} \tau_{xz} & 0 & S_{12} \sigma_x + S_{11} \sigma_z \end{pmatrix} \quad (3.26)$$

The secular equation (3.12) is now no longer diagonal, but one eigenvalue can immediately be found from

$$q \varepsilon'_{11} + p \varepsilon'_{22} + q \varepsilon'_{33} - \lambda = 0, \quad (3.27)$$

resulting in

$$\lambda_2 = \frac{1}{2} [(p + q)S_{11} + (p + 3q)S_{12} - rS_{44}] \sigma_x + [qS_{11} + (p + q)S_{12}] \sigma_z. \quad (3.28)$$

The other two eigenvalues are given by

$$\begin{aligned}\lambda_1 &= \frac{1}{2} \left[A + B + \sqrt{(A - B)^2 + 4C^2} \right] \\ \lambda_3 &= \frac{1}{2} \left[A + B - \sqrt{(A - B)^2 + 4C^2} \right]\end{aligned}\quad (3.29)$$

with

$$\begin{aligned}A &= \frac{1}{2} [(p + q)S_{11} + (p + 3q)S_{12} + rS_{44}] \sigma_x + [qS_{11} + (p + q)S_{12}] \sigma_z \cdot \\ B &= [qS_{11} + (p + q)S_{12}] \sigma_x + [pS_{11} + 2qS_{12}] \sigma_z \cdot\end{aligned}\quad (3.30)$$

$$C = rS_{44} \tau_{xz}$$

The corresponding normalized eigenvectors are

$$v'_{1_st} = \frac{1}{\sqrt{X^2 + 1}} (X, 0, 1), \quad v'_{2_st} = (0, 1, 0), \quad v'_{3_st} = \frac{1}{\sqrt{Y^2 + 1}} (Y, 0, 1) \quad (3.31)$$

with

$$\begin{aligned}X &= \frac{1}{2C} \left[A - B + \sqrt{(A - B)^2 + 4C^2} \right] \\ Y &= \frac{1}{2C} \left[A - B - \sqrt{(A - B)^2 + 4C^2} \right].\end{aligned}\quad (3.32)$$

The Raman tensors in the presence of stress are again found from (3.21) and (3.31) to be:

$$R'_{1_st} = \frac{1}{\sqrt{X^2 + 1}} \begin{pmatrix} d & 0 & Xd \\ 0 & -d & 0 \\ Xd & 0 & 0 \end{pmatrix}, \quad R'_{2_st} = \begin{pmatrix} 0 & 0 & 0 \\ 0 & 0 & -d \\ 0 & -d & 0 \end{pmatrix}, \quad R'_{3_st} = \frac{1}{\sqrt{Y^2 + 1}} \begin{pmatrix} d & 0 & Yd \\ 0 & -d & 0 \\ Yd & 0 & 0 \end{pmatrix} \quad (3.33)$$

For backscattering from the $z' = [001]$ direction with the incident and scattered light polarized along (100), the first and third mode can now be observed. The second mode is invisible. The intensities of the modes are given by

$$I_k \propto | \mathbf{e}_i \cdot \mathbf{R}_k \cdot \mathbf{e}_j |^2 \quad (3.34)$$

resulting in

$$I_1 = \frac{d^2}{X^2 + 1}, \quad I_2 = 0, \quad I_3 = \frac{d^2}{Y^2 + 1}. \quad (3.35)$$

So, depending on the values of X and Y , the first and/or third mode corresponding to the polarization vector of (3.31) will be observed, while the second mode is invisible.

3.3 Film Stress Models

So far it has only been shown how the Raman modes change under the assumption of a certain stress state, such as uniaxial or biaxial stress. *A priori* the stress state is unknown. If the stress is assumed to be purely uniaxial along the interface of the film and the silicon substrate, only one optical phonon mode is observed in the Raman spectrum. The energy of this phonon is directly related to the amount of stress. This approximation is usually very good far enough from the film edge. Right at the film edge the stress is at least biaxial (Fig. 3.1). The Raman spectrum now shows the superposition of two optical phonon modes, whose energies are a complex combination of all stress components. Modeling is therefore required to extract the values for each stress component from the Raman measurements. A stress model delivers the stress components from which the Raman spectrum can be calculated. By comparison of the theoretical and experimental results the model can be validated and quantified.

Modeling of stress in a given sample structure can be done either through the use of analytic film stress models or through finite element calculations.

3.3.1 Analytic Film Stress Models

Several theoretical models exist to describe the stress in a film and substrate arising from the edges of an otherwise uniformly stressed film. The first model was the so called "edge force" model by Hu [28]. This simple model describes the stress induced by a single film edge as a constant force acting at the edge parallel to the silicon/layer interface. In the case of a concentrated line force F_x tangential to the boundary of a half space, the substrate stress components are given in the following form ([28] and references cited therein):

$$\begin{aligned}\sigma_x &= -\frac{2F_x}{\pi} \frac{x^3}{(x^2 + z^2)^2}, \\ \sigma_z &= -\frac{2F_x}{\pi} \frac{xz^2}{(x^2 + z^2)^2}, \\ \tau_{xz} &= -\frac{2F_x}{\pi} \frac{x^2z}{(x^2 + z^2)^2}.\end{aligned}\tag{3.36}$$

This concentrated edge force model does not describe the force exerted by the film edge on the underlying substrate correctly, because the force is distributed over a considerable length near the film edge. Hu therefore developed a distributed force model [28] in which the change in film stress with position is balanced by a distributed tangential force in the substrate. The self-consistent expression for the stress in a semi-infinite thin film is given by

$$\sigma_{\text{fxx}}(x) = \sigma_0 - \frac{2h}{K\pi} \int_0^{\infty} \frac{\partial \sigma_{\text{fxx}}(u)}{\partial u} \frac{du}{x-u} \quad (3.37)$$

with

$$K = \frac{E_s(1 - \nu_f^2)}{E_f(1 - \nu_s^2)}. \quad (3.38)$$

In the above expression σ_0 is the stress in the film without edges and h the thickness of the film. E_i and ν_i are the Young modulus and the Poisson's ratio of the film (subscript f) and substrate (subscript s). The corresponding expression for the stress in the substrate is

$$\sigma_s(x, z) = -\frac{2h}{\pi} \int_0^{\infty} G(x-u, z) \frac{\partial \sigma_{\text{fss}}(u)}{\partial u} du \quad (3.39)$$

where σ_s stands for σ_x , σ_z or τ_{xz} and $G(x-u, z)$ for the corresponding distribution function from (3.36).

This model considers only a single edge. In microelectronic devices, structures consist of stripes or squares in which two edges are often close together, so that the stress from both edges start to overlap. Several approaches have been published to superpose the existing single edge solutions. Vanhellemont calculated the superposition from the concentrated edge force model [29]. Fischer and Richter used the distributed force model to find analytic expressions for the stress in a film with two edges [30]. Atkinson and coworkers also found an analytic approximation for the stress in film stripes [31] based on Hu's distributed force model [28], very similar to the one given by Fischer and Richter [30]. According to [31] and [30] the film stress in a thin film stripe is given in a compact form by

$$\sigma_f(x) = \sigma_0 \left[1 - \frac{\sum_{i=1}^2 \exp\left(-\alpha \sqrt{\frac{K \cdot |x - X_i|}{h}}\right)}{\sum_{j=1}^2 \exp\left(-\alpha \sqrt{\frac{K \cdot |X_j - X_i|}{h}}\right)} \right] \quad (3.40)$$

In this expression σ_0 is again the stress of the uniform film, h the film thickness, and X_1 and X_2 the position of the left and right edges of the film stripe. The factor α has a value of 0.945 in [31] and a value of 0.798 in [30]. According to [31], the value of 0.945 results in better agreement with the numerical solution of Eq. (3.37).

Equation (3.40) describes the film stress much better than the simple superposition of the edge force model. It correctly describes the decrease of film stress in the center of stripes as they become narrower. Fig. 3.2 shows this decrease for the case of 200nm thick nitride stripes on silicon. The stress in the center of the stripes decreases with decreasing stripe width.

If the film stripe is not placed on bulk silicon, but on a silicon mesa, as would be the case for silicon active areas separated by shallow trenches, the film stress can relax even further through an increased deformation of the mesa. Fischer and colleagues have found an analytic expression for the corresponding film stress, which is very similar to Eq. (3.40), but includes the height of the additional mesa as well. The film stress of a film stripe on top of a mesa of height H is then given by [32]:

$$\sigma_f(x) = \sigma_0 \left[1 - \frac{\sum_{i=1}^2 \exp\left(-\alpha \sqrt{\frac{\mathbf{K} \cdot |x - X_i|}{h + \mathbf{K} \cdot H}}\right)}{\sum_{j=1}^2 \exp\left(-\alpha \sqrt{\frac{\mathbf{K} \cdot |X_j - X_i|}{h + \mathbf{K} \cdot H}}\right)} \right] \quad (3.41)$$

The further reduction in film stress due to the additional deformation of the underlying mesa is indicated in Fig. 3.2 by the dotted lines.

So far only expressions for the film stress have been given in (3.40) and (3.41). The stress in the substrate still needs to be calculated by solving Eq. (3.39) for each stress component. The integral of Eq. (3.39) has to be solved numerically. Several papers have been published, which show a comparison of the substrate stress calculated

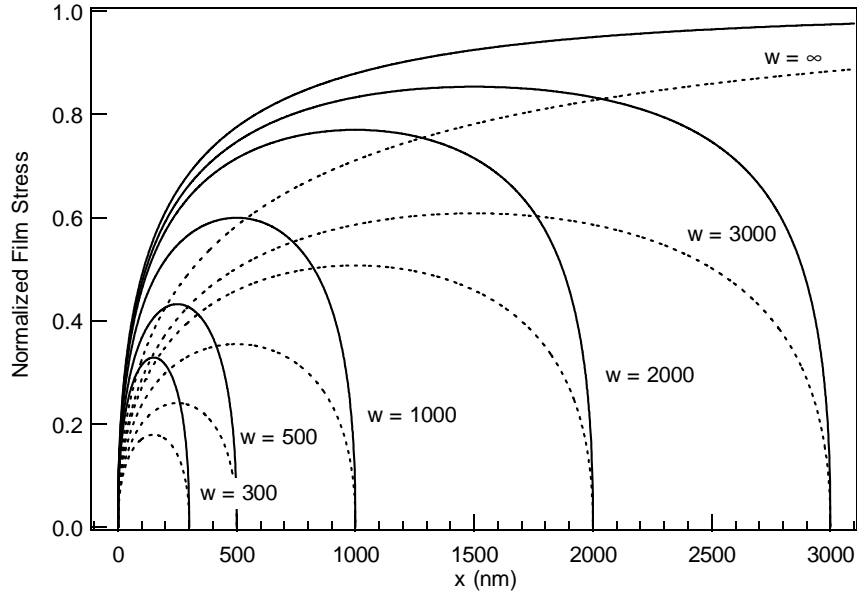


Fig. 3.2: Calculated film stress σ_x for 200 nm thick nitride stripes of different widths w (in nm) on silicon substrate. A normalized film stress of 1.0 corresponds to the stress of the uniform film. The film stress in the center of the stripe decreases with decreasing stripe width. The solid lines are the film stress in nitride stripes on bulk silicon. The dotted lines show the film stress in nitride stripes on top of a 380 nm high silicon mesa of equal width as the film stripe.

either with the edge-force model or the distributed force model (or both) with experimental measurements [23, 33, 34]. The distributed force model generally results in better fits to the experimental data, as expected.

All of the published results in [23, 33, 34] have been obtained with blue laser light (458 nm) and always in or around film stripes on bulk silicon. The fits of the calculated substrate stress to the experimental data are generally quite good. This agreement is a result of the large penetration depth of blue light. Blue light penetrates 320 nm into silicon. To calculate the Raman shifts for blue light, the theoretically calculated substrate stress also has to be averaged over this depth. The areas close to the surface and close to the film edge, where the stress models given by Hu are no longer valid [28], are thus negligible. Calculating the Raman shifts for a penetration depth of only 12 nm, as would be the case for UV light, gives much more weight to these problematic areas and leads to wrong results.

In addition, none of the above mentioned publications deal with substrate stress in mesa-like device structures. The distribution functions used to calculate the substrate stress are also only valid for a semi-infinite bulk substrate. So far, no papers have been published which treat the stress in mesa structures analytically. The application of the analytical film stress models and the resulting calculation of substrate stress to mesa structures seems to be rather difficult. Indications of the influence of a mesa on the film stress have been shown in [32], but not the resulting substrate stress. This problem can apparently only be solved sufficiently by finite element calculations.

3.3.2 Finite Element Calculations

The comparison between calculated and measured Raman shift shown in chapter 4 of this thesis are based on finite element calculations for the reasons discussed in the previous section. The finite element calculations¹ were performed using the 2D process simulator IMPACT-4 [45] and the FE code DIFOX-3D [44].

To compare the measured Raman shifts with the stress calculated by FE, the calculated stress components have to be averaged according to the experimental conditions. First, the Raman shifts according to the theory presented in section 3.2 have to be calculated for all nodes in the sample structure from the surface to the depth determined by the penetration of the used laser light. The resulting Raman modes are then averaged in depth according to the exponential decay of the light into and out of the material (chapter 2.6). Secondly, those depth-averaged values have to be averaged over the size of the laser spot assuming a Gaussian intensity distribution. This procedure is only an approximation, since in reality a Lorentz curve would have to be added up for each node, as discussed in chapter 2 (see also addendum to [23]).

¹ FE simulations performed by T. Hoffmann, IEMN-ISEN, Villeneuve d'Ascq Cédex, France

4 Mechanical Stress Measurements

This chapter presents the measurement of mechanical stress using micro-Raman spectroscopy with blue light and for the first time also with ultra violet (UV) light for excitation [37]. During the course of this chapter, the advantage of UV over blue light will be demonstrated. This advantage is mainly caused by the greatly reduced penetration depth of the laser light into the material. Averaging of stress is thus significantly reduced. Areas of high stress, occurring at film and structural edges, can be seen with UV light, which have previously been averaged away by the large penetration depth of blue light.

The measurement of mechanical stress will be shown in device structures processed with two different shallow trench isolation (STI) processes. STI is an important future isolation technique, which is already used widely in current 0.25 μm and 0.18 μm technology generations.

This chapter, therefore, starts with an overview of the STI processing steps, explaining the similarities and differences of the two investigated processes. It follows a detailed discussion of the influence of the different process parameters on the amount of mechanical stress introduced into the silicon substrate. Some of the stress results will be compared to theoretical calculations using the theory described in chapter 3.

Stress measurements in sample structures smaller than the laser spot will be shown and discussed for the first time [38, 40, 41]. Especially UV light is sensitive to stress changes also in very small structures, but the interpretation of those measurements has to be done with care. The stress is averaged over the laser spot area and can appear significantly different in structures smaller than the laser spot compared to structures bigger than the laser spot.

This chapter is structured as follows: First, the STI processes are described in detail (section 4.1). Then, the mechanical stress caused by the various process steps is shown and discussed (section 4.2). More precisely: The influence of process parameter variations such as different nitride and sidewall oxide thicknesses (section 4.2.1), different trench fill methods (sections 4.2.2 and 4.2.3), trench oxide densification in wet or dry ambient (section 4.2.2), and the influence of wet and dry pre-gate oxidation on the amount of stress and the formation of defects and a degradation of diode leakage (4.2.4) will be presented. Section 4.2.5 summarizes the evolution of mechanical stress through one of the two STI processes. This chapter closes with an overall summary of the main results (section 4.3).

4.1 Shallow Trench Isolation

In technology generations up to 0.25 micron, isolation and separation of active areas was achieved by local oxidation of silicon (LOCOS) and its modifications, such as poly-buffered LOCOS (PBLOCOS or LOPOS). The processing of this LOCOS isolation is relatively simple. A pad-oxide and nitride hardmask is deposited. The isolation areas are opened up by reactive ion etching (RIE) using the necessary lithography steps. Oxide is grown in the opened areas by thermal oxidation separating the active areas which are still covered by the nitride hardmask. During this process some oxide also grows underneath the nitride forming what is called a bird's beak. This bird's beak limits the down-scaling capabilities of LOCOS technology (Fig. 4.1). For this reason, new isolation techniques are required for 0.25 μm technologies and below.

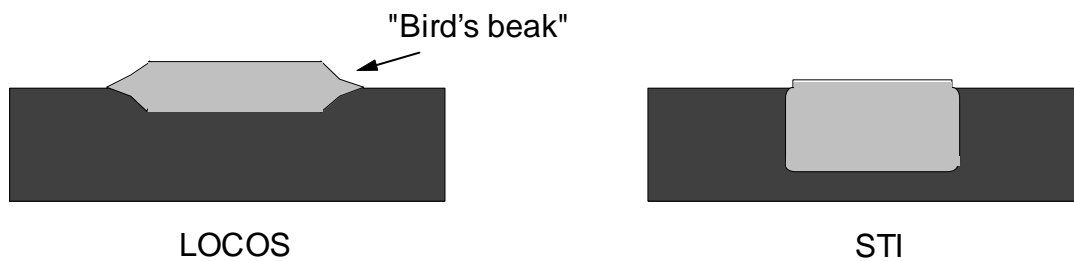


Fig. 4.1: *Comparison of isolation techniques. Local oxidation of silicon (LOCOS) on the left and shallow trench isolation (STI) on the right. During LOCOS formation a bird's beak develops, which limits the scaling capabilities of this technology below 0.25 micron.*

The so called "shallow trench isolation" (STI) is a promising candidate [39]. In this process shallow trenches are etched into the silicon substrate, typically around 400 nm deep. These trenches are then filled with oxide to achieve separation and isolation of neighboring active areas. Several problems are associated with the technological procedure of STI processing. These problems will not be discussed in detail here, because the technology as such was not the motivation for the presented investigations. The problems technologists face are the shape of the trench, corner rounding, etch rates, CMP control, and gate oxide thinning at the active area edges to name just a few. In this thesis it is being investigated how much mechanical stress is induced by the various STI process steps, pinpointing areas of high stress and combinations of process steps that lead to a drastic increase in stress.

The samples investigated in this chapter were from two different STI processes, all processed at the IMEC (Interuniversity Microelectronics Center) in Leuven, Belgium. Besides many small changes, the main difference between both processes is in the filling of the trench. In one process the trench is filled by a thin flowable oxide and a thick TEOS (section 4.1.1) [40], whereas in the other process the trench is filled by a HDP (high density plasma) oxide (section 4.1.2) [41]. The processes will

therefore be referred to as the "*TEOS process*" (4.1.1) and the "*HDP process*" (4.1.2). The *TEOS process* is an older process which was not meant for the fabrication of actual devices. The *HDP process* is based on the *TEOS process* with some changes and improvements. In the following two sections both processes will be described in detail.

4.1.1 The *TEOS Process*

This shallow trench isolation (STI) process consists of the following main process steps [40]: The isolation mask is prepared by deposition of a 20 nm pad-oxide and 200 nm nitride film (Step 1, Fig. 4.3). After photolithographic definition of the active area, the nitride/oxide stack is etched and subsequently the trenches are etched 380 nm deep into the silicon substrate (Step 2, Fig. 4.3). After cleaning a 20 nm thick thermal oxide is grown at 1050°C on the trench bottom and sidewalls (Step 3, Fig. 4.3). This step is also called sidewall re-oxidation. The trenches are then filled in two steps. A flowable oxide (hydrogen silesquioxane spin on dielectric, HSQ) is deposited by spin coating and cured at 850°C in oxygen (Step 4, Fig. 4.3). This provides enough sloping of the trench profiles to allow a void-free bulk fill of the trenches with 550 nm of LPCVD TEOS (Step 5, Fig. 4.3). The densification of this oxide was performed either in dry ambient (O_2) at 1050°C or in wet ambient (steam, H_2/O_2) at 850°C.

Due to the different etch rates of the two different oxides, HSQ and TEOS, it was found to be difficult to control the CMP (chemical mechanical polishing) process². This process is used after the filling of the trenches for planarization. The filling of the trenches was different for different trench widths. In very narrow trenches (0.3 μm), the

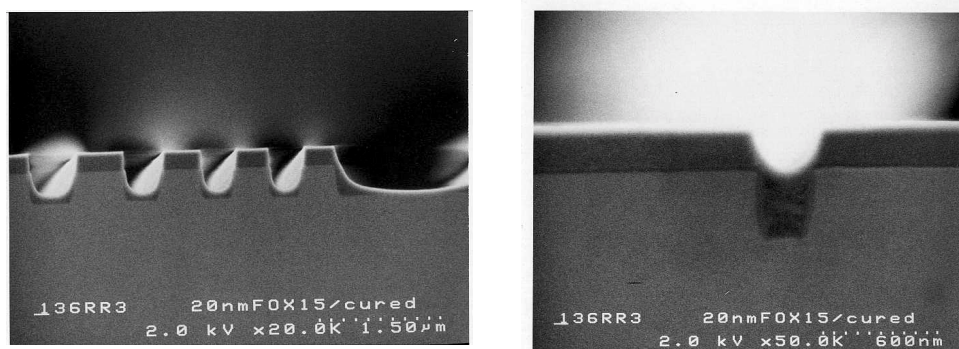


Fig. 4.2: SEM pictures¹ of shallow trench structures after the deposition of the HSQ oxide (step 4, Fig. 4.3). The picture on the left shows a wide trench and a periodic array of 0.5 μm wide trenches. In narrow isolated trenches (0.3 μm), the HSQ fills the trench completely (picture on the right).

¹ SEM pictures courtesy of R. Rooyackers, IMEC Leuven, Belgium

² Personal communication with R. Rooyacker from IMEC, Belgium

flowable oxide filled the trenches completely (Fig. 4.2), so that during CMP the etch rates were different compared to wide trenches, which are mainly filled by TEOS. The result of this was the inability to stop the CMP process in the nitride layer for all trench dimensions. This problem was eliminated by a different trench fill in the *HDP process*, which will be explained in the next section.

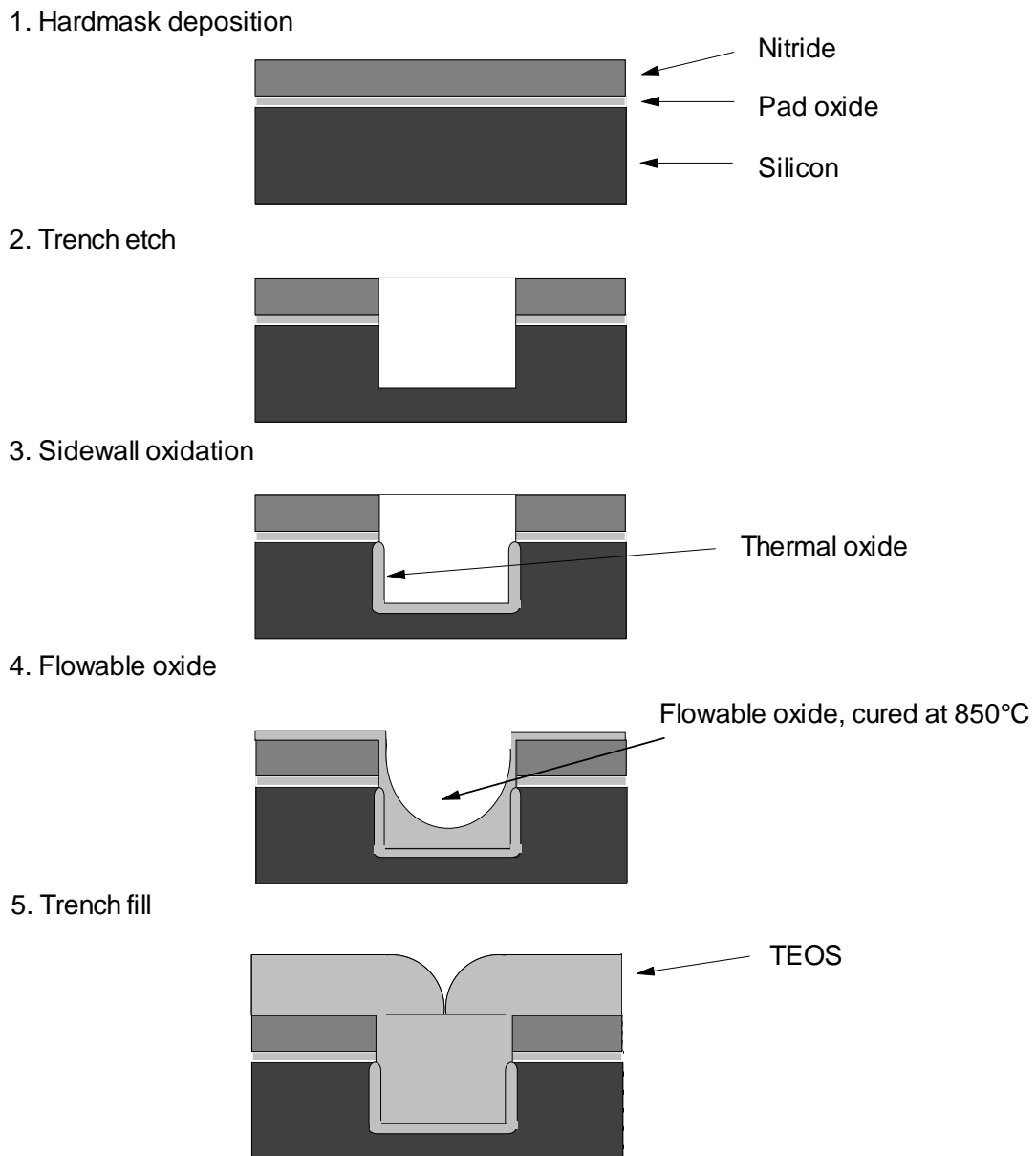


Fig. 4.3 Main process steps of the "TEOS process".

4.1.2 The HDP Process

This process is basically the same as the *TEOS process* up to the filling of the trenches, with some minor parameter changes [41]. The pad-oxide is only 15 nm thick, the nitride only 150 nm, and the sidewall oxide thickness is either 20 nm or 40 nm (Steps 1,2 and 3 of Fig. 4.3 and Fig. 4.4). The trench fill is completely different. In the *HDP process* the flowable oxide deposition has been eliminated. The trenches are filled

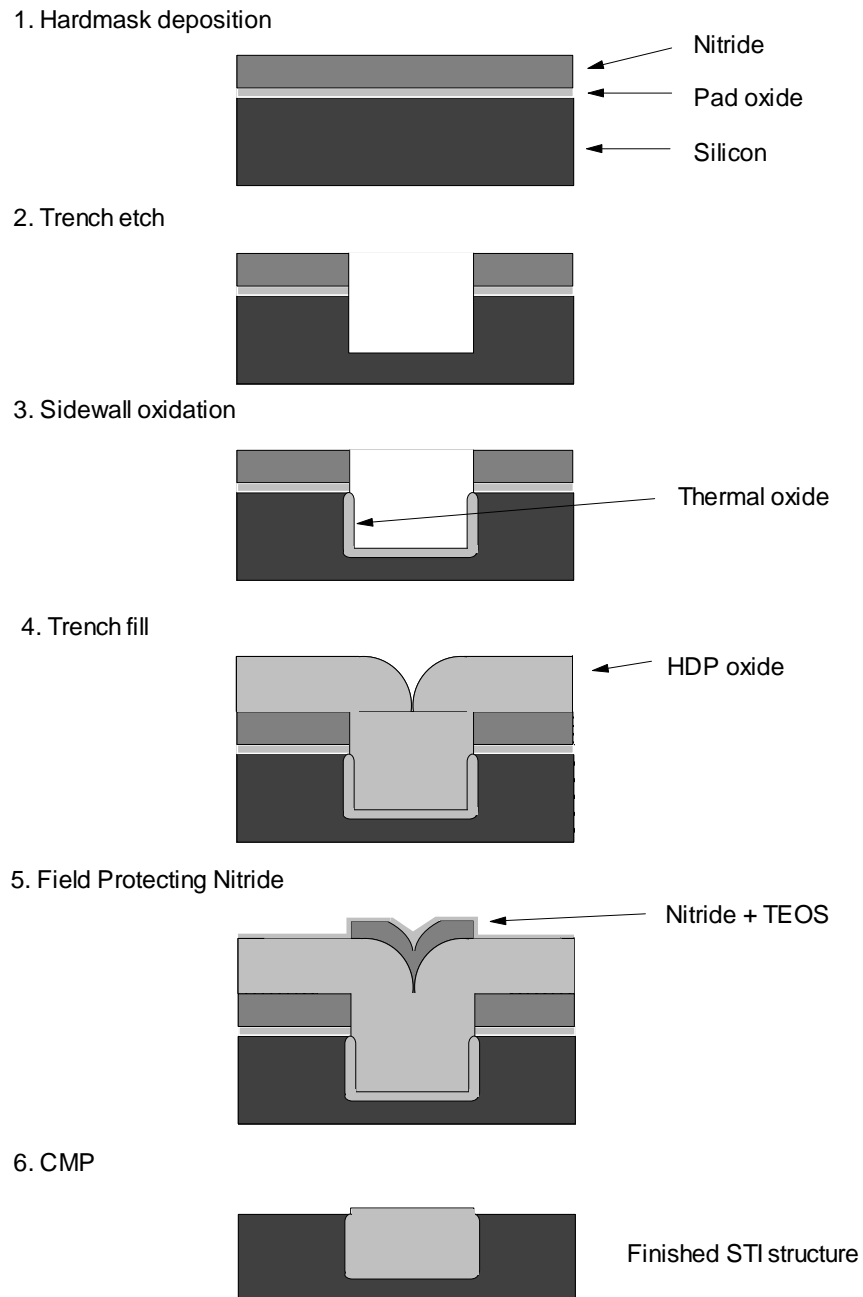


Fig. 4.4: Main process steps of the "HDP process".

completely with 500 nm HDP oxide (step 4, Fig. 4.4), assuring equal etch rates for all trench widths. Prior to CMP a 100 nm field protecting nitride is deposited on top of the HDP oxide, which is opened above the active areas using an additional lithography step. After the removal of the resist a 50 nm thick TEOS is deposited (step 5, Fig. 4.4). CMP follows to planarize the structure. The densification of the trench fill material is then performed in dry ambient (N_2 , $1050^\circ C$) after the removal of the residual nitride mask. Some of the investigated samples are processed without this densification step. Afterwards a 20 nm pre-gate (PG) oxide is grown prior to the well implant. If the trench fill densification step has been performed, the pad-oxide is removed by wet etching prior to PG formation. This PG oxide is grown either at $900^\circ C$ in wet (H_2/O_2) ambient or at $1075^\circ C$ in dry (O_2) ambient. After n-well implantation, the wells are annealed at $850^\circ C$ in O_2 . After removal of the implant oxide (PG oxide) the gate oxide is grown (3.5 nm at $650^\circ C$ in H_2/O_2 ambient).

The influence of the different process steps on mechanical stress in the underlying silicon substrate will now be discussed in detail in the following sections.

4.2 Mechanical Stress caused by STI

During and after shallow trench isolation processing the silicon next to the STI regions is strained. This strain is caused by stress induced from the various nitride and oxide layers through volume expansion (oxidation), intrinsic stress (nitride), or differences in thermal expansion coefficients.

In the following sections the stress caused by the different processing steps will be shown in detail: i) the nitride hardmask and sidewall oxidation, ii) the filling and densification of the trench oxide in the *TEOS process*, iii) the filling of the trench in the *HDP process*, and iv) the influence of the pre-gate oxidation ambient on stress in the *HDP process*.

The measurements of stress using blue and UV light for excitation will be compared to underline the advantages of UV over visible light. Stress measurements in structures smaller than the laser spot will also be shown. The lineshape and width of the silicon phonon under stress will also be discussed, because it gives some information about the amount of averaging over the finite laser spot size. This also points to further investigations which need to be performed to draw more information from the Raman measurements. In summary, it will be shown how mechanical stress evolves through the complete isolation process and how certain combinations of process parameters can lead to a drastic increase in stress, causing defects and the degradation of electrical device characteristics.

The device structures investigated always consist of long stripes (2 mm) of active areas separated by STI regions. The widths of these stripes will always be given in the text. They range typically from 3 μm to 0.3 μm . Stress measurements were

always performed crossing the stripes in the center, so that the influence of stress components along the length of the edges are zero ($\sigma_y = 0$). Measuring the stress at corners or in small square structures will certainly increase the stress as shown in [13], since here the other stress component (σ_y) is of comparable magnitude as σ_x (compare chapter 3 and [13]).

4.2.1 Stress from Nitride and Sidewall Oxide (TEOS & HDP Process)

A CVD nitride (chemical vapor deposition Si_3N_4) film has large intrinsic tensile stress [42]. After deposition on silicon and patterning, the film stress can relax at the edges by causing a compressive stress in the underlying silicon substrate [28]. The magnitude of this compressive stress is proportional to the thickness of the nitride film. Fig. 4.5 shows a comparison of stress measured in a $3\ \mu\text{m}$ wide active area stripe covered by 15/150 nm pad-oxide/nitride and 20/200 nm pad-oxide/nitride films. Fig. 4.5 (a) shows the comparison obtained using UV light (364 nm) and Fig. 4.5 (b) using blue light (458 nm) to excite the Raman scattering. The sidewalls are covered in each case with 20 nm of sidewall oxide. The influence of the sidewall oxide on stress will be discussed later in this section. UV light and blue light both show the increase of compressive stress in the center of the stripe by almost 60%, indicated by the higher silicon phonon shift. Only UV light shows in addition the high corner stress at the edges of the active area stripe. This behavior will also be discussed in more detail later on. In order to minimize the stress induced in the silicon, a thin pad-oxide is deposited prior to the nitride. Above approximately 1000°C this oxide becomes viscous and is supposed to relax some of the stress from the nitride film. As can be seen in Fig. 4.5 the influence of the pad-oxide on the total amount of stress in silicon remains unclear.

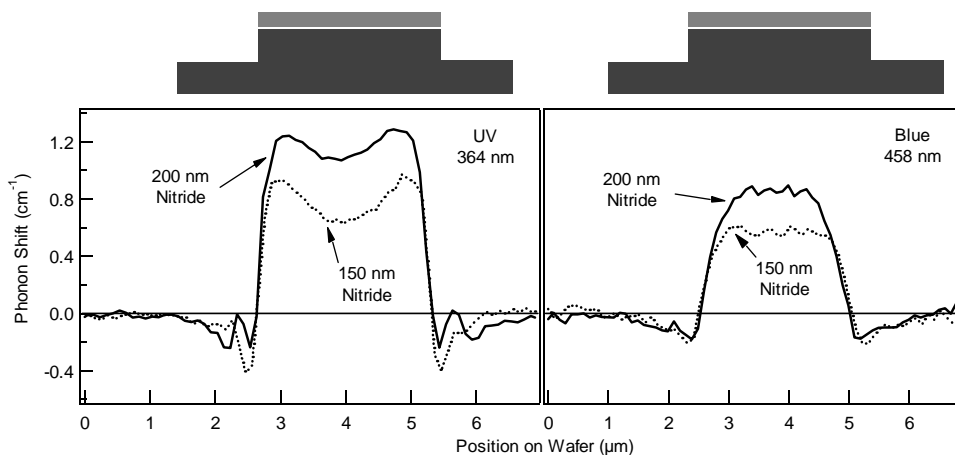


Fig. 4.5: Comparison of stress in a $3\ \mu\text{m}$ wide active area stripe covered by 150 nm and 200 nm nitride. The figure on the left shows the measurement using UV light and the figure on the right using blue light for excitation.

Although the 200 nm nitride layer has a thicker pad-oxide underneath (20 nm instead of 15 nm), the compressive stress in the silicon is 60% higher compared to the 15/150 nm pad-oxide/nitride layer. Further measurements would be required to determine the exact influence of the pad-oxide on the stress relaxation mechanism.

On either side of the active area stripe, tensile stress is indicated by the downshift of the silicon phonon in Fig. 4.5. This tensile stress is caused by the sidewall oxide. Fig. 4.6 shows the mechanical stress measured across a 3 μm wide active area stripe after process steps two (Fig. 4.6 (a)) and three (Fig. 4.6 (b)) of the *HDP process*. The measurements were performed using UV (364 nm) light to excite the Raman scattering. A cross-sectional schematic drawing of the investigated sample structure is shown above the figure. The active area stripe is covered by a 15 nm pad-oxide and 150 nm nitride film. Right after trench etch (Fig. 4.6 (a)) the Si phonon shift is zero in the

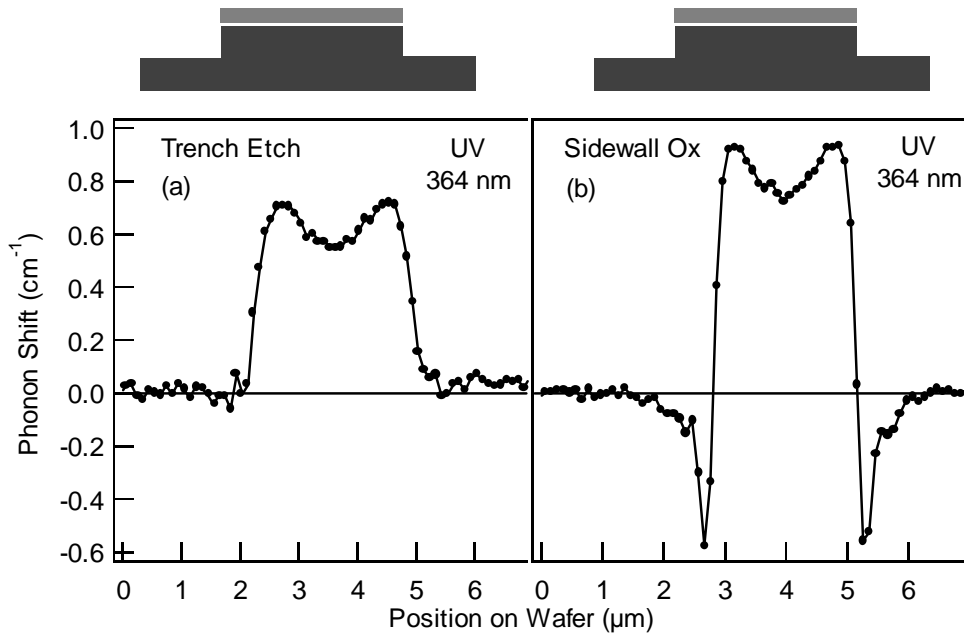


Fig. 4.6: Comparison of mechanical stress in a 3 μm wide active area stripe right after trench etch (a) and after sidewall oxidation (b). A schematic cross section of the sample structure is shown at the top of the figure. The silicon active area mesa is covered by 15 nm pad oxide and 150 nm nitride. The sidewall oxide is 40 nm thick. Each point in the figure corresponds to one Raman measurement. The lines are just connecting the points.

trenches left and right of the active area stripe indicating unstrained silicon. As the laser spot probes the top of the active area stripe the silicon phonon shifts to higher energies. This upshift indicates compressive stress under the nitride hardmask, as expected. At the edges of the stripe the phonon shift reaches a maximum value of 0.75 cm^{-1} and decreases towards the center of the stripe where it reaches a value of 0.55 cm^{-1} . This decrease of stress towards the center of the 3 μm wide stripe is only seen using UV light. Using blue light (Fig. 4.5 and Fig. 4.7) shows the maximum of stress in the center

of the stripe. A decrease of stress towards the center of the stripe could previously only be observed for 5 μm or wider stripes. The stress at the center of the stripe is almost exactly uniaxial (σ_x), so that the measured phonon shift corresponds to a compressive stress of -275 MPa. The stress value at the edge cannot be given as easily, since here the stress is definitely biaxial.

After 40 nm sidewall oxidation (Fig. 4.6 (b)) the stress pattern shows some changes. Left and right of the active area stripe tensile stress is indicated by the downshift of the silicon phonon. The compressive stress on top of the stripe under the nitride also increased. A direct comparison of the two stress patterns shows, that all of the changes are caused by the sidewall oxide. Thermal oxide has about 2.3 times the volume of silicon. During growth it expands and induces tensile stress in the underlying silicon. This stress is largest in the trench bottom corners where the phonon shift reaches a maximum value of -0.6 cm^{-1} . This shift would correspond to a tensile stress of 300 MPa, if it were assumed to be entirely uniaxial.

Besides inducing large tensile stress in the trench corner, the sidewall oxide also increases the compressive stress under the nitride. The phonon shift at the edge of the active area is now 0.9 cm^{-1} and in the center of the stripe 0.7 cm^{-1} . So in the center the stress has increased to -350 MPa. The magnitude of this increase also depends on the thickness of the sidewall oxide as shown in Fig. 4.7.

Fig. 4.7 shows the comparison of stress patterns obtained from a 3 μm wide active area stripe after trench etch, 20 nm sidewall oxidation and 40 nm sidewall oxidation using UV (a) and blue (b) light. The compressive stress in the center under the nitride increases with increasing oxide thickness as well as the tensile stress in the trench

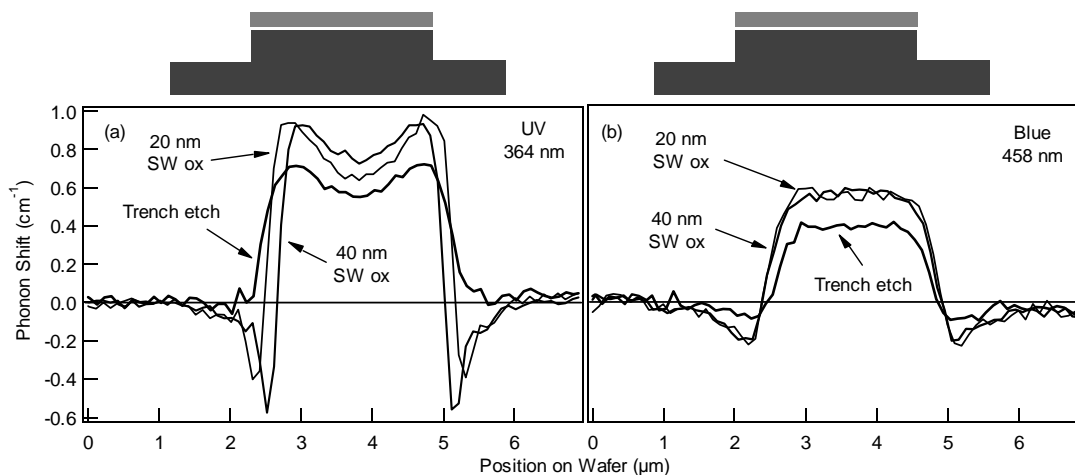


Fig. 4.7: Comparison of stress measurements obtained with UV (364 nm) light (a) and blue (458 nm) light (b) in the same 3 μm wide active area stripe. Both figures (a) and (b) show the stress right after trench etch and with 20 nm and 40 nm of sidewall oxide (SW ox). A schematic drawing of the sample structure is shown at the top of the figure.

bottom corners. All of these changes between 20 and 40 nm sidewall oxidation are only seen using UV light (Fig. 4.7 a) and not with blue light (Fig. 4.7 b).

This demonstrates the advantage of UV over blue light. Since UV light penetrates only 12 nm into silicon as compared to over 300 nm for previously used blue light, only the stress close to the silicon surface is probed, showing the high corner stress. Since stress decreases quickly into the substrate, the changes in near-surface stress are averaged away by the large penetration of blue light. The advantage of UV over blue light becomes even more obvious looking at smaller structures.

Fig. 4.8 and Fig. 4.9 show the stress measured in active area stripes of decreasing width, separated by 2 μm wide trenches. A schematic cross-sectional drawing of the investigated sample structure is shown at the top of each figure. The stripe widths from left to right are 3, 2, 1, 0.9, 0.8, 0.7, 0.6, 0.5, 0.45, 0.4, 0.35, and 0.3 μm . The top trace in each figure is obtained right after trench etch, the middle trace after 20 nm sidewall oxidation, and the bottom trace after 40 nm sidewall oxidation. Fig. 4.8 shows the measurements using UV light and Fig. 4.9 using blue light. Both figures will now be discussed in detail.

The top trace of Fig. 4.8 shows an increase of the compressive stress in the 2, 1, and 0.9 μm wide stripes compared to the 3 μm wide stripe. At the same time the high corner stress is no longer resolved. From the 0.9 μm wide stripe on, the stress appears to decrease going to even smaller stripe widths. Although the laser spot on the sample is around 0.7 μm wide, the stress from the 0.3 μm wide active area stripe is clearly seen with UV light (top trace Fig. 4.8). This is not the case for blue light (top trace Fig. 4.9), where the stress increases slightly from the 3 μm to the 2 μm wide stripe, decreases for the narrower stripes, smears out and disappears almost completely for the smallest stripes.

The observed increase and decrease of stress are the result of a complex interplay between the decreasing film stress, the increasing overlap of the edge induced corner stress from both sides of the stripe, and averaging over the finite laser spot. As described in chapter 3, the film stress decreases with decreasing stripe width. Speaking in the picture of the "edge force model" (chapter 3), the stress in the silicon substrate is determined by the film stress, acting at the edge of the film, times a distribution function, describing the distribution of stress in the silicon substrate. This distribution function is in principle a $1/r$ function with r being the distance from the edge. As the stripes become narrower, the film stress decreases. At the same time, the edges of the stripes come closer together, so that the high corner stress starts to overlap in the center of the stripe. So, although the overall stress motor (the film stress) becomes weaker, the stress still increases, because the corner stress overlap over-compensates the decrease in film stress.

This explains the observed increase in stress going from the 3 μm to the 2, 1, and 0.9 μm stripe in the top trace of Fig. 4.8. The observed decrease for even smaller stripes is a result of averaging over the laser spot. The stress in the trenches between the active areas is zero. Since the laser spot has a Gaussian intensity distribution and a width of

around $0.7 \mu\text{m}$ at $1/e^2$ for UV light and around $0.9 \mu\text{m}$ for blue light, more and more of the zero stress from the trenches is averaged into the silicon phonon position. As the structures become smaller than the laser spot, some zero trench-stress is averaged into the phonon position even in the center of the stripe leading to the observed decrease in stress.

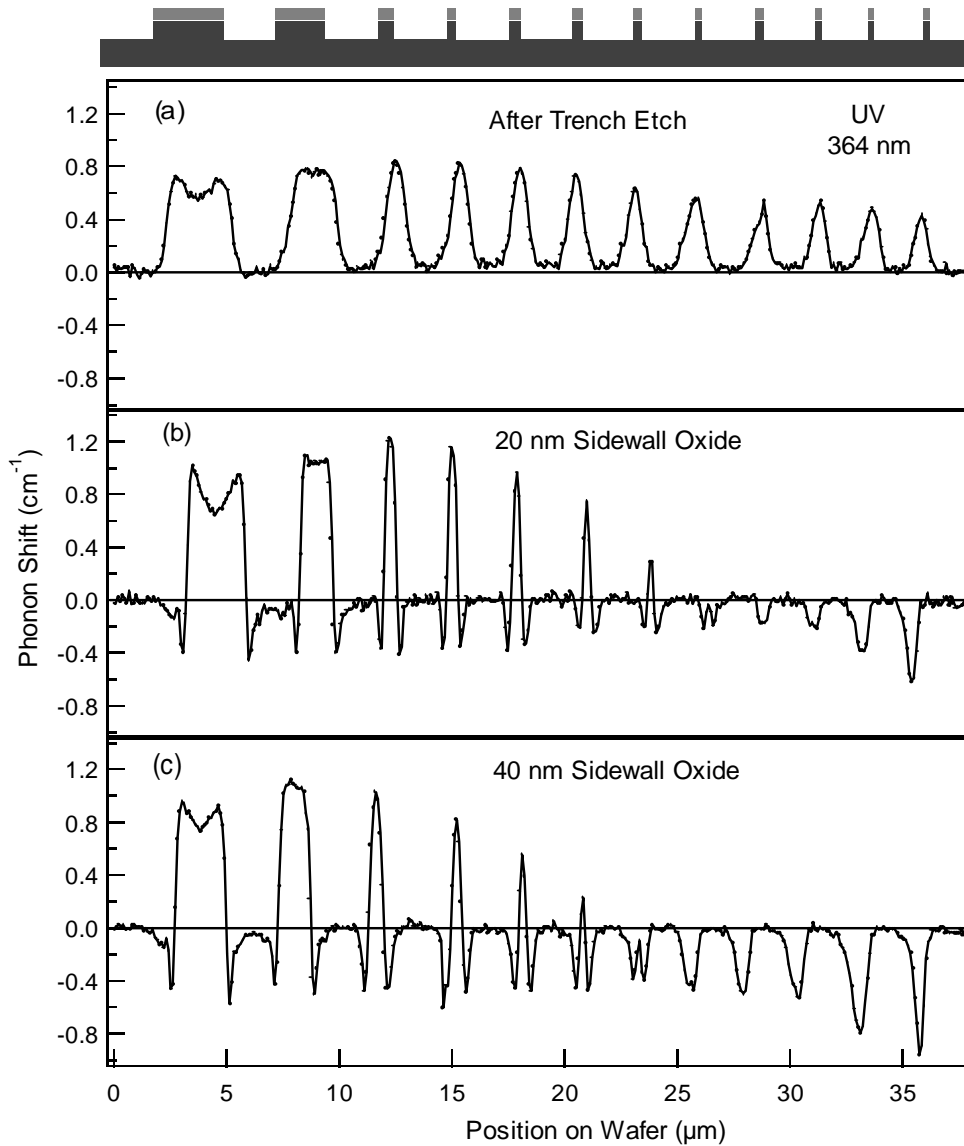


Fig. 4.8: Comparison of stress patterns obtained with UV light (364 nm) in active area stripes of changing width separated by $2 \mu\text{m}$ wide trenches. A cross-section of the sample structure is shown at the top. The stripe widths from left to right are: 3, 2, 1, 0.9, 0.8, 0.7, 0.6, 0.5, 0.45, 0.4, 0.35, 0.3 μm . The top trace shows the stress right after trench etch. The middle and bottom traces show the stress after 20 nm and 40 nm sidewall oxidation. All three wafers are from the HDP process (15/150 nm pad-oxide/nitride).

The interplay between film stress, corner stress and averaging over the laser spot becomes even more important looking at the stress measurements after sidewall oxidation.

The middle and bottom traces of Fig. 4.8 and Fig. 4.9 show the stress after 20 and 40 nm sidewall oxidation, respectively. As described earlier, the tensile stress is caused by the sidewall oxide in the trench bottom corners. As the stripes become narrower the

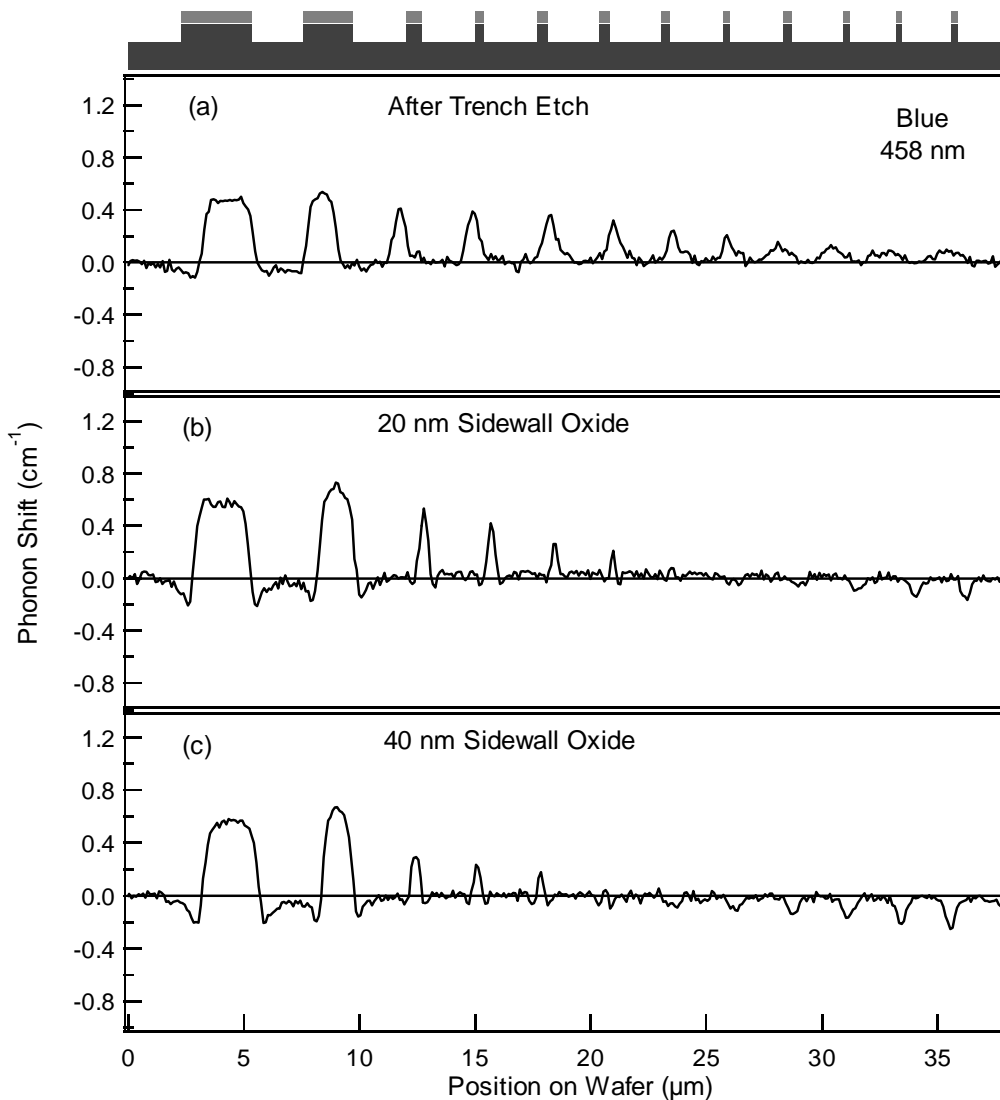


Fig. 4.9: Comparison of stress patterns obtained with blue light (458 nm) in active area stripes of changing width separated by 2 μm wide trenches. A cross-section of the sample structure is shown at the top. The stripe widths from left to right are: 3, 2, 1, 0.9, 0.8, 0.7, 0.6, 0.5, 0.45, 0.4, 0.35, 0.3 μm . The top trace shows the stress right after trench etch. The middle and bottom traces show the stress after 20 nm and 40 nm sidewall oxidation. All three wafers are from the HDP process (15/150 nm pad-oxide/nitride).

compressive stress under the nitride increases initially and starts to decrease in smaller stripes. From a certain stripe width on the measured stress is completely tensile. This phenomenon can only be explained by averaging over the laser spot.

The phonon shift indicated in the previous figures is always the center position of the silicon peak in the Raman spectra. This center position corresponds approximately to the weighed average of the stress under the laser spot. If the laser spot covers the same amount of tensilely and compressively strained silicon, the center position of the measured peak will be at the position of unstrained silicon (phonon shift zero). The information about tensile and compressive stress is still enclosed in the phonon peak in the Raman spectrum, but can only be extracted with the help of modeling. An indication about the amount of averaging is given by the width and asymmetry of the measured silicon phonon peak (compare chapter 2).

The stress patterns after sidewall oxidation consist of areas of tensile and compressive stress. As the laser spot becomes bigger than the investigated sample structure, averaging over the laser spot is the dominant factor that determines the observed phonon shift. If the sample structure is small enough so that the areas of tensile stress at either side of the stripe are bigger than the area of compressive stress in the center of the stripe, the measured phonon shift will eventually be tensile. This is seen in the middle and bottom traces of Fig. 4.8 and Fig. 4.9 for the stripes below 0.5 μm . The UV measurements again resolve the fine details of the different stress areas much better than the measurements using blue light, even in the smallest structures, because in addition to the lateral averaging blue light also averages over the 300 nm depth. The UV measurements, for example, still show an indication of the compressive stress in the center of the 0.5 and 0.6 μm stripe after 20 and 40 nm sidewall oxidation, respectively (Fig. 4.8). The measurements with blue light, on the other hand, hardly show the 0.6, 0.5 and 0.45 μm structures after 20 nm sidewall oxidation and the 0.7/0.6 μm stripe after 40 nm sidewall oxidation at all (Fig. 4.9).

4.2.2 Stress from Trench Oxide (*TEOS Process*)

In the *TEOS process* the filling of the shallow trenches is performed in two steps (see 4.1.1). First, a flowable oxide is deposited and cured to achieve good trench sloping. Secondly, the trenches are filled with LPCVD TEOS. This oxide is then densified in wet ambient at 850°C or in dry ambient at 1050°C. The mechanical stress induced in the underlying silicon by these three process steps will be discussed in this section.

Fig. 4.10 shows a comparison of the stress measured with UV light (364 nm) across a 3 μm wide active area stripe after process steps 3, 4 and 5 of the *TEOS process* (for details see 4.1.1). Fig. 4.10 (a) shows the stress after 20 nm sidewall oxidation (process step 3), (b) after the deposition and curing of the flowable oxide (process step 4), (c) after deposition of 550 nm TEOS and densification in dry ambient at 1050°C

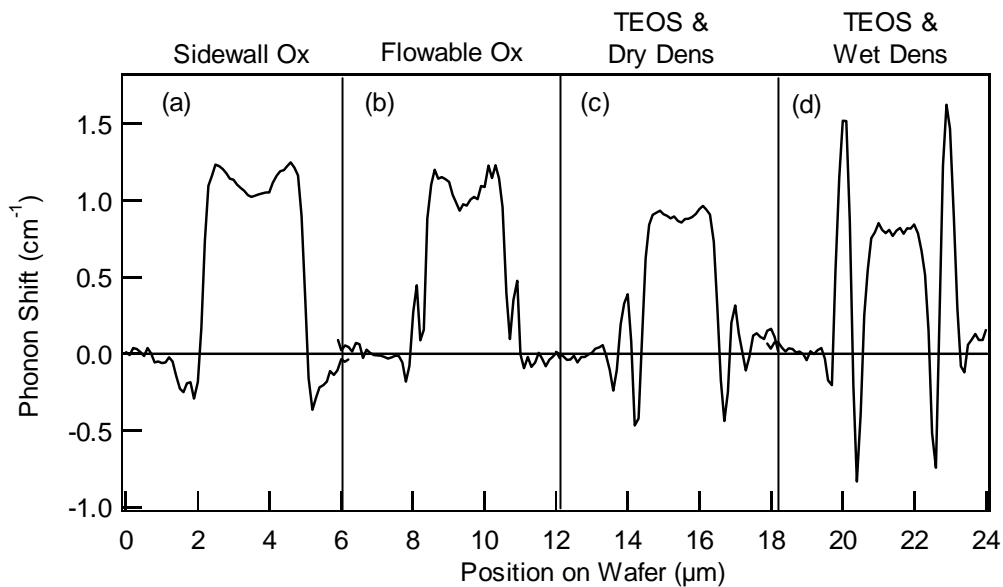


Fig. 4.10: Comparison of stress measured in 3 μm wide active areas after 20 nm sidewall oxidation (a), after flowable oxide deposition and curing (b), after 550 nm TEOS deposition and densification in dry ambient (c), and after 550 nm TEOS deposition and densification in wet ambient (d). All measurements were obtained using UV light (364 nm) for excitation.

(process step 5), and (d) after deposition of 550 nm TEOS and densification in wet ambient at 850°C (process step 5). All active area stripes (a)-(d) are still covered by the 20/200 nm pad-oxide/nitride layers.

The stress pattern of Fig. 4.10 (a) is basically the same as the one in Fig. 4.5 (a). The compressive stress in the active area stripe is caused by the nitride, and the tensile stress on either side of the stripe is caused by the sidewall oxide (compare 4.2.1). After deposition of the flowable oxide and curing at 850°C an additional stress peak is observed in Fig. 4.10 (b) near the edges of the active area stripe. This additional peak is even stronger after TEOS deposition and dry densification (Fig. 4.10 (c)) and becomes dominant after TEOS deposition and wet densification (Fig. 4.10 (d)). The origin of this additional peak will now be discussed.

Fig. 4.11 shows the four stress patterns of Fig. 4.10 overlaid. It can be seen, that the additional stress peak is not located in the trench but at the top edge of the active area stripe. Going from left to right the additional peak consists of a compressive stress followed by an area of tensile stress. This stress pattern on its own is the characteristic pattern of a bird's beak. SEM investigations¹ in samples after wet and dry densification proved, that this assumption is correct (Fig. 4.12). The additional peak is caused by a bird's beak which starts to form already after flowable oxide deposition and curing (in dry ambient). After TEOS deposition and densification in dry ambient the bird's beak

¹ Performed by C. Stuer, University of Antwerp, Belgium

grows only slightly, whereas after TEOS deposition and wet densification the bird's beak grows quite substantially. This is shown in the SEM pictures in Fig. 4.12.

In addition to the formation of a bird's beak, the sidewall oxide thickness also increases during wet densification. The combination of this increase together with the formation of the bird's beak led to a re-entering shape of the top trench corner. During dry densification no additional sidewall oxide growth was seen in the SEM pictures. The bird's beak is also much smaller. The observation of the large stress caused by the growth of a bird's beak during trench fill and wet densification became possible only through the use of UV light [37, 40]. Performing the same measurements as shown in Fig. 4.10

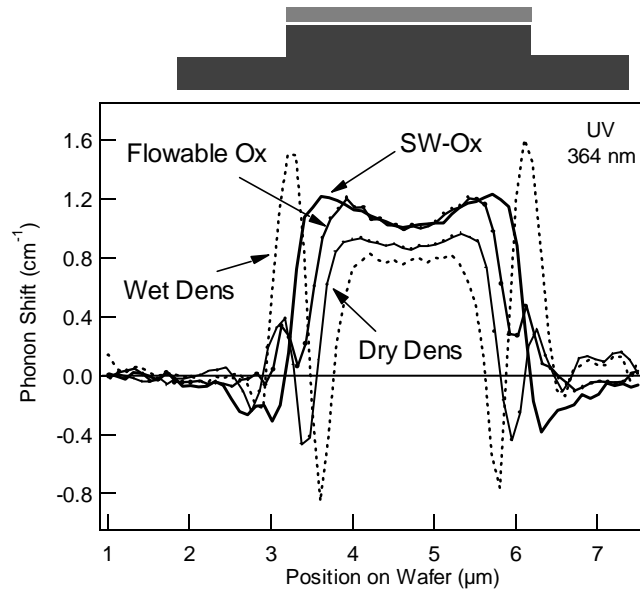


Fig. 4.11: Comparison of the same four stress measurements as in Fig. 4.10. Here, the stress patterns are overlaid to show the origin of the additional compressive and tensile stress peak at the edges of the active area stripe. A schematic cross-section of the $3 \mu\text{m}$ wide sample structure is shown at the top of the figure.

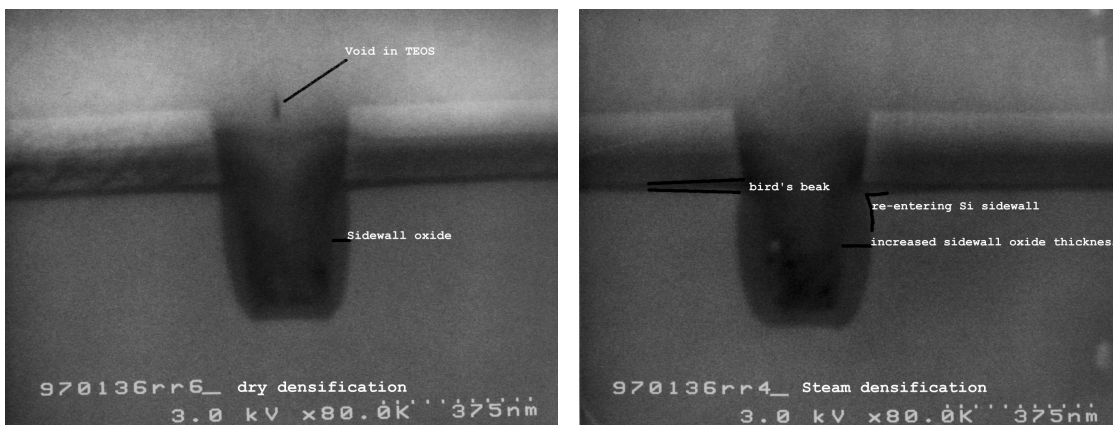


Fig. 4.12: SEM pictures of 300 nm wide shallow trenches processed by the TEOS process after TEOS deposition and densification in dry ambient (left) and wet ambient (right). The picture after wet densification (right) shows an increase in sidewall oxide thickness, a re-entering shape of the top trench corner and a large bird's beak extending under the nitride hardmask. The bird's beak is smaller after dry densification (left picture).

and Fig. 4.11 using blue light does not reveal the high additional stress at the edge of the active area stripe (Fig. 4.13). The measurement using blue light also shows a small additional peak after wet densification, but this peak is tensile and of approximately the same size as the tensile peak from the sidewall oxide. The large compressive peak from the bird's beak is missed altogether.

The reason for this discrepancy between the blue and UV measurement is once more averaging. The stress from the bird's beak is averaged away almost completely by the large penetration depth of the blue light, but is seen by the surface sensitivity of UV light. This underlines the superiority of stress measurements using UV instead of blue light.

Further proof for the bird's beak assumption is given by finite element (FE) simulations¹. Fig. 4.14 shows a comparison of calculated and measured phonon shifts in a 3 μm wide active area after sidewall oxidation and after TEOS deposition and subsequent wet densification. The FE calculations were performed using a non-linear viscoelastic oxidation model [43, 44] implemented in the 2D process simulator IMPACT-4 [45]. The phonon shifts were calculated from the FE simulations by averaging the stress components according to the theory presented in chapter 2 and 3 of this thesis. The calculated stress was averaged laterally using a Gaussian weight function corresponding to the intensity distribution of the laser spot. The averaging over depth was performed using the exponential weight function given in chapter 2. The agreement between simulated phonon shift and the actual measurements using UV light is very good (Fig. 4.14, bottom figure).

The two graphs at the top of Fig. 4.14 show the σ_x component of mechanical stress after sidewall oxidation (top left, Fig. 4.14) and after TEOS deposition and wet densification (top right, Fig. 4.14). The FE simulations show the tensile stress in the bottom corner of the trench after sidewall oxidation. The model does not show the

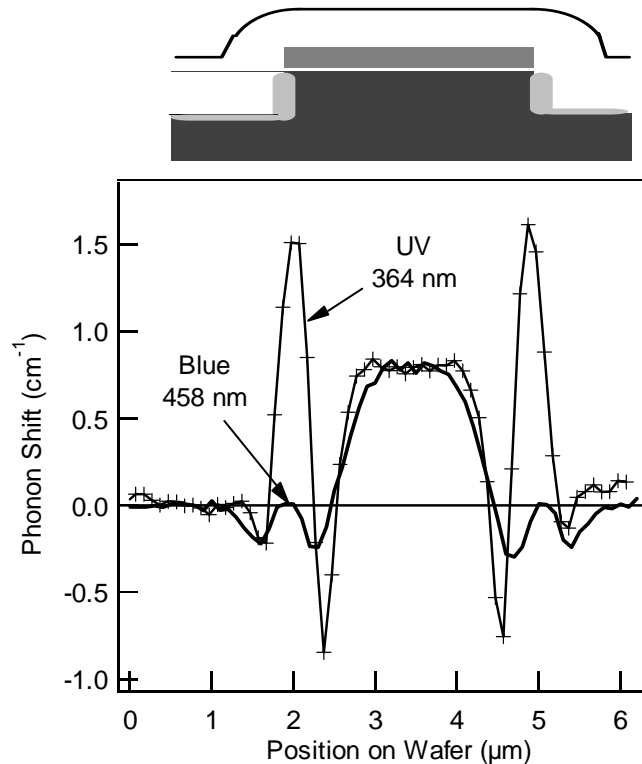


Fig. 4.13: Comparison of stress measurements in the same 3 μm wide active area obtained with UV (364 nm) and blue (458 nm) light. The sample structure is shown schematically at the top.

¹ Performed by T. Hoffmann, IEMN-ISEN, Villeneuve d'Ascq Cédex, France

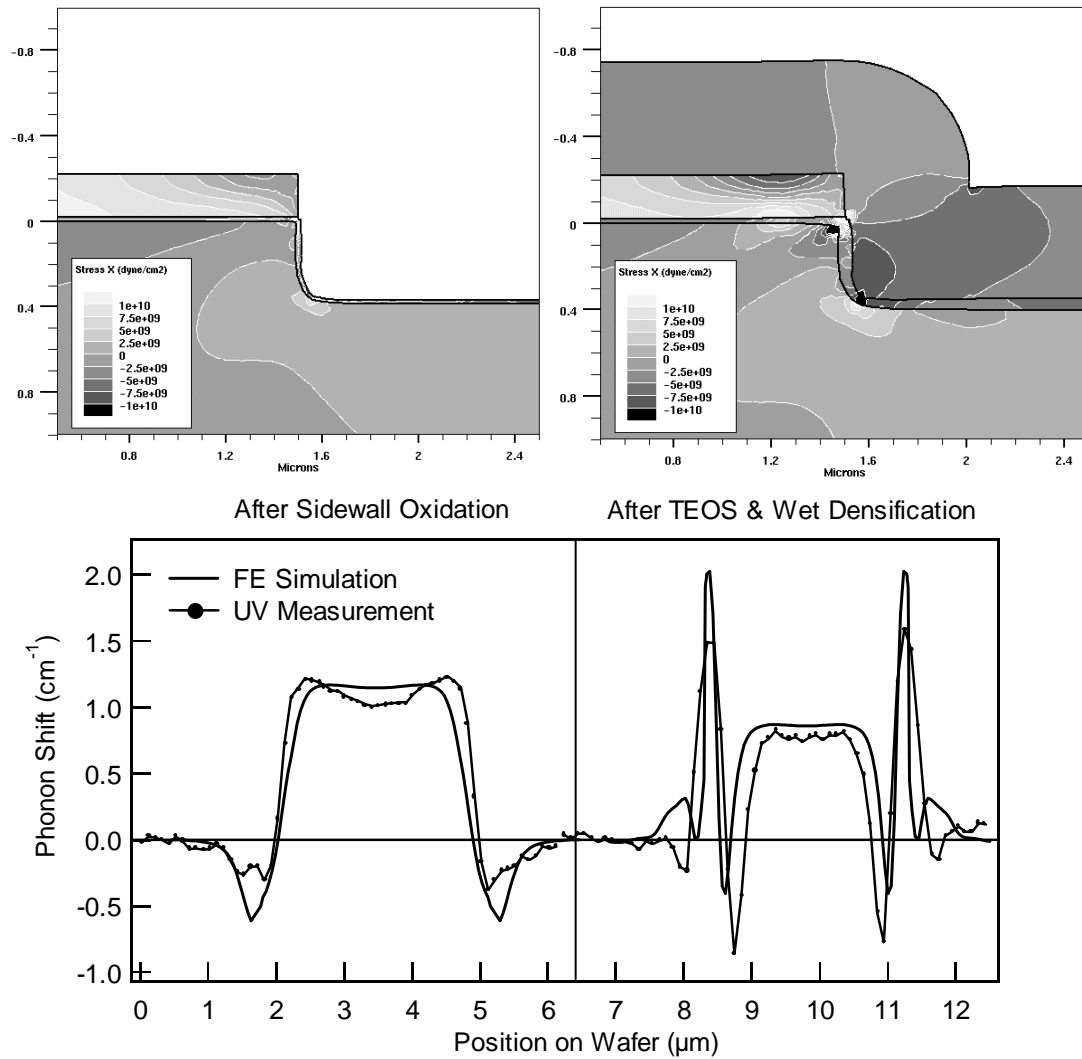


Fig. 4.14: *Finite Element (FE) simulation of mechanical stress (top two figures) and comparison of calculated (solid lines, bottom figure) and measured silicon phonon shift (line & dots, bottom figure) in a 3 μm wide active area after sidewall oxidation and after TEOS deposition and wet densification.*

decrease of stress towards the center of the stripe very well. After wet densification the FE model reproduces the high compressive and tensile stress from the bird's beak very well. The 2D stress map at the top of Fig. 4.14 also shows the re-entering shape of the active area stripe's top corner after wet densification. The good agreement between simulation and experiment validates the theoretical model quantitatively and allows the numerical algorithm to be extended to 3D [46].

The comparison of FE simulations and UV Raman measurements is another example for the improvement gained by the use of UV over blue light. Since the high stress from the bird's beak is hardly visible with blue light, the exact calibration of the FE simulation would be much more difficult if not impossible.

4.2.3 Stress from Trench Oxide (*HDP Process*)

In the *HDP process* the trenches are filled after sidewall oxidation in one step, by deposition of 450 nm HDP oxide. This oxide is not densified until after CMP and removal of the residual nitride mask. To achieve good planarization a field protecting nitride is deposited prior to CMP using an additional lithography step (see 4.1.2 for details).

This section shows, that the deposition of the HDP and field protecting nitride have almost no influence on the stress in the silicon substrate (Fig. 4.15 and Fig. 4.16). After CMP a drastic change occurs, which can not be explained so far. The tensile stress in the trench bottom corners disappears almost completely after CMP (Fig. 4.16).

Fig. 4.15 shows the mechanical stress after sidewall oxidation (same as Fig. 4.8 bottom trace) and after the filling of the trenches with HDP oxide. This oxide is not densified, yet, and the stress in the underlying silicon is not changed very much. The compressive stress under the nitride hardmask on top of the active area stripes has

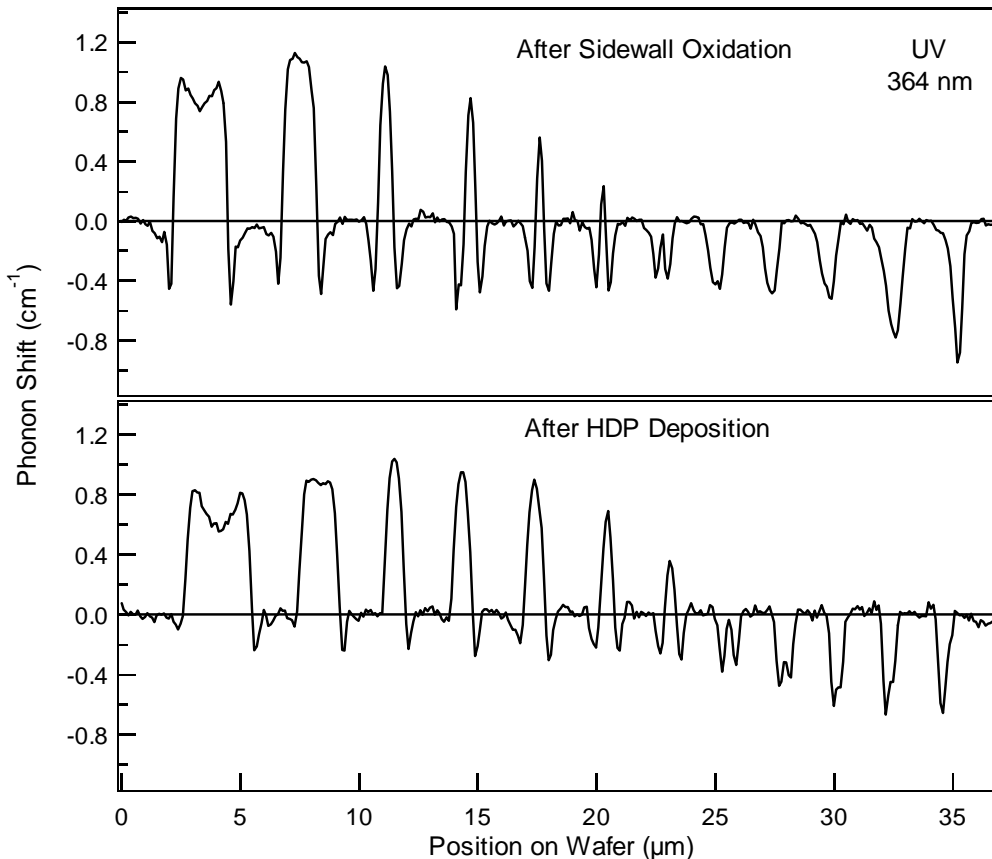


Fig. 4.15: Comparison of stress measured with UV light (364 nm) after 40 nm sidewall oxidation (top trace) and after trench fill with 450 nm HDP oxide (bottom trace). The sample structure is the same as described in section 4.2.1 and consists of active area stripes ranging from 3 μm to 0.3 μm wide (from left to right) separated by 2 μm wide shallow trenches.

decreased slightly. The tensile stress in the trench bottom corners appears to have decreased also. This is seen around the 3 μm wide active area stripe and also in the small active area stripes.

After the formation of the field protecting nitride, which consists of a 100 nm thick nitride layer on top of the HDP oxide opened above the active areas, and an additional 50 nm TEOS layer, the stress hasn't changed notably from after HDP deposition. This is seen by comparing the bottom trace of Fig. 4.15 with the top trace of Fig. 4.16.

At this point, it is remarkable to note, that the stress measurements still work very well. On top of the active area stripes the UV light has to pass through a 15 nm pad-oxide, 150 nm nitride, 450 nm HDP oxide, and 50 nm TEOS stack, before it reaches the silicon surface. All of these materials are transparent in the UV, but the light is still influenced by the different indexes of refraction and density variations within the oxide layers. Apparently these changes are small enough to allow precise stress measurements in the underlying silicon substrate.

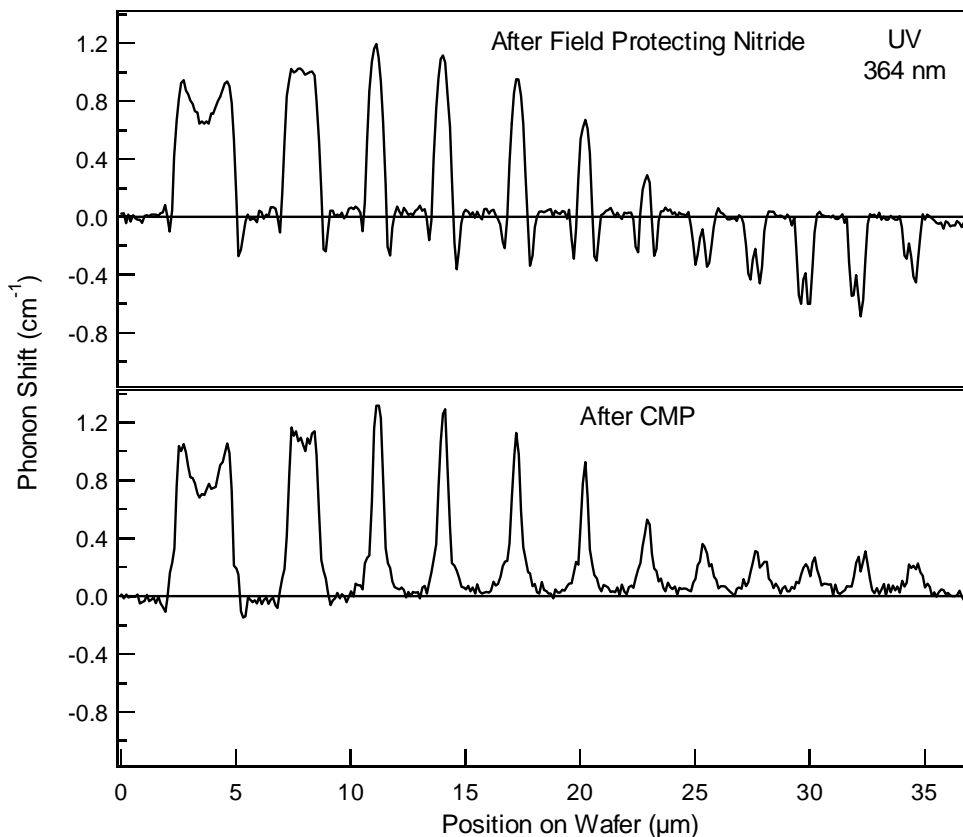


Fig. 4.16: Comparison of stress measured with UV light (364 nm) after deposition and structuring of the field protecting nitride (top trace) and after CMP (bottom trace). The sample structure is the same as described in section 4.2.1. It consists of active area stripes ranging from 3 μm to 0.3 μm wide (from left to right) separated by 2 μm wide shallow trenches.

After planarization of the wafer using CMP the stress has changed remarkably. This is seen in Fig. 4.16. The tensile stress in the trench bottom corners is almost completely gone. The compressive stress in the active area stripes is caused by the residual nitride mask, which has not been removed, yet. A comparison of the compressive stress after CMP (bottom trace Fig. 4.16) to the stress right after trench etch (top trace Fig. 4.8) indicates, that the residual nitride mask is thinner on top of narrow stripes.

At this time, no explanation for the disappearance of the tensile stress after CMP can be given.

4.2.4 Stress from Pre-Gate Oxidation (*HDP Process*)

This section discusses the influence of trench oxide densification in combination with the pre-gate oxidation in dry or wet ambient. It will be shown that the mechanical stress can increase drastically using the wrong combination of process steps. The increase in stress led to the formation of defects and a strong increase of diode leakage.

After CMP and removal of the residual nitride mask, the HDP oxide in the trenches is densified at 1050°C in N₂ ambient. The mechanical stress in the silicon substrate is now governed by the trench oxide and no longer by the nitride hardmask on top of the active areas. A 20 nm thick pre-gate (PG) oxide is grown prior to well

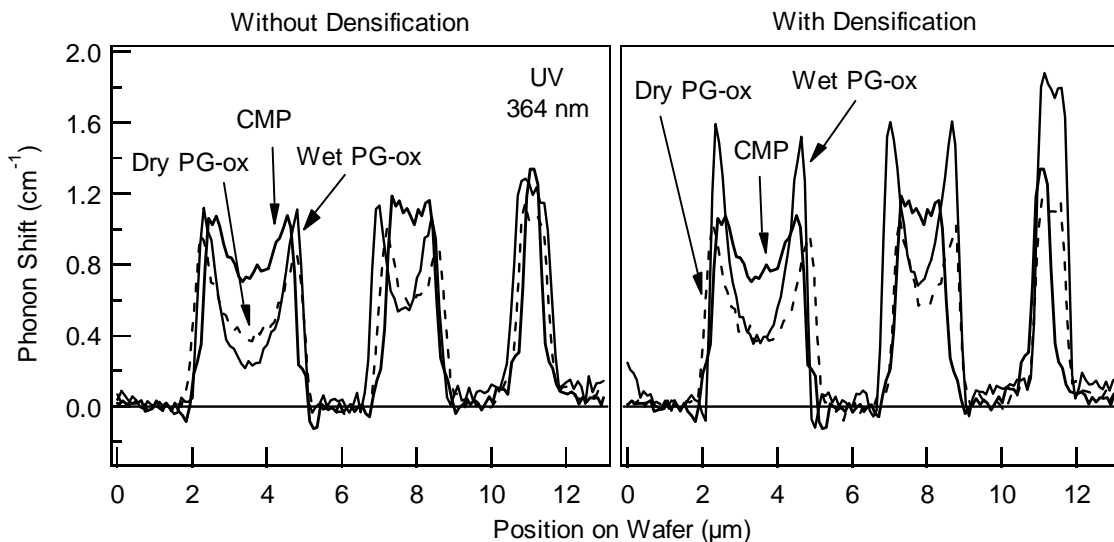


Fig. 4.17: Influence of wet and dry pre-gate (PG) oxidation on mechanical stress in 3, 2, and 1 μm wide active area stripes. The thick solid line shows the stress after CMP and before the removal of the residual nitride mask. Wet PG oxidation after nitride removal and densification increases the stress at the active area edges by 60% compared to dry PG oxidation (right graph). Without densification, the increase of stress with wet PG oxidation is less and nearly the same as with dry PG oxidation (left graph).

implantation at 900°C in wet ambient or at 1075°C in dry ambient. To study the influence of pre-gate oxidation in combination with trench oxide densification on the amount of mechanical stress in the underlying silicon, PG oxidation was performed in wet or dry ambient with and without prior trench densification. The corresponding stress measurements are shown in Fig. 4.17.

Fig. 4.17 contains two diagrams, each comparing the mechanical stress after wet PG oxidation (thin solid line) and dry PG oxidation (dashed line) in the same 3, 2 and 1 μm active areas as shown in Fig. 4.8. The stress after CMP and before the removal of the residual nitride mask (thick solid line) is included as a reference of how the overall stress is changed by the PG oxidation process. The diagram on the right side of Fig. 4.17 compares the stress measurements in samples with densification of the HDP oxide prior to the PG oxidation. The left diagram of Fig. 4.17 shows the same comparison in samples without trench oxide densification. The most distinct difference between the two diagrams is the 60% higher edge stress in the active areas after wet PG oxidation with prior HDP oxide densification (dotted line, Fig. 4.17 right). Without densification of the HDP oxide, the stress is about the same for wet and dry PG oxidation (Fig. 4.17 left).

The increase of stress during wet PG oxidation with prior trench oxide densification can be explained by the growth of additional oxide on the silicon sidewalls. This oxide expands between the densified HDP oxide in the trenches and the silicon active areas, pushing against the sidewalls and increasing the compressive stress in the silicon stripe. In the case of dry PG oxidation no oxide is growing at the Si

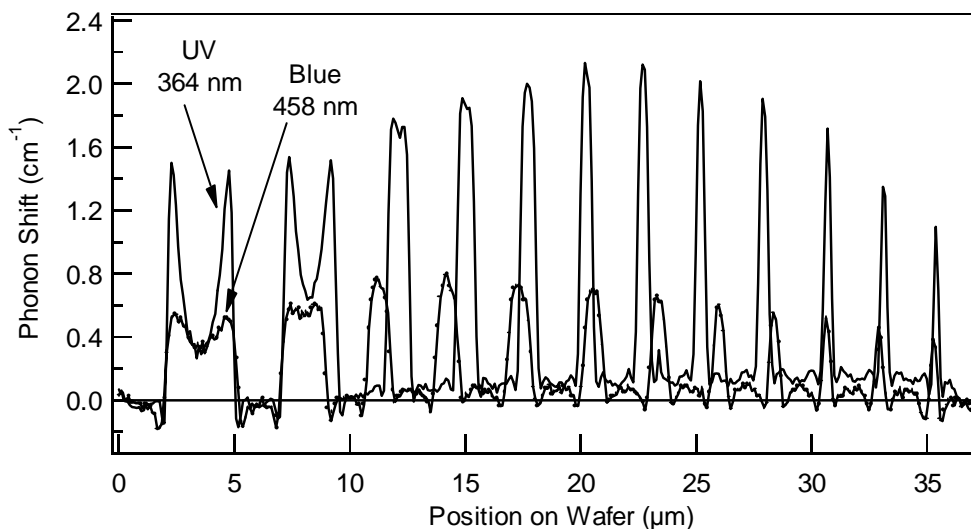


Fig. 4.18: Comparison of stress measurements using UV (364 nm) and blue (458 nm) light for excitation. The sample consists of the same array of active area stripes separated by shallow trenches as shown in section 4.2.1. Only the UV measurement reveals the high stress at the edges of the active area stripes.

sidewalls, and thus no additional stress is induced. If the HDP oxide in the trenches has not been densified, neither wet nor dry PG oxidation leads to an increase in mechanical stress (Fig. 4.17). Oxide still grows on the silicon sidewalls during wet PG oxidation, but now the trench oxide is soft and the growing oxide can expand unhindered into the trench region. In order to obtain good isolation characteristics, it is necessary to densify the trench oxide.

All of the measurements in Fig. 4.17 were obtained using UV light (364 nm). The influence of the pre-gate oxidation ambient in combination with trench oxide densification is only seen in the variations of the high stress at the active area edges. Blue light (458 nm) averages the high corner stress over a depth of over 300 nm, so that changes in those areas are almost invisible. This is shown in Fig. 4.18, comparing stress measurements after wet PG oxidation with prior trench oxide densification using blue and UV light for excitation. The compressive stress in the center of the stripe is the same for blue and UV light (Fig. 4.18), which indicates that the stress in the center of the stripe does not change as quickly with depth as at the edges. UV light, with its surface sensitivity, shows in addition the high corner stress (Fig. 4.18) and therefore also changes in this stress due to changes in technological parameters (Fig. 4.17). The phonon shift reaches a maximum value of 2.2 cm^{-1} in the $0.7 \mu\text{m}$ wide active area stripe and decreases again for smaller stripes. This is a good indication, that the laser spot on the sample is around $0.7 \mu\text{m}$. The laser spot therefore probes the stress from both stripe edges simultaneously, without averaging any of the zero stress from the trenches into the phonon position. For narrower stripes that is exactly what happens and the phonon shift decreases again. To obtain the real stress values for the small stripes, stress modeling is inevitable.

The two traces in Fig. 4.18 show some variations in the positions of the active area stripes. These changes are not real, but are caused by the motorized xy-stage. The measurements are taken with a scanning step size of $0.1 \mu\text{m}$. The size of one step apparently is not always exactly $0.1 \mu\text{m}$, but sometimes a little more or a little less, so that over a distance of 400 measurement points (which corresponds to a distance of $40 \mu\text{m}$) those small variations in step size add up. To ease the comparison of the two traces in Fig. 4.18, the x-values of one trace have been multiplied by a constant factor close to one, so that the positions of the $3 \mu\text{m}$ and $0.3 \mu\text{m}$ stripes coincide.

Stress after N-well implantation, anneal and gate oxidation

Fig. 4.17 showed that mechanical stress increases by 60% after wet PG oxidation with prior trench oxide densification. After PG oxidation the wells are implanted and annealed at 850°C for 10 minutes. Afterwards the PG oxide is removed and a 3.5 nm gate oxide is grown at 650°C in wet ambient. Fig. 4.19 shows the same comparison of stress measurements as Fig. 4.17, but now each wafer shown in Fig. 4.17 has been processed further including N-well implant, anneal, and gate oxidation. As can be seen from the two diagrams of Fig. 4.19, the high corner stress after wet PG oxidation with

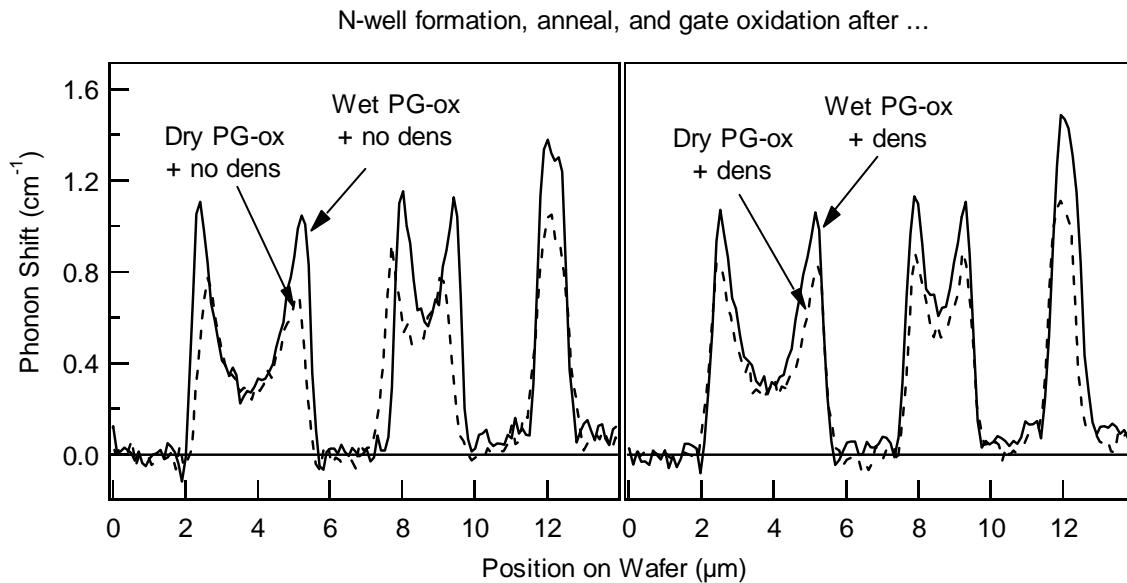


Fig. 4.19: Comparison of mechanical stress after N-well implant, anneal, and gate oxidation in the same 3, 2, and 1 μm wide active area stripes as shown in Fig. 4.17. Left diagram: When the trench oxide had not been densified prior to pre-gate (PG) oxidation in dry (dashed line) or wet (solid line) ambient. Right diagram: When the trench oxide had been densified prior to dry (dashed line) and wet (solid line) PG oxidation. All measurements were obtained with UV light.

prior trench densification (compare Fig. 4.17) has relaxed after N-well formation. The stress now seems to depend only on the PG oxidation ambient, regardless of whether the trench oxide had been densified or not (Fig. 4.19). For the case that the PG oxide is grown in a dry ambient, the stress at the edges is 30-40% lower compared to wet PG oxidation. The next section deals with the correlation of this stress relaxation after well-formation with the formation of defects and a degradation of electrical properties.

Fig. 4.21 shows two transmission electron microscopy (TEM) micrographs¹ of 0.5 μm wide shallow trenches after N-well implant, anneal, and gate oxide formation. The TEM pictures were taken in the same samples as the stress measurements shown in Fig. 4.19 after trench oxide densification and subsequent wet and dry pre-gate oxidation (right diagram of Fig. 4.19). The sample which was processed including trench densification and wet PG oxidation prior to the implant shows defects as shown in the right TEM picture of Fig. 4.21. This formation of defects could explain the stress relaxation observed comparing Fig. 4.17 and Fig. 4.19. The sample processed with dry PG oxidation shows no defects (left picture, Fig. 4.21). This correlates well with the stress measurements, since wet PG oxidation showed initially a 60% higher stress at the active area edges as compared to dry PG oxidation. This is the first experimental

¹ TEM investigations performed by C. Stuer, University of Antwerp, Belgium

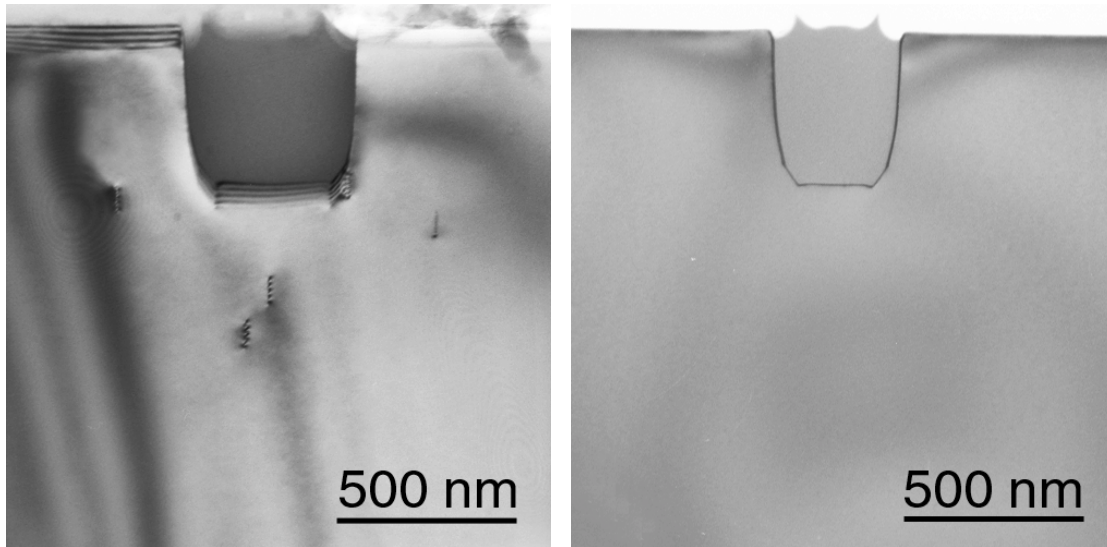


Fig. 4.21: TEM micrographs of a 0.5 μm wide shallow trench after N-well implant, anneal, and gate-oxide formation. Using wet PG oxidation and trench oxide densification prior to the implant shows defects (left), whereas using dry PG oxidation shows no defects (right).

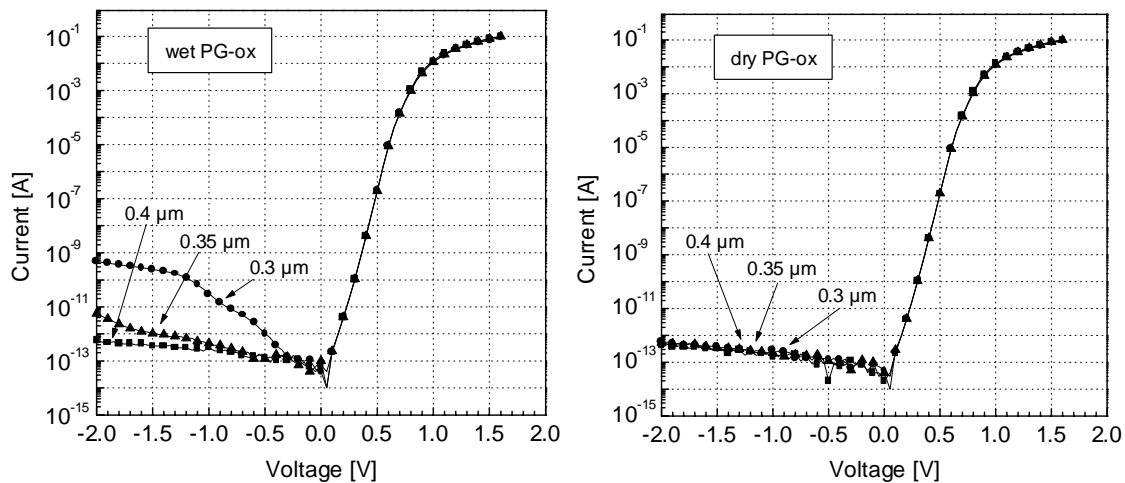


Fig. 4.20: Influence of wet (left) and dry (right) pre-gate oxidation on p^+/n diode leakage measurements across shallow trenches of different widths. When a wet pre-gate oxide is used the leakage current increases depending on the width of the shallow trench (left graph). This is not the case using a dry grown pre-gate oxide (right graph).

correlation of stress measurements with UV micro-Raman spectroscopy and the formation of defects observed with TEM.

A second correlation is given by diode leakage measurements shown in Fig. 4.20. I-V measurements¹ of a p^+/n diode across shallow trenches with changing widths

¹ Performed by S. Pochet, IMEC Leuven, Belgium

indicate, that leakage current increases strongly in narrow trenches where wet PG oxidation is used in the formation process (left diagram, Fig. 4.20). The 0.4 μm shallow trench still shows excellent isolation. However, the leakage current of a diode across a 0.3 μm shallow trench increases by 3 orders of magnitude over the 0.4 μm shallow trench. In diodes where dry PG oxidation was used, no change in leakage current was found as a function of the trench width (right diagram, Fig. 4.20). The I-V characteristics remain excellent down to the narrowest trench (0.3 μm).

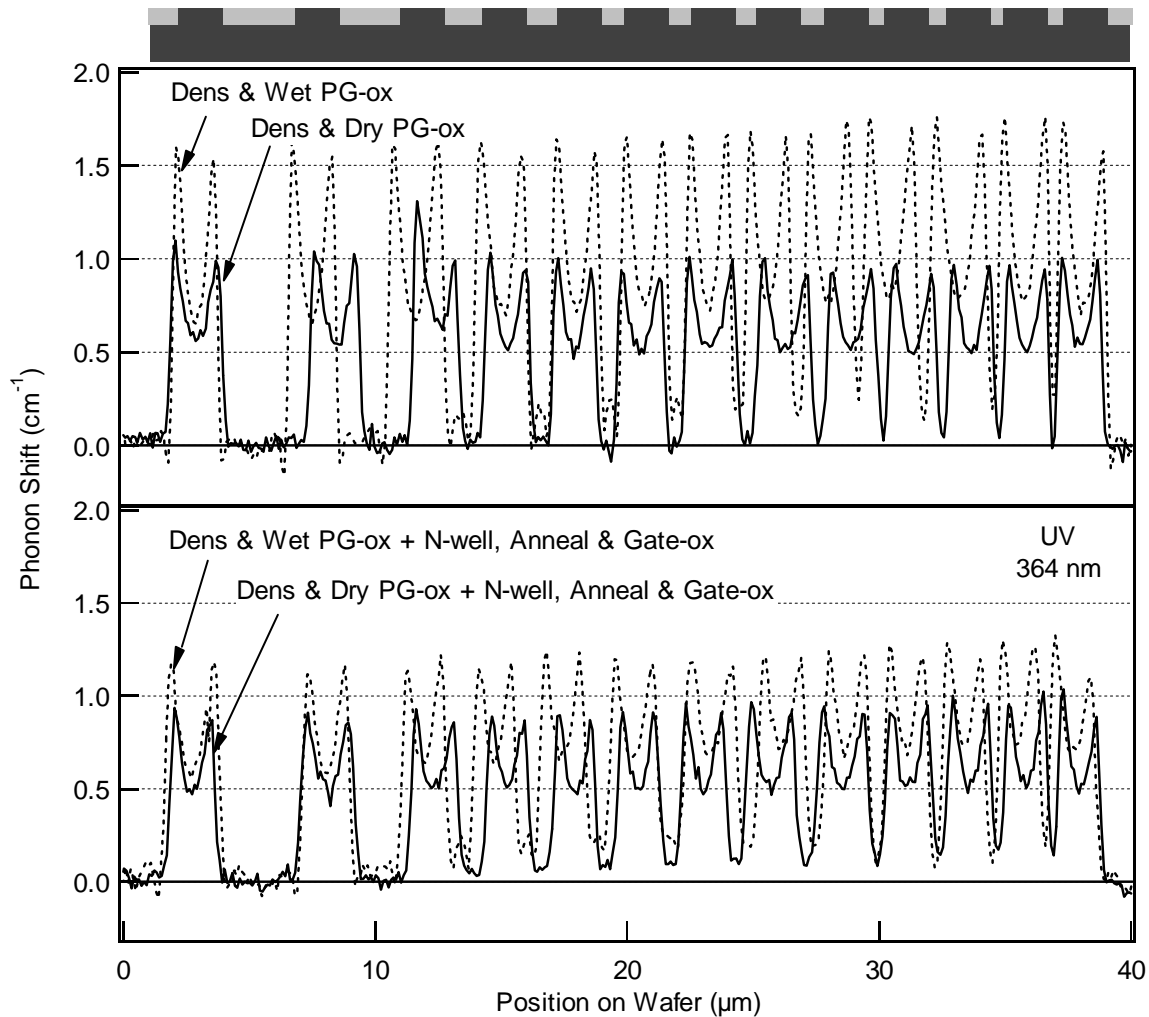


Fig. 4.22: Comparison of stress measurements in an array of 2 μm wide active area stripes separated by shallow trenches of different widths. From left to right the shallow trenches are 3, 2, 1, 0.9, 0.8, 0.7, 0.6, 0.5, 0.45, 0.4, 0.35, and 0.3 μm wide. A schematic drawing of the structure is shown at the top. The top graph compares the stress after wet (dotted line) and dry (solid line) pre-gate (PG) oxidation with prior trench densification. The bottom graph shows the same comparison after the respective wafers have been processed further including N-well implant, anneal, and gate-oxidation. All measurements were obtained with UV light (364 nm).

Influence of Trench Width on Stress

So far, only stress measurements in active area stripes of changing width separated by 2 μm wide shallow trenches have been shown. As long as the trenches are not filled, these are the interesting structures, because the stress causing layers are the nitride on top of the stripe and the sidewall oxide. After trench fill and especially after densification it might be interesting to see how the width of an adjacent trench influences the stress in an active area stripe. The answer is shown in Fig. 4.22.

Fig. 4.22 shows stress measurements in an array of 2 μm wide active area stripes separated by shallow trenches of different width. A schematic drawing of the investigated sample structure is shown at the top of Fig. 4.22. The shallow trenches are 3, 2, 1, 0.9, 0.8, 0.7, 0.6, 0.5, 0.45, 0.4, 0.35, and 0.3 μm wide (from left to right). The top graph of Fig. 4.22 shows the comparison of stress after wet (dotted line) and dry (solid line) PG-oxidation with prior trench densification. The bottom graph of Fig. 4.22 shows the same comparison after the respective wafers have been processed further including N-well implant, anneal and gate-oxidation. All measurements are obtained using UV light.

The result of this comparison is, that the stress in the active area stripes is almost independent of the adjacent trench width. The active area stripes on the left edge of Fig. 4.22 show the same stress as the respective measurements in 2 μm wide active areas shown in Fig. 4.17 (right graph) and Fig. 4.19 (right graph). As the trenches become narrower only a slight increase in stress (on average less than 10%) can be observed. The stress after wet PG oxidation, on the other hand, is 50-60% higher than after dry PG oxidation. This results leads to the conclusion, that chip layout is less important than choosing the right process steps in order to avoid the buildup of large stress.

4.2.5 Evolution of Stress (*HDP Process*)

The identification of process steps that induce large mechanical stress in the silicon substrate is important for the avoidance of defect formation. Once defects have formed in the silicon, it is difficult to find the cause for those defects, since the process history can be quite long. By measuring the stress after each process step, it is possible to identify those steps after which the stress increased drastically. This information can lead to changes in the process flow in order to avoid high stress and thus lower the potential for defect formation. So far, the stress after each major processing step of the shallow trench isolation process called *HDP process* has been shown.

To get an overview of the stress in the complete process Fig. 4.23 shows the value of the phonon shift at the center of the 3 and 2 μm active area stripes investigated in the previous sections, as well as the phonon shift at the edges of the 3, 2 and 1 μm active area stripes. Plotting these values as a function of the process steps, results in the evolution of mechanical stress for the given process flow (Fig. 4.23). One can

immediately see, which process step induces how much stress. The paths indicated in the graph give the evolution for a certain set of technological parameters, such as wet instead of dry pre-gate oxidation. The path with the lowest phonon shift values, which are a direct measure of stress, describes the set of parameters with the lowest potential for defect formation.

Most of the changes in stress with different process parameters became possible only through the use of UV light. Blue light averages too much over the large penetration depth for the changes to become visible. Micro-Raman spectroscopy using UV light for excitation is therefore a real improvement.

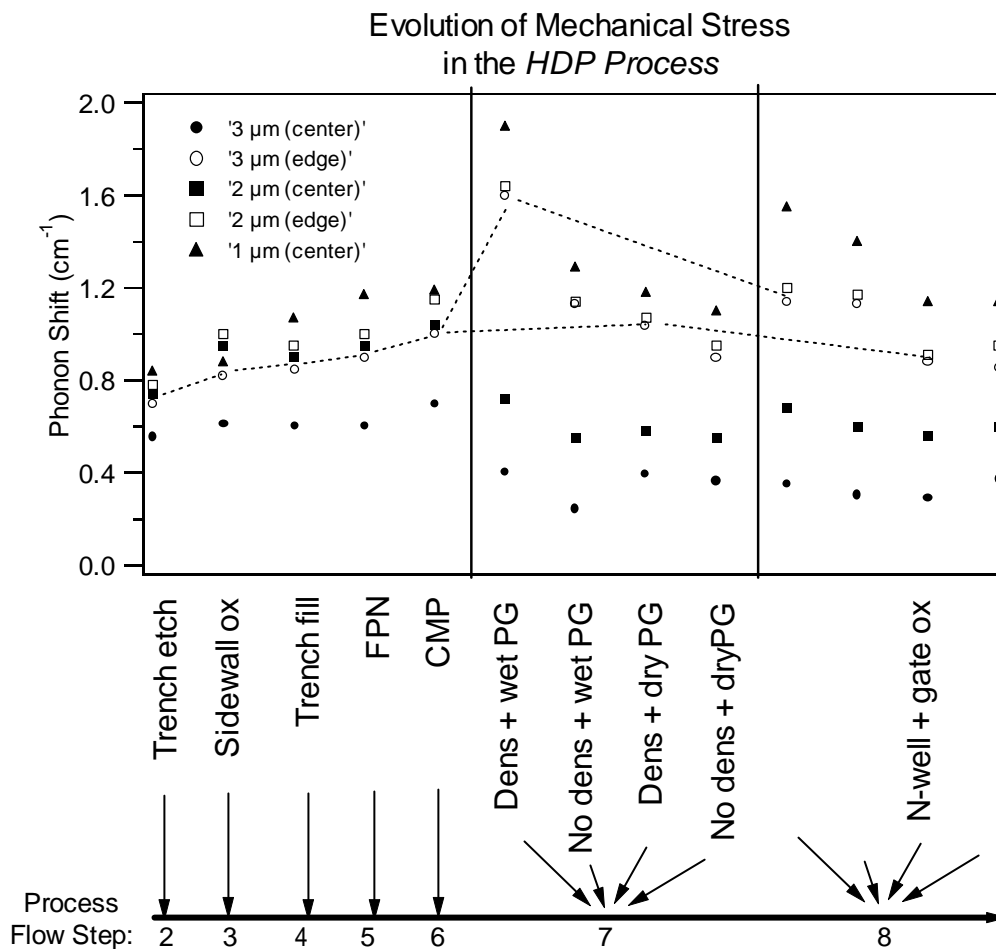


Fig. 4.23: Evolution of mechanical stress through the HDP process as measured by UV micro-Raman spectroscopy. The phonon shift indicating mechanical stress is given for the center and edge of 3, 2, and 1 μm wide active area stripes as a function of the process step, shown below the graph. Two possible stress evolution paths are indicated by dashed lines in the graph. The highest stress is measured after trench densification and wet pre-gate (PG) oxidation.

4.3 Summary

This chapter presented the measurement of mechanical stress in silicon device structures processed with two different shallow trench isolation processes. The main results of this chapter can be summarized as follows:

- Through the use of UV instead of blue light to excite the Raman scattering, the penetration depth of the light into silicon has been reduced drastically from 320 nm for blue light to 12 nm for UV light. Due to its small penetration depth, UV light is very sensitive to near-surface stress. Especially the high stress at structural edges becomes visible, which has so far been averaged away by blue light.
- Stress measurements in device structures smaller than the laser spot of around 0.7 μm (UV light) to 0.9 μm (blue light) have been shown for the first time. Especially with UV light it was shown, that it is possible to measure stress changes in structures as small as 0.3 μm . The quantitative interpretation of measurements in small structures is only possible in combination with stress modeling and the comparison of stress measurements in larger structures. Otherwise, completely wrong conclusions can be drawn from those measurements.
- The ability to observe areas of high stress at critical edge structures enables the monitoring of stress changes due to changes in process parameters. This was demonstrated for a main-stream technology, the shallow trench isolation. Areas of high stress levels with the potential to trigger defects are identified and the influence of process parameter changes on the amount of stress is investigated.
- The influence of the nitride hardmask and the sidewall oxide on the amount of stress in active area stripes has been investigated. It was found that the nitride hardmask induces compressive stress along the nitride/silicon interface. The influence of the pad-oxide remains unclear, since a thicker pad-oxide does not seem to diminish the stress from a likewise thicker nitride layer. The sidewall oxide creates areas of tensile stress in the trench bottom corners and at the same time increases the compressive stress under the nitride hardmask. The amount of stress induced by the nitride hardmask and sidewall oxide is in both cases proportional to the thickness of the respective layers.
- The filling of the trench with a flowable oxide and TEOS in the *TEOS process*, led to the formation of a bird's beak at the top corner of the active area stripes. This bird's beak was identified after flowable oxide deposition and curing, as well as after densification of the trench TEOS in wet and dry ambient through measurements using UV light. The additional areas of very large stress caused by the bird's beak

especially after wet densification are only seen clearly with UV light; they are averaged away by blue light. The identification of the bird's beak was verified by SEM measurements and FE simulations. The comparison with FE simulations also allowed the quantification of the oxidation model used in the simulation.

- The filling of the trench with HDP oxide in the *HDP process*, as well as the formation of the field protecting nitride, does not influence the stress in the underlying silicon very much. After CMP the tensile stress in the trench bottom corners disappears. So far, there is no explanation for this behavior.
- Growing a pre-gate oxide in wet ambient with prior trench oxide densification was shown to increase the stress at the active area edges by 60% as compared to the growth of the same pre-gate oxide thickness in dry ambient. The identification of the influence of the pre-gate formation in combination with trench oxide densification on the amount of stress became possible only through the use of UV light. Blue light averages away the high stress at the active area edges, making the observation of changes in those areas impossible. The stress measurements after wet and dry pre-gate oxidation were correlated for the first time directly with the formation of defects found in TEM and the increase of leakage current in diodes across narrow shallow trenches. It was found that after n-well implant, anneal and gate-oxidation defects had formed if a wet pre-gate oxide was grown prior to the implant. In addition, leakage current increased by several orders of magnitude across 0.3 μm wide shallow trenches as compared to 0.4 μm wide trenches. Using a dry grown pre-gate oxide shows no defects in TEM and perfect I-V characteristics down to the smallest trench.
- The mechanical stress in active area stripes adjacent to finished shallow trench isolation areas was found to be governed by the history of the processing steps more than the size of the STI region. Only a 10% increase in stress was observed in active area stripes adjacent to 0.3 μm wide trenches as compared to 3 μm wide trenches. Different process parameters can increase the stress by as much 60%. Choosing the right process parameters, therefore, seems more important than chip layout.

Part B: Phonons in SiGe

5 Introduction: Why SiGe?

During the last few years, the interest has risen to improve existing silicon technology through the use of $\text{Si}_{1-x}\text{Ge}_x$ and just recently through $\text{Si}_{1-x-y}\text{Ge}_x\text{C}_y$. The preparation of SiGe epitaxial layers on silicon allows one to engineer the band gap and the strain in the epitaxial layer. The SiGe hetero bipolar transistor (HBT) can reach higher frequencies, enabling faster circuits at lower prices than III-V's used so far. This opens up new market segments for silicon technologies, such as mobile communication in the 2-5 GHz band.

But besides the technological aspects, SiGe is also a very interesting material from a physical point of view. Silicon and germanium are miscible over the whole composition range, making it an ideal material system to study the transition of physical properties from silicon to germanium. Although the first publication on SiGe crystals dates back to 1939 [47], there are many open questions concerning the material properties. One reason is the difficulty of growing large volume crystals with high structural quality. At the start of this PhD work, there was no clear understanding of the lattice vibrations of SiGe with sometimes contradictory assignments of various vibrational modes. In addition, a behavior of the Ge phonon in samples with very small silicon concentrations was reported in the literature [72], which could neither be reproduced with Raman measurements nor with theoretical calculations. In this thesis Raman measurements of samples with high structural quality and homogeneity will be presented, which contradict the findings of that publication. Using Raman spectroscopy together with results from Fourier transform infrared spectroscopy (FTIR) absorption, a complete and unambiguous picture of the vibrational modes in SiGe is now available.

SiGe bulk crystals have some very interesting applications. Since Si and Ge are completely miscible over the whole composition range, crystal properties such as bandgap and lattice constant can be varied continuously. The variation of the lattice constant is advantageous for the application of X-ray optical components. The crystals can be used as a monochromator for divergent X-rays [48] and for focusing of X-rays [49, 50]. SiGe bulk crystals are also investigated to be used as solar cells because of the increased sensitivity to the longer wavelengths of sunlight as compared to silicon [51]. SiGe substrates could replace graded-buffer SiGe epitaxial layers on silicon substrates. These graded-buffer layers are layer stacks in which the Ge concentration is gradually increased, in order to finally grow an unstrained SiGe layer or a strained Si layer [52].

Part B of this thesis is organized as follows: Chapter 6 gives a general introduction to the SiGe material system together with a short description of different crystal growth processes and the determination of the Ge content in these crystals. The lattice vibrations of SiGe crystals will be discussed in detail in chapter 7. The first

section of chapter 7 includes an introduction to the absorption- and Raman scattering mechanism. Next, the variation of the Ge phonon for small Si contents will be shown, which contradicts previously published results. It follows the discussion of the development of vibrational modes in SiGe, starting on the Ge-rich side. The silicon atoms induce local vibrational modes in those Ge-rich samples. The different selection rules for absorption and Raman scattering are used to unambiguously identify these local modes. The next section will describe the anharmonic Keating model, which helped to assign the correct vibrational modes, and compare the theoretical and experimental spectra. Chapter 7 closes with a discussion of the influence of disorder on the Ge phonon in Ge-rich SiGe crystals.

6 SiGe Experimental

This chapter deals with the basic properties of SiGe bulk crystals. First, a summary of the main physical properties of SiGe will be given. Secondly, a short description of the different mechanisms used to grow the investigated samples will be presented and the problems with growing large bulk SiGe crystals will be discussed. The last section of this chapter deals with the determination of the exact crystal composition.

6.1 Basic Properties

Both semiconductors silicon and germanium have diamond crystal structure. The crystals are formed by covalent bonding of neighboring atoms. The same holds true for SiGe. The lattice parameter of silicon is 4% smaller than that of germanium (Tab. 6.1). In $\text{Si}_{1-x}\text{Ge}_x$ therefore, the lattice parameter depends on the Ge concentration x . The increase of the lattice parameter with increasing Ge concentration deviates slightly from Vegard's rule, the linear interpolation between the lattice parameters of Si and Ge [53]. This is shown in Fig. 6.1.

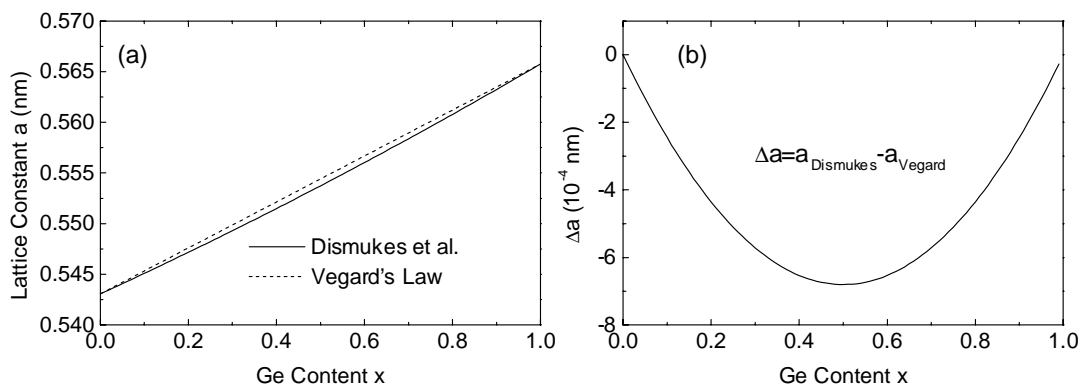


Fig. 6.1: (a) Lattice parameter a of $\text{Si}_{1-x}\text{Ge}_x$ as a function of the Ge content x . The solid line represents experimental values determined by X-ray diffraction from Dismukes et al. [53]. The dotted line shows the linear interpolation of the lattice constant between silicon and germanium (Vegard's Law). (b) Difference Δa between the experimentally determined values for the lattice parameter (Dismukes) and the linear interpolation (Vegard).

Physical Properties	Silicon	Germanium
Crystal structure	Diamond	Diamond
Atom size (Å)	1.17	1.22
Lattice parameter (Å)	5.4307	5.6579
Bond length (Å)	2.35	2.45
Rel. atomic mass	28.1	72.6
Indirect bandgap, T=300 K (eV)	1.11	0.66
Indirect bandgap, T=2 K (eV)	1.170	0.744
Dielectric constant ϵ	12.1	16.2
Carrier mobility (drift)	e ⁻ : 1500	3900
(cm ² /Vs)	h ⁺ : 500	1900
Phonon Deformation Potentials (cm ⁻²)		
K ₁₁ = p	-5.022×10 ⁵	-1.305×10 ⁵
K ₁₂ = q	-6.243×10 ⁵	-1.755×10 ⁵
K ₄₄ = r	-1.9×10 ⁵	-0.99×10 ⁵
Elasticity Constants (Pa ⁻¹ , T = 300 K)		
S ₁₁	7.68×10 ⁻¹²	14.23×10 ⁻¹²
S ₁₂	-2.14×10 ⁻¹²	-2.67×10 ⁻¹²
S ₄₄	12.60×10 ⁻¹²	14.97×10 ⁻¹²

Tab. 6.1: *Physical properties [54], phonon deformation potentials [25,55] and elasticity constants [54] of silicon and germanium.*

Silicon and germanium both have an indirect bandgap. Their respective conduction band minima lie at different points in the Brillouin zone. In germanium the conduction band minimum lies exactly at the L point, whereas in silicon it lies at 85% of the distance from the Γ to the X point going in the Δ direction. The size of the indirect bandgap as a function of crystal composition is shown in Fig. 6.2 (data from [56]). The changeover from a silicon-like bandgap with the conduction band minimum close to the X point to a germanium-like bandgap with the conduction band minimum at the L point, occurs at a germanium concentration of $x = 0.85$.

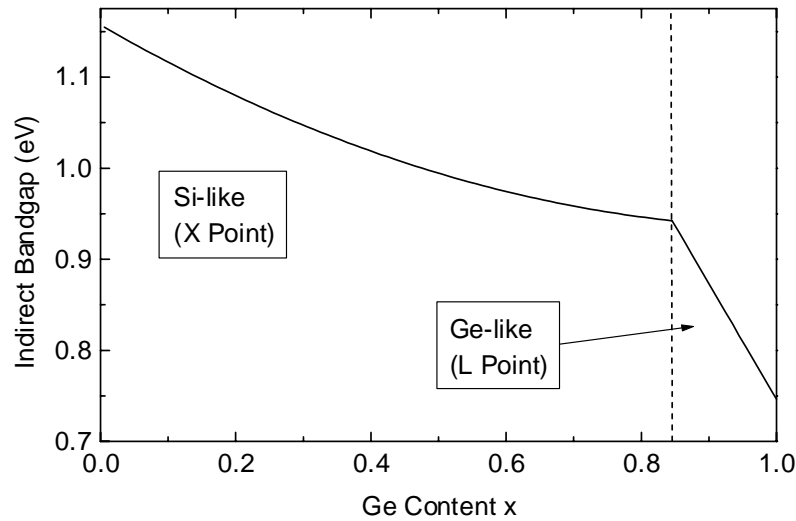


Fig. 6.2: Size of the indirect bandgap of SiGe as a function of germanium content x . At $x=0.85$, the conduction band minimum changes from silicon-like (minimum near the X point) to germanium-like (minimum at the X point) [56].

Values for the phonon deformation potentials or the elasticity constant of $\text{Si}_{1-x}\text{Ge}_x$ are unknown. Roos¹ et al. [57] found from nanoindentation measurements that the elasticity constants for SiGe deviate strongly from Vegard's law. Those findings were later contradicted by Floro et al. [58], who determined Vegard's law to be valid in the composition range $x = 0.15-0.6$. For the phonon deformation potentials of SiGe, no experimental or theoretical data has been published so far. In this thesis, the linear interpolation between the values for silicon [25] and germanium [55] will be used.

6.2 Crystal Growth

Two main factors are responsible for the difficult growth of bulk SiGe crystals:

i) Strong segregation

The distribution coefficient of silicon in germanium is approximately 5, whereas the distribution coefficient of germanium in silicon is only 0.3. While trying to grow Ge-rich crystals, this leads to a strongly enhanced incorporation of silicon into the crystal.

ii) Mechanical stress

The size difference of 4% between the Si and Ge atoms leads to large mechanical stress within the material causing dislocations and even cracks.

¹ Personal Communication: Unpublished measurements performed later confirm the findings of Floro et al.

The samples investigated in this thesis were grown using three different methods:

Ge-rich samples with x larger than 0.9 were grown at the Crystallographic Institute of the University of Freiburg, Germany, using the vertical Bridgeman technique.

Using a vertical zone-melting technique, samples with Ge concentrations larger than 0.4 were also grown in Freiburg.

Si-rich samples with Ge concentrations smaller than 0.1 were grown at the Institute for Crystal Growth in Berlin, Germany, using the Czochralski method.

These three methods will now be described shortly, emphasizing their respective characteristics.

Vertical Bridgeman technique

To grow the crystal, the whole source material is melted. This is achieved in a mono-ellipsoid mirror furnace with a lamp heater. The source material is inside an ampoule, which is lifted vertically from the heating zone. Due to the large distribution coefficient of Si in Ge, a steep silicon gradient is formed at first, when trying to grow crystals with large Ge concentrations. Fig. 6.3 shows an EDX (energy dispersive X-ray) scan along the growth direction of a typical concentration profile obtained with the vertical Bridgeman technique. The seed used for this crystal was germanium oriented along the (111) direction. The crystals typically have a diameter of 9 mm and a length of 30 to 40 mm. More details concerning this technique can be found in references [59] and [60].

Zone melting technique

With this technique only a part of the source material is melted. This melted zone is then moved through the source material starting at the seed crystal. The main advantage with regard to growing SiGe crystals is the fact that the Si concentration can be increased gradually in the molten material. This makes it possible to grow single crystals in the central part of the composition range. A concentration profile for the zone melting technique is shown in Fig. 6.3. The continuous increase of silicon in the crystal is reached by slowly increasing the silicon concentration in the melted zone. The melting of the zone is achieved by two heating lamps, which are situated in a double-ellipsoid mirror furnace. The source material is moved slowly through the common focus of both lamps. The seed for this type of crystal was also a (111) oriented piece of germanium. The crystals have a typical diameter of 9 mm. More details concerning this technique can be found in references [60] and [61].

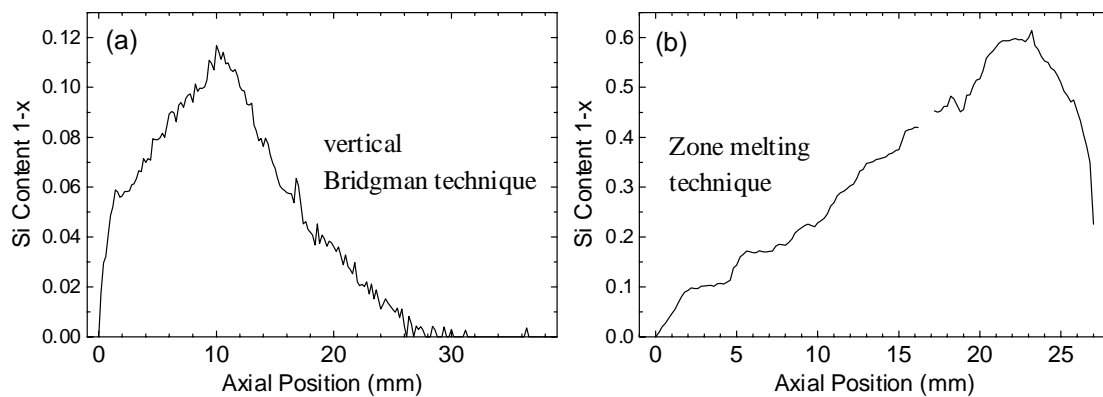


Fig. 6.3: *Si content 1-x along the growth direction of a SiGe crystal grown by (a) the vertical Bridgman technique and (b) the zone melting technique. The values have been measured by EDX¹. The Ge seed crystal is at position 0 mm.*

Czochralski method

With this technique the whole source material is melted inside a crucible. The seed crystal is brought into contact with the molten material and then slowly lifted from the crucible under constant rotation. The crucible is commonly made from quartz. Caused by the chemical reactivity of liquid silicon, oxygen is drawn from the crucible and build into the growing crystal. The crystals grown with this method have oxygen concentrations in the range of 10^{18} cm^{-3} . The seed crystal for this method is silicon. The investigated samples had (111) and (100) orientations. The crystals typically have a diameter of 5 cm. More details about this method and the resulting crystals can be found in reference [62].

6.3 Determination of Composition

Several methods exist to determine the exact composition of $\text{Si}_{1-x}\text{Ge}_x$ crystals. The two most commonly applied methods use the characteristic change of the lattice parameter and the bandgap. The lattice parameter can be determined by X-ray diffraction. A very precise X-ray diffraction technique is named after Bond. In this method the lattice parameter is determined from an exact measurement of the Bragg angle. The Bragg angle is determined with high precision from the angular difference between two symmetrical reflection settings of a Bragg reflection from the same lattice

¹ The EDX measurements were performed at the Crystallographic Institute of the University Freiburg, Germany, by A. Barz and Dr. P. Dold.

plane (hkl) [63]. The error Δa in determining the lattice parameter in the samples investigated in this thesis was in the range $5 \times 10^{-7} \text{ nm} < \Delta a < 1 \times 10^{-4} \text{ nm}$. Once the lattice parameter is known, the crystal composition can be found by using the functional dependence between lattice parameter and composition determined by Dismukes [53] (Fig. 6.1). To get this functional dependence, Dismukes and coworkers determined the composition via density measurements.

The size of the indirect bandgap and thus the composition can be measured by optical methods such as photoluminescence (PL) and absorption. Band edge absorption is an easy measurement, which can be performed at room temperature. The exact procedure has been described by Donecker et al. in [64]. They give a functional dependence between the indirect bandgap and the crystal composition for Si-rich crystals with germanium contents of up to $x=0.16$.

The inverse process to absorption, photoluminescence, can also be used to determine the size of the bandgap. At low temperatures $T < 50 \text{ K}$ the excitonic recombination can be observed. A functional dependence between the Ge contents x and the excitonic bandgap E_{ex} is given by Weber and Alonso [56] for both Si-rich and Ge-rich samples.

To compare the functional dependencies from Dismukes and from Weber and Alonso, the lattice parameter of some samples were determined by the X-ray Bond

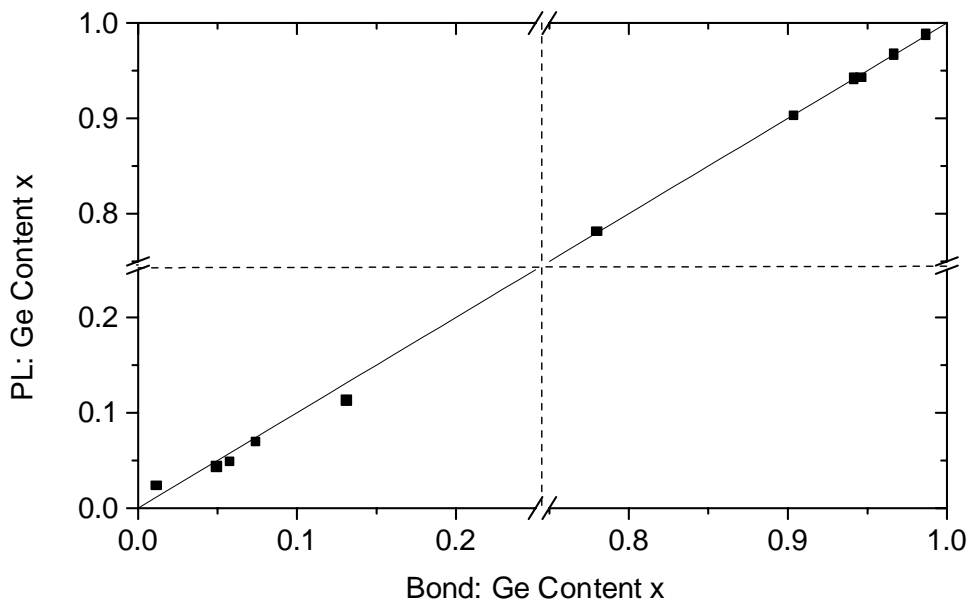


Fig. 6.4: Comparison of Ge contents x determined by photoluminescence (PL) according to Weber and Alonso [56] and by the lattice constant (Bond method) according to Dismukes [53]. The error bars are smaller than the symbols. Both axes are interrupted, since experimental data points are only shown for Si- and Ge-rich samples. The solid line has a slope of 1. On the Ge-rich side the agreement between the two methods is very good. On the Si-rich side there are some deviations.

method and the Ge content x was determined with the dependence given by Dismukes et al. [53]. We also determined the excitonic bandgap from the luminescence of the free exciton and used the dependence given by Weber and Alonso [56] to determine the Ge content x . The comparison of both methods is shown in Fig. 6.4. The solid line has a slope of 1 and indicates exact agreement between the values for Ge content x determined via the lattice constant and via PL. For Ge-rich samples the agreement is very good. On the Si-rich side slight deviations occur. The functional dependence given by Weber and Alonso for the Si-rich side was determined in samples of sometimes poor quality. In those samples the free exciton couldn't be observed and they used defect-bound excitons [56]. They assumed certain values for the bonding energies of these excitons in Si and Ge and interpolated the values for SiGe according to the effective masses and the dielectric constants of Si and Ge. This method together with the poor sample quality provides enough room for errors to explain the deviation for the Si-rich side.

Raman spectroscopy can also be used to determine the composition of SiGe crystals, via the shift of the optical silicon phonon. Functional dependencies between this shift and crystal composition have been given by Alonso and Winer [69] and Tsang et al. [65]. These dependencies are valid for Si-rich crystals with Ge contents of approximately up to $x=0.4$.

A direct chemical analysis of SiGe to determine the crystal composition is difficult. Both elements Si and Ge are too similar in most properties. The only direct determination of composition is by density measurements.

7 Phonons in SiGe

In this chapter the phonon spectrum of SiGe will be described and analyzed. The investigation of phonons delivers information on where the atoms are situated in the crystal and their respective bonds. For compound crystals, such as SiGe, it may even be possible to identify a near range order. Using infrared (IR) absorption and Raman spectroscopy for example, it was found that in strained $\text{Si}_{1-y}\text{C}_y$ layers on silicon substrates the carbon atoms occur preferentially on third-nearest neighbor sites [66]. In covalent materials, the inter-atomic forces are dominated by short range interactions. The lattice vibrations therefore give information about the local atomic symmetry.

Measuring the lattice vibrations with Raman spectroscopy alone does not convey a complete picture, because certain vibrational modes are invisible due to the selection rules. These modes are said to be Raman-inactive (compare section 2.2). In crystals with a center of inversion, the Raman-inactive modes can be observed by infrared absorption. In silicon and germanium infrared light is only absorbed via multi-phonon processes, meaning that at least two phonons are involved in the absorption process. In SiGe the crystal symmetry is lowered through the disordered arrangement of the atoms and thus one-phonon absorption and local modes can be observed also.

In this chapter, the developing lattice vibrations in Ge-rich crystals with small Si contents will be shown and identified. The precise identification of the different modes became possible only through the comparison of low temperature Raman spectra ($T < 80 \text{ K}$) and IR absorption measurements, together with theoretical calculations using the anharmonic Keating model. The influence of disorder on the Ge phonon at 300 cm^{-1} in Ge-rich SiGe will also be discussed. The introduction of Si atoms into the germanium lattice should shift the Ge phonon to higher energies due to the decreasing lattice constant. Instead, the Ge phonon shifts to smaller energies. This is caused by disorder, which breaks the crystal symmetry and softens the selection rules, so that phonons with $k > 0$ are also involved in the scattering process. The resulting decrease in phonon energy results in an over-compensation of the increase caused by the change in lattice constant.

This chapter starts with the presentation of a Raman and IR absorption spectrum of SiGe. Using these spectra, the most important publications dealing with the lattice vibrations of SiGe will be reviewed. Next, a short introduction to absorption spectroscopy and a description of the vibrational modes that can be observed by this technique will be given. The next section describes the lattice vibrations in Ge-rich SiGe crystals by comparing Raman and IR absorption together with theoretical calculations. A discussion of the Ge phonon at 300 cm^{-1} and a summary will close this chapter.

7.1 Introduction

Fig. 7.1 shows the comparison of a Raman and an IR absorption spectrum of a Ge-rich sample in the spectral range 100-600 cm^{-1} . The Raman spectrum shows several peaks at 300 cm^{-1} , 400 cm^{-1} and around 460 cm^{-1} . The peak at 300 cm^{-1} is the characteristic optical phonon mode of Ge. This mode is only Raman active, just like the

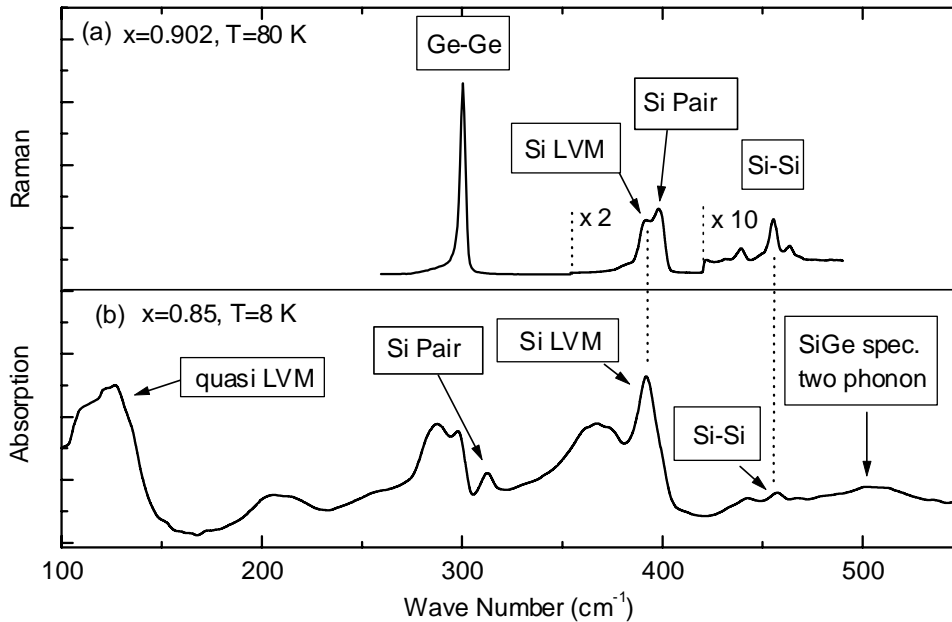


Fig. 7.1: (a) Raman and (b) absorption¹ spectrum of Ge-rich SiGe crystals with similar Ge contents x . Si-Si and Ge-Ge denote vibrations of bonds between Si and Ge atoms. Si pair denotes the vibration of two neighboring Si atoms. In Ge only the optical phonon in the center of the Brillouin zone at 300 cm^{-1} is Raman active. Additional modes in the range from 400 cm^{-1} to 460 cm^{-1} appear through the incorporation of Si into the crystal. LVM stands for localized vibrational mode. The defect induced SiGe specific absorption in the absorption spectrum are superimposed by a strong two-phonon background.

optical phonon mode of Si at 520 cm^{-1} . The modes observed in the spectral range from 400 cm^{-1} to 460 cm^{-1} are SiGe specific vibrational modes. These modes are caused by isolated Si atoms (local vibrational mode, LVM) and neighboring Si pairs. Vibrations caused by the Si atoms in Ge-rich SiGe crystals can be observed much easier by Raman spectroscopy than by absorption, since the multi-phonon background is much smaller for Raman than for absorption spectroscopy. The SiGe specific absorption shown in Fig. 7.1 is superimposed by a strong two-phonon background.

The phonon spectrum of bulk SiGe crystals has already been discussed in a number of publications. Most of the published results were obtained by Raman

¹ The absorption measurements shown in this chapter were performed by Dr. Markus Franz.

spectroscopy. In 1966, Feldman et al. were the first to publish Raman measurements of Ge-rich samples [67]. They identified the localized vibrational mode (LVM) of Si in Ge at 390 cm^{-1} . They also observed a broad peak at 460 cm^{-1} . This broad peak consisted of two unresolved peaks, which Feldman et al. ascribed to the two Raman active modes of Si pairs.

Brya measured Raman spectra of poly-crystalline samples over the whole composition range. He thus determined the shift of the various vibrational modes with changing composition [68]. Brya reported Raman modes at 445 cm^{-1} and 460 cm^{-1} for Ge content $x \geq 0.1$. He assigned the mode at 445 cm^{-1} to Si pairs and the mode at 460 cm^{-1} to larger Si clusters.

Alonso and Winer investigated three fully relaxed SiGe layers on Si substrates with Ge contents $x = 0.28$, $x = 0.55$ and $x = 0.77$ [69]. They also calculated the Raman spectra using the normal Keating model and thus assigned the modes at 460 cm^{-1} to Si clusters. In an earlier paper, Lockwood and coworkers [70] assigned certain Raman modes to an ordered Si-Ge structure in strained SiGe layers. Alonso and Winer showed, that these Raman modes are also observed in disordered SiGe crystals.

Another paper by Gaisler et al. concentrated more on the spectral range of the localized Si mode at 390 cm^{-1} [71]. They performed measurements also at 80 K and observed the development of a second mode at 400 cm^{-1} with increasing Si concentration (Fig. 7.1). Gaisler et al. explained the development of this second mode with the increasing influence of additional Si atoms in the near vicinity of a single Si atom, changing the frequency of the localized vibration at 390 cm^{-1} . This interpretation is not correct, though, as will be shown in section 7.4.1.

A paper dealing exclusively with the Raman active Ge phonon at 300 cm^{-1} was published by Fuchs et al. [72]. They found, that for small Si concentrations the Ge phonon initially shifts to higher energies. With increasing Si content $1-x > 0.02$ they then observed a shift of the Ge phonon to smaller energies. It will be shown later in this chapter, that this behavior observed by Fuchs et al. could not be reproduced with our samples. Instead, the observation of a continuous downshift of the Ge phonon with increasing Si content will be presented [74].

In general, absorption spectra of bulk SiGe crystals have been investigated much less than Raman spectra. This may be due to the need for crystals of high quality to obtain good absorption spectra as compared to Raman measurements. The Raman spectra were obtained with the 514.5 nm line of an Ar^+ -ion laser. The penetration depth of this laser light into silicon is around 760 nm (see chapter 2). During absorption measurements the light passes through the total thickness of the sample, which is typically 0.5 to 1.5 mm . Sample homogeneity and purity is therefore extremely important. The crystal composition also has to be constant over the sample thickness to minimize line broadening. Another quality factor for absorption measurements is the defect density. If the defect concentration is too high, the sample will become opaque through absorption of the IR light by defects.

The first investigation of phonon absorption in SiGe was published by Braunstein in 1962 [75]. He reported on the most significant changes in the spectral range of two-phonon absorption for the whole composition range. Details in the phonon absorption spectra, such as the localized Si vibration, could not be observed by his measurements.

This was accomplished by Cosand and Spitzer in 1971 [76]. They investigated Ge-rich samples with $x > 0.88$ and Si-rich samples with $x < 0.12$. They identified the localized Si vibration in absorption spectra of Ge-rich samples and band-modes on the Si-rich side of the composite crystal. Theirs is the only paper which deals with phonon absorption of Si-rich samples.

About 10 years later in 1980, Shen and Cardona discovered a quasi-localized mode in two Ge-rich samples with $x = 0.89$ and $x = 0.84$, caused by the introduction of Si atoms into the Ge-rich crystals [77]. Another 10 years later in 1990, Humlicek et al. published measurements in Ge-rich samples with very small Si contents of up to $1-x = 0.01$ [78]. Through the measurement of difference spectra between SiGe and Ge samples, the effective charge of the localized Si vibration was determined. They also observed defect induced two-phonon absorption.

Besides all these experimental publications of lattice vibrations in SiGe, some theoretical papers have also been published [79, 80, 81]. The results of these paper will be discussed in the following sections, comparing them to the experiments.

Despite the many papers published since the 1960's, several open questions concerning the lattice vibrations of SiGe remained at the start of this thesis. In the above mentioned publications of Raman and absorption measurements of SiGe bulk crystals the uncertainty concerning the correct assignment of the Raman active mode at 400 cm^{-1} and the modes in the range around 460 cm^{-1} and the existence of this mode in absorption spectra remained. A reason for this uncertainty lies in the fact that many investigations were performed in samples with Si concentrations $1-x > 0.05$. The concentration range of $1-x < 0.05$ is especially important for the correct assignment of the vibrational modes of the Ge-rich crystals. In samples with these small Si contents, it was possible to observe the vibrational modes of isolated Si atoms, Si pairs etc.. As the Si content increases even more, the assignment of separate vibrational modes to the peaks in the spectra becomes difficult since larger Si clusters are formed. Another reason for the uncertainty is caused by the fact, that most measurements are performed at room temperature. Since the vibrational peaks of composite crystals are often broadened, the peaks can be resolved much better at lower temperatures ($T < 80 \text{ K}$).

7.2 Phonon Absorption in Silicon and Germanium

The theory of Raman scattering is presented in chapter 2. Here, the theory of phonon absorption by infrared light will shortly be reviewed. The different selection rules of Raman and IR absorption will later assist in the correct assignment of the SiGe

vibrational modes. The absorption of light through phonons results from the coupling of the incident photon to the phonon via an electric dipole moment. This is the difference to Raman scattering, where the photon couples to the phonon via a change in the polarizability of the crystal (compare chapter 2.2). The electric dipole moment μ existing in a crystal is influenced by the lattice vibrations and can be expanded into a Taylor series with respect to the shift q_i of the i -th atom from its equilibrium position:

$$\mu = \mu_0 + \sum_i \left(\frac{\partial \mu}{\partial q_i} \right)_0 q_i + \frac{1}{2} \sum_{i,j} \left(\frac{\partial^2 \mu}{\partial q_i \partial q_j} \right)_0 q_i q_j + \dots \quad (7.1)$$

The index 0 indicates the equilibrium position. The probability w for an optical transition between an initial state i and a final state j is given by the following matrix element:

$$w \propto |\langle i | \mu | j \rangle|^2 \quad (7.2)$$

The first term in Eq. 7.1, μ_0 , represents a static dipole moment as it is present in ferroelectric crystals, but not in Si or Ge. The second term in Eq. 7.1 is proportional to the shift q_i of the atoms, indicating that a phonon induces a linear dipole moment to which a photon can couple. This term describes the process of one-phonon absorption. This is the dominant absorption process in III-V and II-VI semiconductors. In silicon and germanium this process is not possible due to the cubic crystal symmetry. A shift of the identical atoms within the diatomic base from their equilibrium positions does not

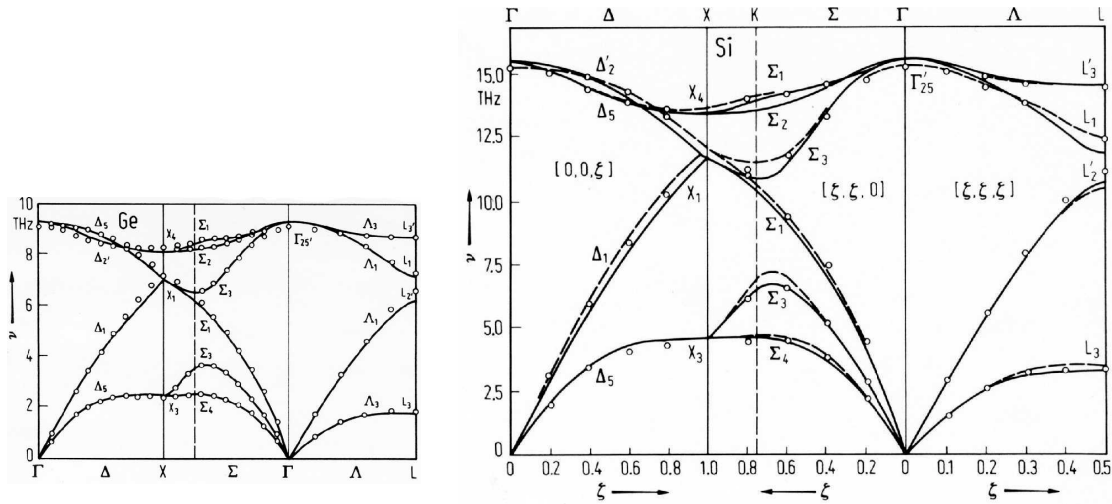


Fig. 7.2: Phonon dispersion curves of germanium (left) and silicon (right) [54]. The energy scales are shown in the same size for better comparison. Points in the graphs are experimental values and the solid lines theoretical curves. The optical phonons of both materials have their maximum energy at the Γ point in the center of the Brillouin zone. For Ge the energy corresponds to 300 cm^{-1} and for Si to 521 cm^{-1} .

lead to a dipole moment. For diamond type crystals the factor $d\mu/dq$ in Eq. 7.1 is zero. The following terms of Eq. 7.1 are nonlinear with respect to q . They stand for two-phonon, three-phonon, etc. processes, meaning that at least two phonons are involved in the absorption process. Two-phonon absorption is the dominant process in silicon and germanium. The probability of an optical transition (Eq. 7.2) decreases with the number of phonons involved in the absorption process. Three- and four-phonon absorption has been observed in silicon and germanium, but with much smaller intensity than two-phonon absorption.

The two-phonon absorption process can be understood from the simple model given by Lax and Burnstein [82] and Winer and Cardona [83]. One of the two phonons breaks the symmetry of the crystal, inducing a charge redistribution through the overlap of atomic orbitals. The other phonon vibrates these charges and thus induces a dipole moment to which a photon can couple. It becomes clear from this model, that only optical phonons induce an asymmetric shift of the atoms in the diatomic unit cell, so that at least one optical phonon is always involved in the absorption process.

The selection rules for the phonon absorption process are determined by crystal symmetry. In silicon and germanium one-phonon absorption is forbidden due to the cubic symmetry. Defects can destroy this symmetry locally and give rise to different absorption processes. The vibrational modes induced by defects can be divided into three groups [84]:

i) Band modes

The lattice vibrations caused by the defects lie energetically within the phonon band of the perfect crystal.

ii) Localized modes

The vibrational modes lie energetically above the phonon modes of the unperturbed crystal.

iii) Gap modes

As the name implies, these modes lie energetically in the phonon dispersion gap between the acoustical and optical branches.

The mass of the defect atom m_{defect} in relation to the atomic mass of the host material m_{host} determines which type of vibrational mode is induced in the crystal. Band modes are induced, if the defect atom is heavier than the host atoms ($m_{\text{defect}} > m_{\text{host}}$). The vibrational frequency caused by a heavier atom lies in the phonon band and can therefore propagate through the crystal. The local symmetry of the crystal is broken and one-phonon absorption becomes possible, even in silicon and germanium. This is called defect induced one-phonon absorption.

If the band mode lies in an energetic regime, where the phonon density of states is very small, the amplitude of the vibration can become rather large. This is called in-band resonance or a quasi-local vibrational mode (quasi-LVM). This mode can be

observed in the absorption spectrum of Fig. 7.1 at 150 cm^{-1} . Details on the assignment of this mode can be found in [74].

Local modes are caused by atoms with a smaller mass than that of the host material ($m_{\text{defect}} < m_{\text{host}}$). The energy of these vibrational modes lie above the phonon energies of the host crystal and the phonons can not propagate through the crystal. The amplitude of the vibration decays exponentially away from the defect. The vibration is thus localized at the defect site. The same holds true for gap modes. In silicon and germanium, unlike in III-V semiconductors, the phonon dispersions don't have a gap between the acoustical and optical branches and gap modes therefore do not exist (Fig. 7.2).

7.3 The Si Local Vibrational Mode

Dawber and Elliot developed a model for the vibrational modes of defects in silicon based on a Debye model [85]. Applying this theory to germanium results in an energy of 392 cm^{-1} for the localized vibrational mode of an isolated Si atom. For this

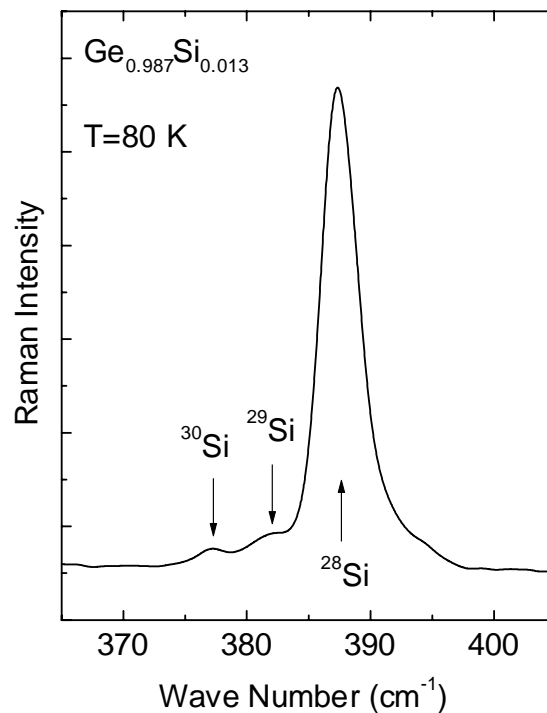


Fig. 7.3: Raman spectrum of a $\text{Ge}_x\text{Si}_{1-x}$ sample with $x = 0.013$ recorded at 80 K showing the Si localized vibrational mode (LVM). Next to the strong central line of the ^{28}Si isotope with natural abundance 92.2% two additional satellite lines are seen. These are caused by the other two isotopes of silicon: ^{29}Si (4.7%) and ^{30}Si (3.1%).

reason Feldman et al. assigned the vibrational mode observed in Raman spectra at 390 cm^{-1} to the localized Si mode [67]. Cosand and Spitzer identified the Si local mode for the first time in absorption spectra for this same reason [76]. The cross section for the absorption is very small at $4 \times 10^{-21} \text{ cm}^2$ [76]. The reason for this small value lies in the covalent nature of the bonds between Si and Ge and only the small difference in electro-negativity.

Since the Ge atoms are much heavier than the Si atoms, a strong localization of the vibration of isolated Si atoms in germanium can be expected. Theoretical calculations have shown, that the neighboring Ge atoms of a vibrating Si atom are almost at rest [81]. Setting the mass of the Ge atoms in these calculations to infinity changed the vibrational energy of the Si atoms by no more than 5% as compared to realist values for the Ge atoms. The vibrations of isolated Si atoms, Si nearest neighbor pairs, etc. are therefore localized almost entirely at the corresponding lattice sites.

Fig. 7.3 shows a Raman spectrum of the Si localized vibrational mode recorded at 80 K in a Ge-rich SiGe sample containing only 1.3 % silicon. Besides the strong central line two small satellite peaks can be seen. These three lines are assigned to the three different isotopes of silicon: ^{28}Si , ^{29}Si and ^{30}Si . The isotopes have a natural abundance of 92.2%, 4.7% and 3.1%, respectively. The relative intensities of the three peaks shown in Fig. 7.3 correspond to the abundances of the isotopes. The energy of a localized vibrational mode is determined mainly by the mass of the vibrating atom. If one assumes that the strength of the bonds with the neighboring Ge atoms is the same for all three Si isotopes the frequencies of the vibrations of the three isotopes should be different according to their corresponding masses. The energy shift of the two satellite peaks with respect to the central peak corresponds well with the mass ratios of the isotopes:

$$\omega_{29} / \omega_{28} \approx \sqrt{m_{28} / m_{29}} \quad \text{and} \quad \omega_{30} / \omega_{28} \approx \sqrt{m_{28} / m_{30}}$$

The isotope effect was observed for the first time during this thesis [73, 74].

7.4 SiGe-Specific Vibrational Modes

In this section the modes at 400 cm^{-1} and around 460 cm^{-1} in the Raman spectrum shown in Fig. 7.1 (a) and the modes at 310 cm^{-1} , 370 cm^{-1} and 460 cm^{-1} in the absorption spectrum of Fig. 7.1 (b) will now be analyzed. All of these modes are caused by vibrations of Si atoms with different neighbor atoms. The details of these configurations are worked out in detail in the following sections.

7.4.1 Infrared and Raman Active Modes

As discussed in section 7.2 the absorption of infrared light by lattice vibrations is determined by an electric dipole moment. The Raman scattering process on the other hand takes place when the polarizability of the atoms as they are moved from their equilibrium positions changes. The different selection rules for infrared and Raman active lattice vibrations make the assignment of vibrational modes easy through the comparison of Raman and IR absorption spectra.

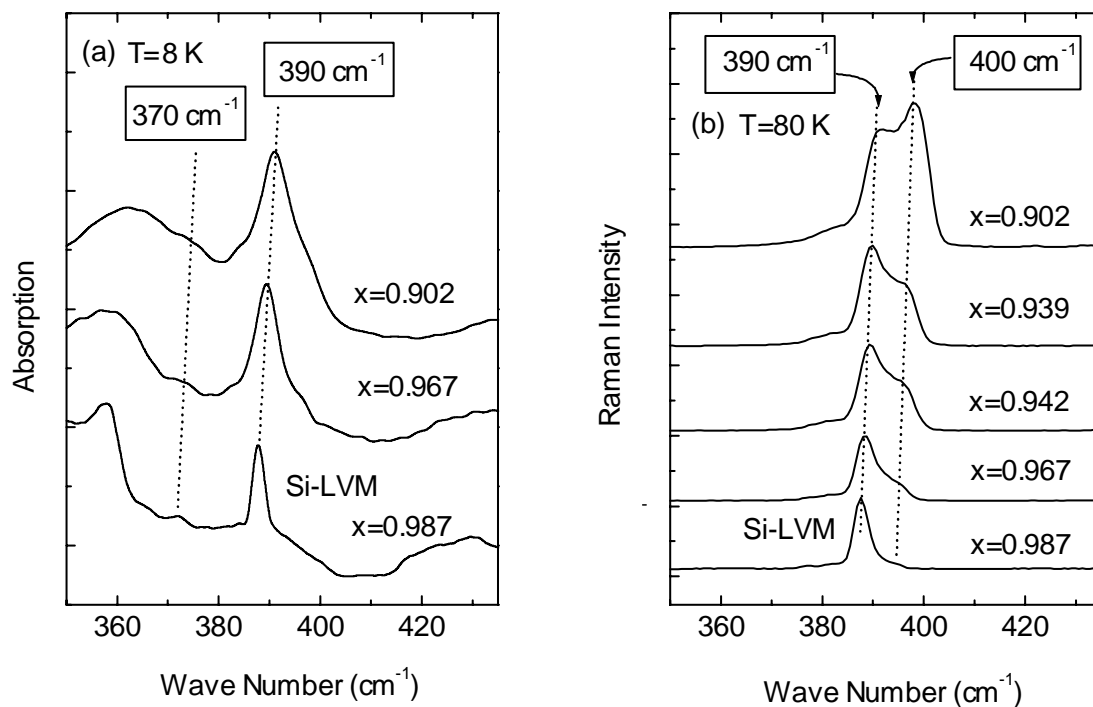


Fig. 7.4: Absorption (a) and Raman (b) spectra of a series of Ge-rich samples in the spectral range of the Si localized vibrational mode. The SiGe specific absorption in this range is the localized Si mode at 390 cm^{-1} shifting slightly to higher energies with increasing Si concentration. Another weak absorption is seen at 370 cm^{-1} . This mode is not present in the Raman spectra. The Raman spectra on the other hand show an additional peak at 400 cm^{-1} developing on the high energy side of the localized Si mode. This mode is only Raman active.

Fig. 7.4 shows the comparison of Raman and absorption spectra of the spectral range in which the Si localized vibrational mode occurs. Looking at the SiGe specific absorption in the absorption spectra one sees a weak line at 370 cm^{-1} and the localized mode at 390 cm^{-1} . The line at 370 cm^{-1} is not present in the Raman spectra and is thus not Raman active, but solely IR active. In the Raman spectra of Fig. 7.4 an additional

line appears at 400 cm^{-1} , whose intensity increases strongly with increasing Si content. This mode is only Raman active and not IR active.

These two modes at 390 and 400 cm^{-1} have already been observed by Gaisler and coworkers in Raman spectra of Ge-rich samples [71]. They explained the development of the mode at 400 cm^{-1} with the change of the energy of the mode at 390 cm^{-1} . The number of Si atoms in the vicinity of an isolated Si atom with four neighboring Ge atoms increases with increasing Si concentration. Since influence is assumed to shift the mode to higher energies. In this model from Gaisler et al. the mode shifts increasingly fast the more Si atoms are on neighboring lattice sites. This explanation of the mode at 400 cm^{-1} is obviously wrong, as can be seen from the absorption spectra of Fig. 7.4. Since the localized mode is also infrared active, the absorption band should also shift from 390 cm^{-1} to 400 cm^{-1} with increasing influence from neighboring Si atoms. This is not the case. The mode at 400 cm^{-1} is definitely only Raman active and appears on the high energy side of the 390 cm^{-1} mode. With increasing Si content both modes shift to slightly higher energies.

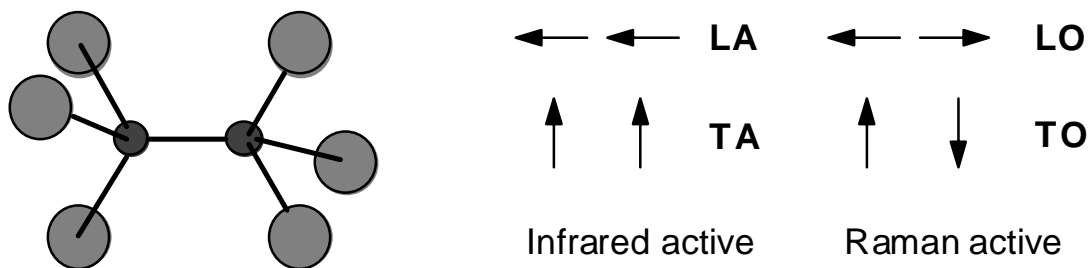


Fig. 7.5: Schematic drawing of a Si nearest neighbor pair defect in germanium. This defect is of D_{3d} symmetry, inducing two IR active and two Raman active vibrational modes. The arrows indicate the vibrations of the two neighboring Si atoms.

Since the mode at 400 cm^{-1} appears with increasing Si concentration, Si nearest neighbor (Si-NN) pairs are a likely cause. Two directly neighbored Si atoms in a Ge lattice induce a defect of D_{3d} symmetry. Two infrared active and two Raman active vibrational modes result from this symmetry of the Si nearest neighbor defect [86]. The possible vibrational modes are shown in Fig. 7.5.

The vibration of the two IR active modes does not depend on the strength of the bond between the two Si atoms. The energy of the IR active modes of the Si nearest neighbor defect should be lower than the energy of an isolated Si atom, because the pullback force of one bond is effectively missing. The Raman active modes in Fig. 7.5 should have a higher energy than the localized mode, since the vibrational energy in this case is determined mainly by the bond between the Si atoms which is stronger than the bond between the Si and Ge atoms. An exact calculation and assignment of the possible vibrational modes in SiGe can be done using the anharmonic Keating model. This is presented in the next section.

7.4.2 Anharmonic Keating Model

The anharmonic Keating model has been developed by Rucker and Methfessel [81]. A summary of the main points of their theory follows.

According to Keating the deformation energy W of a crystal with diamond structure and lattice constant a_0 can be described as [87]:

$$W = \sum_{i,j} \frac{\alpha}{a_0} [\Delta(r_{ij}^2)]^2 + \sum_{i,j,k \neq j} \frac{\beta}{a_0^2} [\Delta(\mathbf{r}_{ij} \cdot \mathbf{r}_{ik})]^2 \quad (7.3)$$

The vector \mathbf{r}_{ij} connects two neighboring atoms as shown in Fig. 7.6. The first term describes the change in lattice constant between the neighboring atoms i and j via the bond-stretching force constant α . The second term describes the change in bond angle θ between the bonds of atoms i with its neighbors j and k via the bond-bending force constant β . Here, Δ denotes the change relative to the equilibrium position of the perfect diamond type crystal due to a distortion, i.e.

$$\Delta(\mathbf{r}_{ij} \cdot \mathbf{r}_{ik}) = \mathbf{r}_{ij} \cdot \mathbf{r}_{ik} - \mathbf{r}_{ij}^0 \cdot \mathbf{r}_{ik}^0 \quad (7.4)$$

The standard Keating model delivers good results for elemental semiconductors [87]. It is inadequate for alloys of group IV crystals such as SiGe. The atomic radii are quite different and large local strains are induced in the crystals. The strain energy is not a quadratic form in the deformations and the harmonic approximation of the Keating model is thus no longer sufficient to describe the lattice vibrations. Anharmonic effects have to be included as well. This problem has been solved by Rucker and Methfessel by scaling the force constants α and β regarding the bond length and bond angle. The scaling laws have been derived from *ab initio* density-functional calculations:

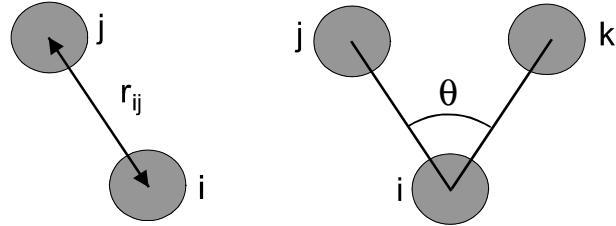


Fig. 7.6: Schematic representation of the nearest neighbor forces.

$$\alpha_{ij} = \alpha_{ij}^0 \left(\frac{r_{ij}^0}{r_{ij}} \right)^4 \quad \text{and} \quad \beta_{ijk} = \beta_{ijk}^0 \left(\frac{r_{ij}^0}{r_{ij}} \right)^{7/2} \left(\frac{r_{ik}^0}{r_{ik}} \right)^{7/2} \left(\frac{\theta_0}{\theta} \right)^{\nu} \quad (7.5)$$

The scaling exponents for the bond length dependence of the force constant α and β have been found to be universal for all alloys of the group IV elements [81]. The exponent ν describes the dependence of the bond-bending force constant β on the angle θ between two bonds as obtained from a fit to phonon-deformation potentials. For the calculations shown later in this chapter the values from [81] were applied.

The dynamical matrix and thus the eigen-frequencies and eigen-vectors of the vibrational modes can be calculated from the deformation energy W (Eq. (7.3)). The

correct selection rules have to be considered for the calculation of the Raman and absorption spectra.

To calculate the Raman spectra the same polarizability for all atoms is assumed. The off-resonance Raman intensities are then given by

$$\sigma^{xy} \propto \sum_{\mu} \frac{2\Gamma\omega}{(\omega_{\mu}^2 - \omega^2)^2 + \Gamma^2\omega^2} \left| \sum_i s_i u_{iz}^{\mu} \right|^2 \quad (7.6)$$

Here, μ runs over all phonon modes, u_{iz}^{μ} is the displacement vector of the atoms at lattice site i , and s_i is +1 and -1 for the two fcc sublattices of the diamond structure. The Cartesian indices x , y and z specify the polarization. A Lorentzian lineshape with a broadening of $\Gamma = 3 \text{ cm}^{-1}$ is assumed.

The absorption coefficient for infrared light is given by the imaginary part ϵ_2 of the dielectric function:

$$\epsilon_2^{xy} \propto \sum_{\mu} \frac{2\Gamma\omega}{(\omega_{\mu}^2 - \omega^2)^2 + \Gamma^2\omega^2} \sum_{i,j} z_i^* z_j^* u_{ix}^{\mu} u_{jy}^{\mu} \quad (7.7)$$

Here, the factor z^* represents an effective charge of the Si and Ge atoms. This charge is caused by the differing electro-negativities of the two elements. While this model accounts for the single-phonon absorption due to Si-Ge vibrations it does not describe the multi-phonon background.

To calculate the spectra, 512 atom supercells with randomly distributed atoms according to the stoichiometry were used. Calculated Raman and absorption spectra for different Si concentrations are shown in Fig. 7.7. The dominant line in the calculated absorption spectra in Fig. 7.7 (a) is the localized Si mode at 390 cm^{-1} . The two IR-active vibrational modes from Si nearest neighbor pairs are also labeled. These modes are at approximately 310 and 370 cm^{-1} . The calculated Raman spectra in Fig. 7.7 (b) contain besides the strong Ge phonon at 300 cm^{-1} also the localized Si vibration at 390 cm^{-1} and the two Raman-active vibrational modes from Si nearest neighbors at 400 and 450 cm^{-1} , as expected. With increasing Si concentration, the number of complex vibrational modes increases due to the increasing number of Si neighbors.

The agreement between the calculated and measured Raman and absorption spectra is quite good. The low temperature absorption spectrum of Fig. 7.1 (b) clearly shows the weak mode at 310 cm^{-1} . The second IR-active mode from Si nearest neighbor pairs at 370 cm^{-1} is also seen, as shown in Fig. 7.4. The purely Raman-active mode at 400 cm^{-1} in Fig. 7.4 is caused by Si nearest neighbor pairs. The second Raman-active Si nearest neighbor mode at 450 cm^{-1} is also shown in Fig. 7.1 (a) and will be discussed further in the next section.

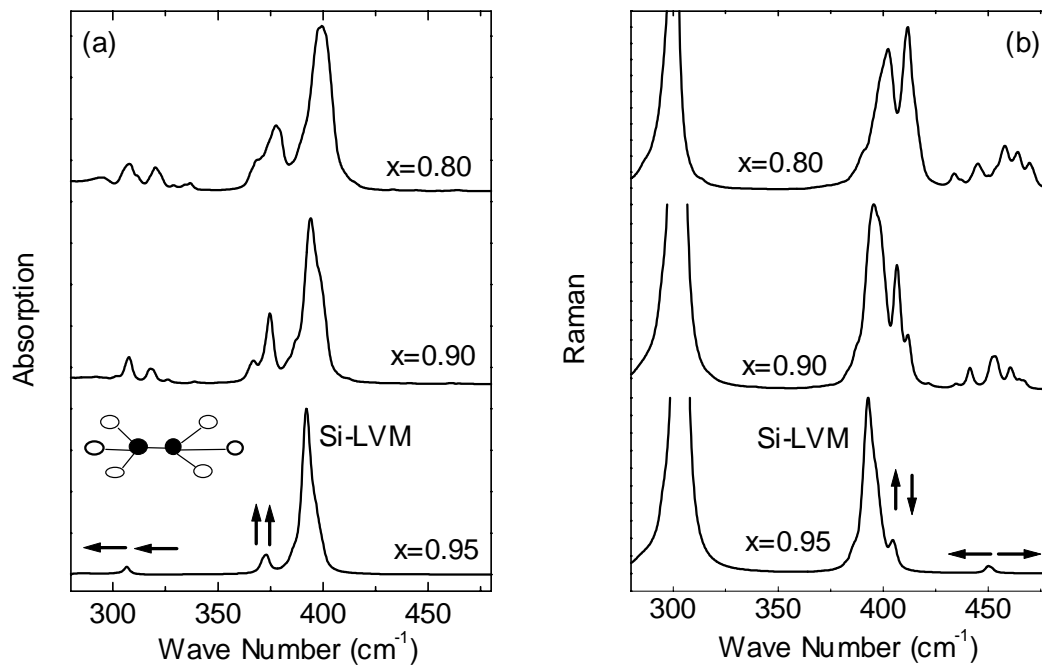


Fig. 7.7: Calculated absorption (a) and Raman (b) spectra of Ge-rich SiGe crystals with different Ge concentrations. The calculations are based on the anharmonic Keating model.¹ The arrows are labeling the vibrations of the Si nearest neighbor pairs according to Fig. 7.5.

In summary, the identification and experimental observation of the Si local vibrational mode and all four modes of Si nearest neighbor pairs in Ge-rich SiGe crystals was presented. The infrared active modes of the Si nearest neighbor have been observed for the first time. The Raman active modes had already been observed by Gaisler et al., but their interpretation was wrong. The correct assignment of the modes became possible through the comparison with calculations by the anharmonic Keating model.

7.4.3 Si-Si vibrations at 460 cm⁻¹

The observation of the vibrational mode at 460 cm⁻¹ has already been published several times with differing interpretations. Feldman et al. observed a broad line at 462 cm⁻¹ in a sample with a Si concentration of $1-x = 0.25$ [67]. This broad line consists of two unresolved lines at approximately 450 and 475 cm⁻¹. Feldman et al. assigned these two lines to the two Raman-active modes of Si nearest neighbor pair vibrations. Brya reported Raman modes at 445 and 460 cm⁻¹ for $x \geq 0.1$ [68]. He

¹ The calculations were kindly performed by Dr. Holger Rucker.

assigned the mode at 445 cm^{-1} to Si nearest neighbor pairs and the mode at 460 cm^{-1} to larger Si clusters. Gaisler et al. observed two lines at 440 and 460 cm^{-1} in a sample with $1-x = 0.2$ and assigned them both to Si nearest neighbor pairs [71].

The authors mentioned above all assumed that both Raman active modes of the Si nearest neighbor pair lie in the range of $440\text{--}460\text{ cm}^{-1}$. As was shown in the previous section, that is not the case. The energy of the TO mode of the Si nearest neighbor pair is actually much lower at 400 cm^{-1} . The clear and unambiguous assignment of the different modes became possible only through the measurement in samples with small Si concentrations of $1-x < 0.1$. For higher Si concentrations the number of vibrational modes increases rapidly due to the formation of larger Si clusters. This can be seen in

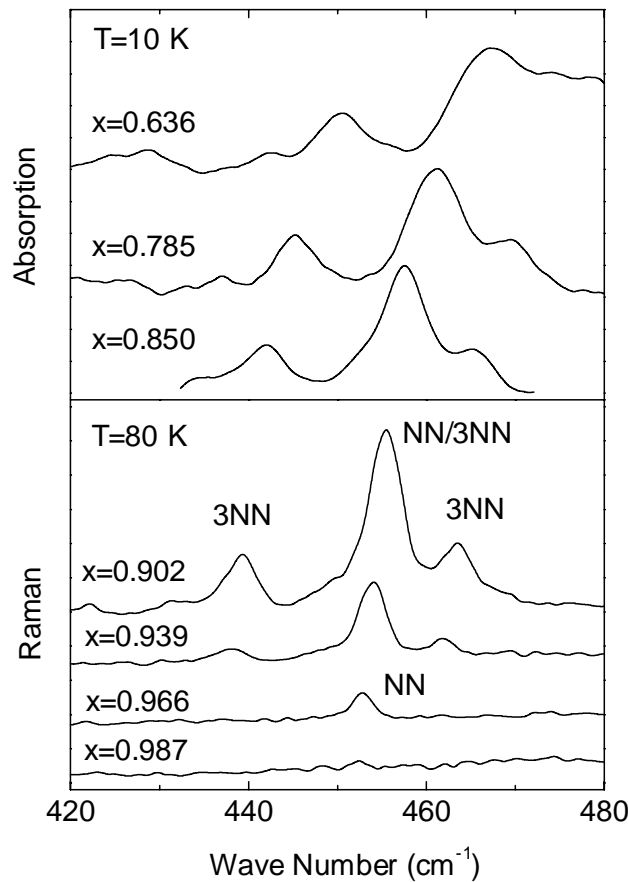


Fig. 7.8: Comparison of absorption and Raman spectra in the spectral range of the Si-Si nearest neighbor (NN) vibrations. The mode at 455 cm^{-1} appearing first in the Raman spectrum is caused by Si nearest neighbor pairs. The two modes at 440 and 465 cm^{-1} appearing for higher Si concentrations are caused by 3 directly neighbored Si atoms (3-NN). Another 3-NN mode lies at approximately 455 cm^{-1} masked by the nearest neighbor mode. These modes are only Raman active. With further increasing Si concentrations vibrational modes from additional Si atoms contribute to these modes. This can be seen in the absorption spectra beginning at $x = 0.90$.

Fig. 7.7 (b). An increasing number of modes can be seen in the range of 460 cm^{-1} with increasing Si content.

Fig. 7.8 shows the comparison of Raman and absorption spectra in this spectral range taken at 80 K and 10 K, respectively. The measurement at low temperatures, especially in the Raman spectra, made the observation of the single modes possible. Most publications dealing with these lines show measurements at room temperature and for higher silicon concentrations. In those cases the lines are not resolved and the different modes were difficult to assign. The Si-Si modes shown in Fig. 7.8 were observed in absorption for the first time.

Comparing the calculated Raman spectra in Fig. 7.7 to the measurements in Fig. 7.8 shows good agreement. The mode at 455 cm^{-1} appearing in the Raman spectrum for very small Si concentrations can be assigned to the vibrations of Si nearest neighbor pairs with help of the anharmonic Keating model (Fig. 7.7). The next two modes appearing at 440 and 465 cm^{-1} are two vibrational modes from 3 directly neighbored Si atoms. With increasing Si content even more vibrational modes from larger Si clusters contribute to these lines. Si phonons are forming in the composite crystal which absorb infrared light. This absorption starts to be observed in samples with $x = 0.90$. These modes are not present in the theoretical calculations of Fig. 7.7. Since these modes are caused by vibrations of Si-Si bonds, they are not included in the calculation due to the form of Equation (7.7).

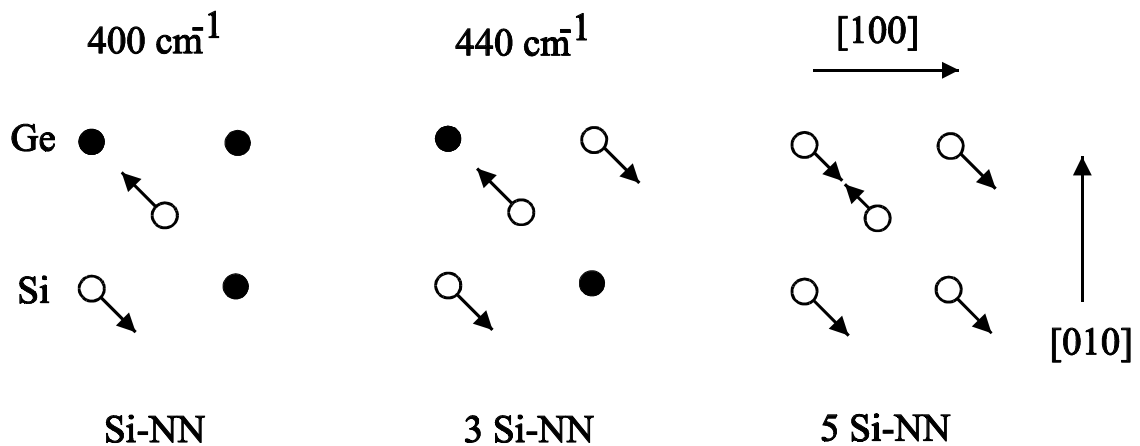


Fig. 7.9: Schematic drawing of the vibrational modes of Si nearest neighbors. This figure is according to the theoretical work of Grein and Cardona [79]. It shows the projection of the atoms into a (001) plane. The center atom has bonds with the four corner atoms. The wave numbers given at the top of the figure are the experimentally determined values from this thesis. The only-Raman active Si nearest neighbor mode (Si-NN) can be observed at 400 cm^{-1} (Fig. 7.4). For 3 Si nearest neighbor atoms this mode shifts to 440 cm^{-1} (Fig. 7.8). With increasing number of Si atoms only a small shift can be observed, so that these modes all lie in the spectral range around 460 cm^{-1} .

Other theoretical investigations of the lattice vibrations of SiGe crystals have also been published by Gironcoli [80] and Grein and Cardona [79], besides the anharmonic Keating model. Gironcoli calculated in his work Raman spectra using an "*ab initio interatomic-force-constant*" theory. In this theory force constants of higher order are included, so that the influence of local stresses are included as well. The calculated Raman spectra for $x = 0.28$, $x = 0.55$ and $x = 0.77$ agree very well with the experimentally determined Raman spectra of [69]. The theoretical Raman lines agreed to within 5 cm^{-1} with the experimental ones.

Grein and Cardona calculated the vibrational modes of Si atoms in Ge-rich samples using a "*mass-defect Green's-function*" theory [79]. They assumed that the Si atoms or clusters are embedded in a virtual SiGe crystal. This method delivers for a Si nearest neighbor pair vibrational modes at 371.9 (TA) , 384.6 (TO) and $435.0 \text{ cm}^{-1} \text{ (LO)}$. The LA mode was only said to be resonant with the background at approximately 300 cm^{-1} . For samples with small Si concentrations Grein and Cardona showed the theoretically predicted vibrational modes. The development of the TO Si nearest neighbor mode (Si-NN) with increasing number of Si atoms is shown in Fig. 7.9 [79]. The experimentally observed development of these modes is shown for the first time in this thesis.

7.5 Disorder and the Ge phonon at 300 cm^{-1}

As mentioned at the beginning of this chapter, it is possible to investigate near-range order effects in compound semiconductors with phonon spectroscopy. This has been the case for $\text{Si}_{1-y}\text{C}_y$ heteroepitaxial layers [66]. Via TEM, ordered arrangements of atoms were also discovered in AlGaAs [88] and InGaAs [89] on GaAs substrate and for Si/Ge superlattices [90]. It is assumed in these layer systems, that the strains caused by the lattice mismatch between layer and substrate are the driving force behind the near-range order.

In thick unstrained $\text{Si}_{0.5}\text{Ge}_{0.5}$ layers on silicon substrate a short-range order has also been found by TEM [91]. In this system twin-layers of Si and Ge atoms along $\langle 111 \rangle$ have been found. These layers are microscopically strained. The atomic arrangement has been explained with a small chemical energy overcompensating the microscopic strain [91]. The investigated relaxed SiGe epitaxial layers had bulk characteristics. Epitaxial layers are grown at relatively low temperatures of 390 to 475°C outside the thermodynamical equilibrium. SiGe bulk crystals on the other hand are grown at much higher temperatures. Theoretical calculations predict that the Si-Ge bond is energetically favored over the Si-Si and Ge-Ge bond [92]. The difference between the homopolar and heteropolar bond is so small, that it plays no role at the high growth temperatures of bulk crystals. So, a statistical distribution of the Si and Ge

atoms can be expected. Indeed, no near-range order has been found in SiGe bulk crystals up to this day.

Effects indicating disorder are in many regards obvious, though. Also for the case of phonon spectroscopy. The singularities in the phonon density of states of silicon and germanium are no longer as pronounced, but are said to be "smeared out". A phonon dispersion relation can not really be given in a compound crystal, as can be seen in the case of multi-phonon absorption. The influence of disorder can also be found directly in

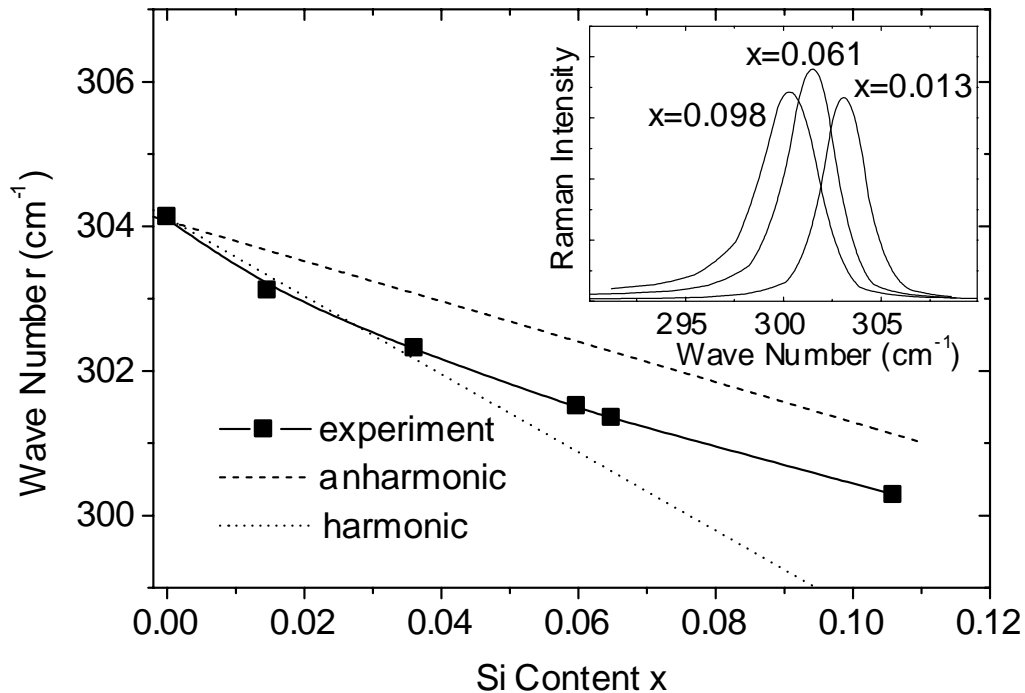


Fig. 7.10: Shift of the Ge phonon in SiGe bulk crystals with Si concentrations $0 \leq 1-x \leq 0.12$. The Ge phonon shifts continuously to smaller energies with increasing Si content. Peak positions of measured Raman spectra (symbols) are shown together with results of calculations with anharmonic Keating model (dashed line) and calculations with zero anharmonicity (dotted line). The inset shows the Raman spectra of the Ge phonon for different alloy compositions recorded at $T = 80$ K.

Raman spectroscopy looking at the behavior of the germanium phonon at 300 cm^{-1} with increasing Si content in the sample.

Two effects influence this phonon. With the addition of Si atoms the average lattice constant will become smaller. This should shift the Ge phonon to higher energies. Through the addition of Si atoms the crystal symmetry is broken and the strong selection rule of momentum conservation is no longer strictly valid. This means that phonons with $k \neq 0$ contribute to the Raman scattering. The optical phonon energy of germanium decreases for k -values away from the center of the Brillouin zone ($k = 0$).

The Ge phonon will thus shift to lower energies with increasing Si content. The two above mentioned effects, reduction of lattice constant and increase of disorder, result in opposite directions for the shift of the Ge phonons. Measurements in samples with small Si concentrations have shown, that the shift due to disorder overcompensates the shift due to the decrease in lattice constant, so that the Ge phonon shifts continuously to smaller energies with increasing Si content. This is shown in Fig. 7.10.

Fuchs et al. observed a shift of the Ge phonon which was positive for silicon concentrations up to 2% and a continuous decrease of the Ge phonon energy for Si concentrations greater than 2% [72]. This effect could not be reproduced with the samples investigated in this thesis [74]. The experimentally determined shift of the Ge phonon is compared with results of calculations using the anharmonic Keating model as described in section 7.4.2. Supercells of 512 atoms were used for the calculations. Raman spectra were obtained by averaging over ten supercells with randomly distributed atoms. To clarify the role of the anharmonicity calculations with a harmonic model and identical force constants have also been performed. The anharmonicity was turned off by setting the exponents in Eq. (7.5) to zero. Both calculations result in a continuous decrease of Ge phonon energy (Fig. 7.10). This result contradicts earlier calculations by Fuchs et al., though both calculations used a Keating model and supercells. This discrepancy can not be resolved. We even tested the sensitivity of our calculations to the numerical values of the two force constants α and β (Eq. (7.3)). A monotonously decreasing frequency of the Ge phonon with increasing Si content was found for all ratios α/β between 2 and 12. Other theories reproduce our results of a continuously decreasing Ge phonon energy as well [79, 81].

7.6 Summary

The lattice vibrations of SiGe have been investigated ever since the 1960's; mainly by Raman spectroscopy. Despite the many investigations, several open questions and contradicting results remained. In this thesis some of the open questions could be clarified and some details were contributed to the picture of phonon spectroscopy of SiGe crystals.

- Through the comparison of absorption and Raman measurements the model for the Raman active mode at 400 cm^{-1} given by Gaisler et al. [71] was shown to be wrong. In the model by Gaisler et al. this mode results from the increasing influence of Si atoms on the energy of the localized vibrational mode at 390 cm^{-1} . Here, the exclusively Raman active mode at 400 cm^{-1} was unambiguously identified as being caused by the vibration of Si nearest neighbor pairs. This identification became possible only through theoretical calculations with the anharmonic Keating model.

- The Si nearest neighbor pairs have a second vibrational mode at 455 cm^{-1} . In this spectral range, contradicting and unclear assignments of the Raman modes can be found in literature. Through Raman measurements at low temperatures, it became possible to assign the observed modes with increasing Si content to vibrations from two directly neighbored Si atoms and three directly neighbored Si atoms. In absorption the vibrations from several neighboring Si atoms have been assigned unambiguously for the first time. The experimental results confirm the theoretical predictions reported in the literature for the development of vibrational modes in Ge-rich SiGe bulk crystals.
- The Si nearest neighbor pair induces two exclusively infrared active modes which were observed for the first time and assigned by comparison with theoretical calculations.
- The excellent agreement between the experimental spectra and theoretical results of the anharmonic Keating model show the strong influence of local stresses on the lattice vibrations of SiGe bulk crystals. The assumptions made in the anharmonic Keating model could be confirmed by the experimental results in SiGe crystals.
- The localized vibrational modes of all three silicon isotopes have been observed for the first time in Ge-rich samples using Raman spectroscopy. This observation is a direct experimental verification of the assignment of the local vibrational mode of Si.
- The influence of disorder on the Ge phonon shift in Ge-rich samples with Si concentrations $0 < 1-x < 0.12$ has been shown. The observation of a continuous downshift of the Ge phonon with increasing Si content contradicts a previous publication [72], but agrees with theoretical calculations using the anharmonic Keating model.

Outlook

The measurement of mechanical stress in Si device structures by UV micro-Raman spectroscopy showed the potential of the technique to identify process steps, which induce high stress levels in the silicon substrate. The small penetration of UV light into silicon helps to observe areas of high stress in especially critical edge regions, which have so far been averaged away by longer wavelength light. This information can be used to reduce the potential for defect formation. The automation of this non-destructive technique would help to introduce UV micro-Raman spectroscopy into industry as a helpful tool for the optimization of future deep submicron technologies.

UV light significantly reduces stress averaging. This makes the comparison between simulated and measured stress much easier. The physical models used for stress simulation can be verified and quantified with greater accuracy, since the UV measurements deliver values for the true near-surface stress. The measured Si phonon shape in the Raman spectrum also deviates much stronger from a perfect Lorentzian lineshape, if the stress distribution in the laser focus is inhomogeneous. This additional information contained in the lineshape can be used in conjunction with stress simulations to obtain information about all stress components under the laser focus. The assumption of uniaxial stress for the assignment of stress values to the measured phonon shifts would thus be rendered obsolete. The extraction of the different stress components from a lineshape analysis of the measured Raman signal is a challenge for the future.

Comparing the stress measurements of UV micro-Raman spectroscopy with TEM techniques, such as CBED, should help to verify and quantify the models needed to interpret the TEM results.

This thesis also presented the investigation of phonons in SiGe bulk crystals with micro-Raman and FTIR spectroscopy. The obtained results can be compared to SiGe epitaxial layers. The physical properties of bulk crystals are influenced by disorder of the composite crystal and local strains. In addition to that, epitaxial layers are influenced by further effects such as macroscopic strains due to lattice mismatch between substrate and layer, properties of buffer layers, and confinement effects in very thin films. A comparison of the properties of bulk crystals and epitaxial layers can help to identify epitaxy-specific effects.

The interpretation of the phonon spectrum of SiGe bulk crystals gave no sign of an atomic order. Systematic thermal treatment of bulk crystals with a Si/Ge content of 50% could deliver insight into a order-disorder transition of SiGe. The results obtained

in this thesis with regard to the phonons in SiGe could be used as a basis for such investigations.

Micro-Raman spectroscopy allows one to measure phonon properties with a spatial resolution of around 1 μm . The spatial resolution can be used to monitor the homogeneity of crystal composition in bulk crystals and SiGe epitaxial layers over the size of a wafer or crystal.

Abbreviations

CBED	Convergent Beam Electron Diffraction
CCD	Charge Coupled Device
CMOS	Complementary Metal Oxide Semiconductor
CMP	Chemical Mechanical Polishing
CVD	Chemical Vapor Deposition
EDX	Energy Dispersive X-Ray analysis
FE	Finite Element
FTIR	Fourier Transform Infrared
FWHM	Full Width at Half Maximum
HBT	Hetero Bipolar Transistor
HDP	High Density Plasma
HSQ	Hydrogen Silesquioxane
IC	Integrated Circuit
IR	Infrared
LA	Longitudinal Acoustic phonon
LO	Longitudinal Optical phonon
LOCOS	Local Oxidation of Silicon
LPCVD	Low Pressure Chemical Vapor Deposition
LVM	Local Vibrational Mode
N.A.	Numerical Aperture
NN	Nearest Neighbor
PBLOCOS	Poly-Buffered Local Oxidation of Silicon
PDP	Phonon Deformation Potential
PG	Pre-Gate
PL	Photoluminescence
RIE	Reactive Ion Etching
RSNOM	Raman Spectroscopy with Near-field Optical Microscopy
SEM	Scanning Electron Microscopy
SIL	Solid Immersion Lens

STI	Shallow Trench Isolation
SW	Sidewall
TA	Transverse Acoustic phonon
TEM	Transmission Electron Microscopy
TEOS	Tetra-Ethyl-Ortho-Silicate
TO	Transverse Optical phonon
UV	Ultraviolet
XTEM	Cross-sectional Transmission Electron Microscopy

References

- [1] G.E. Moore, "Progress in Digital Integrated Electronics", *Proc. IEEE Int. Electron Devices Meeting* (1975), p. 11
- [2] C.V. Raman, *Ind. J. Phys.* **2**, 387 (1928)
- [3] G. Landsberg and L. Mandelstam, *Naturwiss.* **16**, 57 (1928)
- [4] J.P. Russell, *Appl. Phys. Lett.* **6**, 223 (1965)
- [5] J.H. Parker, Jr., D.W. Feldman and M. Ashkin, *Phys. Rev.* **155**, 712 (1967)
- [6] M. Cardona (ed.): *Light Scattering in Solids*, 2nd edn., *Topics Appl. Phys.*, Vol.8 (Springer, Berlin, Heidelberg 1983)
- [7] M. Cardona and G. Güntherodt (eds.): *Light Scattering in Solids II-V*, *Topics Appl. Phys.*, Vols.50,51,54,66 (Springer, Berlin, Heidelberg, 1982, 1984, 1989)
- [8] K. Brunner, G. Abstreiter, B.O. Kolbesen and H.W. Meul, *Appl. Surf. Science* **39**, 116 (1989)
- [9] I. De Wolf, *Semicond. Sci. Technol.* **11**, 139 (1996)
- [10] S.C. Jain, H.E. Maes, K. Pinardi and I. De Wolf, *J. Appl. Phys.* **79**, 8145 (1996)
- [11] R. Loudon, *Adv. Phys.* **13**, 423 (1964); erratum *ibid.* **14**, 621 (1965)
- [12] S. Webster, D.N. Batchelder and D.A. Smith, *Appl. Phys. Lett.* **72**, 1478 (1998)
- [13] I. De Wolf, G. Groeseneken, H.E. Maes, M. Bolt, K. Barla, A. Reader, P.J. McNally, *Proceedings of 1998 ISTFA* (Dallas, 1998), p. 11215
- [14] C.D. Poweleit, A. Gunther, S. Goodnick and J. Menéndez, *Appl. Phys. Lett.* **73**, 2275 (1998)
- [15] B. Dietrich and K.F. Dombrowski, *J. Raman Spectrosc.* **30**, 893 (1999)
- [16] D.E. Aspnes and A.A. Studna, *Phys. Rev. B* **27**, 985 (1983)
- [17] M. Born and E. Wolf, *Principles of Optics*, 6th edn., (Pergamon Press, Oxford, 1985), p. 441
- [18] D.M. Lipkin and D.R. Clark, *J. Appl. Phys.* **77**, 1855 (1995)
- [19] S. Ganesan, A.A. Maradudin and J. Oitmaa, *Ann. Phys.* **56**, 556 (1970)
- [20] E. Anastassakis, A. Pinczuk, E. Burstein, F.H. Pollak and M. Cardona, *Solid State Commun.* **8**, 133 (1970)
- [21] J.F. Nye, *Physical Properties of Crystals*, (Clarendon Press, Oxford, 1964)
- [22] E. Anastassakis, *J. Appl. Phys.* **82**, 1582 (1997)
- [23] I. De Wolf, H.E. Maes and S.K. Jones, *J. Appl. Phys.* **79**, 7148 (1996), *addendum*: I. De Wolf and E. Anastassakis, *J. Appl. Phys.* **85**, 7484 (1999)
- [24] M. Chandrasekhar, J.B. Renucci and M. Cardona, *Phys. Rev.* **17**, 1623 (1978)
- [25] E. Anastassakis, A. Cantarero and M. Cardona, *Phys. Rev. B* **41**, 7529 (1990)
- [26] O.H. Nielsen and R.M. Martin, *Phys. Rev. Lett.* **50**, 697 (1985); *Phys. Rev. B* **40**, 3792 (1985)

- [27] M. Methfessel, C.O. Rodriguez and O.K. Andersen, Phys. Rev. B **40**, 2009 (1989)
- [28] S.M. Hu, J. Appl. Phys. **50**, 4661 (1979)
- [29] J. Vanhellemont, S. Amelinckx and C. Claeys, J. Appl. Phys. **61**, 2170 (1987), and J. Appl. Phys. **61**, 2176 (1987)
- [30] A. Fischer and H. Richter, J. Appl. Phys. **75**, 657 (1994)
- [31] A. Atkinson, T. Johnson, A.H. Harker and S.C. Jain, Thin Solid Films **274**, 106 (1996)
- [32] A. Fischer, H. Kühne, G. Lippert, H. Richter and B. Tillack, phys. stat. sol. (a) **171**, 475 (1999)
- [33] I. De Wolf, G. Pozzat, K. Pinardi, D.J. Howard, M. Ignat, S.C. Jain and H.E. Maes, Microelectron. Reliab. **36**, 1751 (1996)
- [34] I. De Wolf, M. Ignat, G. Pozza, L. Maniguet and H.E. Maes, J. Appl. Phys. **85**, 6477 (1999)
- [35] M. Qing, S. Chiras, D.R. Clark and Z. Suo, J. Appl. Phys. **78**, 1614 (1995)
- [36] S.K. Jones, A. Poncet, I. De Wolf, M.M. Ahmed and W.J. Rothwell, *Proceedings of the 1994 International Electron Devices Meeting (IEDM, San Francisco, 1994)*, p. 877
- [37] K.F. Dombrowski, I. De Wolf and B. Dietrich, Appl. Phys. Lett. **75**, 2450 (1999)
- [38] K.F. Dombrowski and I. De Wolf, Solid State Phenomena Vols. **63-64**, 519 (1998)
- [39] A.H. Perera, J.-H. Lin, Y.-C. Yu, M. Azrak, B. Taylor, J. Hayden, M. Thomas and M. Blackwell, *Proceedings of the 1995 International Electron Devices Meeting (IEDM, Washington, DC, 1995)*, p. 679
- [40] K.F. Dombrowski, B. Dietrich, I. De Wolf, R. Rooyackers and G. Badenes, *Proceedings of the 1999 European Solid State Devices Research Conference (ESSDERC, Leuven, 1999)*, p.196
- [41] K.F. Dombrowski, A. Fischer, B. Dietrich, I. De Wolf, H. Bender, S. Pochet, V. Simons, R. Rooyackers, G. Badenes, C. Stuer and J. Van Landuyt, *Proceedings of the 1999 International Electron Devices Meeting (IEDM, Washington, DC, 1999)*, p. 357
- [42] S.M. Hu, J. Appl. Phys. **70**, R53 (1991)
- [43] V.Senez, D.Collard, B.Baccus, M.Brault and J.Lebailly, J. Appl. Phys. **76**, 3285 (1994)
- [44] V. Senez et al., *Proceedings of the 1996 International Electron Devices Meeting (IEDM, San Francisco, 1996)*, p. 705
- [45] B. Baccus, Solid State Electron. **32**, 1013 (1989)
- [46] T. Hoffmann, K.F. Dombrowski and V. Senez, *Proceedings of the Conference on Modeling and Simulation of Microsystems (MSM, San Diego, 2000)*, in press
- [47] H. Stöhr and W. Klemm, Zeitschrift für anorg. u. allg. Chemie **241**, 305 (1939)
- [48] A. Erko, F. Schäfer, W. Gudat, N.V. Abrosimov, S.N. Rossolenko, V. Alex, S. Groth and W. Schröder, Nuc. Inst. Methods in Phys. Research A **374**, 408 (1996)
- [49] R.K. Smither, Rev. Sci. Instrum. **53**, 131 (1982)

- [50] R. Madar, E. Mastromatteo, A. Magerl, K.-D. Liss and C. Bernard, *Surface and Coatings Technology* **54/55**, 229 (1992)
- [51] J.M. Ruiz, J. Casado and A. Luque, *Proceedings of the 12th EC Photovoltaic Solar Energy Conference* (Amsterdam, 1994), p. 572
- [52] N. Sugii, K. Nakagawa, Y. Kimura, S. Yamaguchi and M. Miyao, *Semicond. Sci. Technol.* **13**, A140 (1998)
- [53] J.P. Dismukes, L. Ekstrom and J.R. Pfaff, *J. Phys. Chem.* **68**, 3021 (1964)
- [54] Landoldt-Börnstein, *Numerical Data and Functional Relationships in Science and Technology*, Vol. 17 Semiconductors, Subvol. a, Physics of Group IV Elements and III-V Compounds (Springer, Berlin, 1989)
- [55] F. Cerdeira, C.J. Buchenauer, F.H. Pollak and M. Cardona, *Phys. Rev. B* **5**, 580 (1972)
- [56] J. Weber and M.I. Alonso, *Phys. Rev. B* **40**, 5683 (1989)
- [57] B. Roos, H. Richter and J. Wollweber, *Solid State Phenomena* **47-48**, 509 (1996)
- [58] J.A. Floro, E. Chason, S.R. Lee and G.A. Petersen, *Appl. Phys. Lett.* **71**, 1694 (1997)
- [59] P. Dold, A. Barz, S. Recha, K. Pressel, M. Franz and K.W. Benz, *J. Cryst. Growth* **192**, 125 (1998)
- [60] A. Barz, P. Dold, U. Kerat, S. Recha, K.W. Benz, M. Franz and K. Pressel, *J. Vac. Sci. Technol. B* **16**, 1627 (1998)
- [61] A. Barz, U. Kerat, P. Dold and K.W. Benz, *Cryst. Res. Technol.* **33**, 849 (1998)
- [62] N.V. Abrosimov, S.N. Rossolenko, W. Thieme, A. Gerhardt and W. Schröder, *J. Cryst. Growth* **174**, 182 (1997)
- [63] W.L. Bond, *Acta Cryst.* **13**, 814 (1960)
- [64] J. Donecker, A. Gerhardt and J. Wollweber, *Mat. Sci. Eng. B* **28**, 18 (1994)
- [65] J.C. Tsang, P.M. Mooney, F. Dacol and J.O. Chu, *J. Appl. Phys.* **75**, 8098 (1994)
- [66] H. Rucker, M. Methfessel, B. Dietrich, K. Pressel and H.J. Osten, *Phys. Rev. B* **53**, 1302 (1996)
- [67] D.W. Feldman, M. Ashkin and J.H. Parker, Jr., *Phys. Rev. Lett.* **17**, 1209 (1966)
- [68] W.J. Brya, *Solid State Commun.* **12**, 253 (1972)
- [69] M.I. Alonso and K. Winer, *Phys. Rev. B* **39**, 10056 (1989)
- [70] D.J. Lockwood, K. Rajan, E.W. Fenton, J.-M. Baribeau and M.W. Denhoff, *Solid State Commun.* **61**, 465 (1987)
- [71] V.A. Gaisler, O.A. Kuznetsov, I.G. Neizvestnyi, L.K. Orlov, M.P. Sinyukov and A.B. Talochkin, *Sov. Phys. Solid State* **31**, 2006 (1990)
- [72] H.D. Fuchs, C.H. Grein, M.I. Alonso and M. Cardona, *Phys. Rev. B* **44**, 13120 (1991)
- [73] M. Franz, K. Pressel, K.F. Dombrowski, H. Rucker, A. Barz, P. Dold and K.W. Benz, *Mat. Sci. Forum Vols.* **258-263**, 109 (1997)
- [74] M. Franz, K.F. Dombrowski, H. Rucker, B. Dietrich, K. Pressel, A. Barz, U. Kerat, P. Dold and K.W. Benz, *Phys. Rev. B* **59**, 10614 (1999)
- [75] R. Braunstein, *Phys. Rev.* **130**, 879 (1962)

- [76] A.E. Cosand and W.G. Spitzer, J. Appl. Phys. **42**, 5241 (1971)
- [77] S.C. Shen and M. Cardona, Solid State Commun. **36**, 327 (1980)
- [78] J. Humlicek, K. Navratil, M.G. Kekoua, E.V. Khoutsishvili, Solid State Commun. **76**, 243 (1990)
- [79] C.H. Grein and M. Cardona, Phys. Rev. B **45**, 8328 (1992)
- [80] S. de Gironcoli, Phys. Rev. B **46**, 2412 (1992)
- [81] H. Rücker and M. Methfessel, Phys. Rev. B **52**, 11059 (1995)
- [82] M. Lax and E. Burnstein, Phys. Rev. **97**, 39 (1955)
- [83] K. Winer and M. Cardona, Phys. Rev. B **35**, 8189 (1987)
- [84] A.S. Barker, Jr. and A.J. Sievers, Rev. Mod. Phys. **47**, Suppl. No.2, S2 (1975)
- [85] P.G. Dawber and R.J. Elliot, Proc. Phys. Soc. **81**, 453 (1962)
- [86] R.C. Newman, *Infrared Studies of Crystal Defects*, Taylor & Francis (London, 1973)
- [87] P.N. Keating, Phys. Rev. **145**, 637 (1966)
- [88] T.S. Kuan, T.F. Kuech, W.I. Wang and E.L. Wilkie, Phys. Rev. Lett. **54**, 201 (1985)
- [89] T. Fukui and H. Saito, Jpn. J. Appl. Phys. **23**, 521 (1984)
- [90] A. Ourmazd and J.C. Bean, Phys. Rev. Lett. **55**, 765 (1985)
- [91] F.K. LeGoues, V.P. Kesan and S.S. Iyer, Phys. Rev. Lett. **64**, 40 (1989)
- [92] J.L. Martins and A. Zunger, Phys. Rev. Lett. **56**, 1400 (1986)

Acknowledgements

At this point I would like to express my earnest gratitude to the many people, who have accompanied and helped me in the completion of this work throughout the past years:

First of all, I want to thank my thesis advisor, Prof. B. Dietrich, for his guidance, encouragement and support during all the years of my thesis work. For the opportunity to perform these studies at the institute and all his contributions to my work, I am very grateful.

Next, I want to thank Prof. A. Ourmazd, Prof. J. Wagner, and Prof. J. Reif for their contribution in the evaluation of my thesis.

Special thanks go to Dr. I. De Wolf, who gave me invaluable insights into the secrets of stress measurements with micro-Raman spectroscopy. The many discussions and her knowledge have contributed greatly to the success of my work. I am also very grateful to Dr. R. Rooyackers and Dr. G. Badenes, who provided me with a constant flow of the highly interesting sample material, from which I obtained my experimental results.

I also want to thank the Crystallographic Institute at Freiburg University for the excellent SiGe bulk crystals.

Dr. M. Franz and Dr. H. Rücker have contributed to this thesis with infrared absorption measurements and theoretical calculations using the anharmonic Keating model, for which I am very grateful.

Dr. K. Pressel has earned my gratitude for all the cheering up and for just being there to listen.

I want to thank Dr. A. Fischer for his contributions to my understanding of the theoretical background of mechanical stress.

Part of this work was supported financially by the Deutsche Forschungsgemeinschaft (DFG) in the frame of the project "Defects in SiGe" (PR 493/3-3).

Last, but certainly not least, I am very grateful for the moral support, understanding, and love of my parents, family, and my beloved wife.